Study on Thermoelectric and Mechanical Properties of *n* and *p*-type Skutterudites, and Contact Alloy for Si-Ge

A Dissertation

Presented to

the Faculty of the Department of Physics and T_CSUH

University of Houston

In Partial Fulfillment

of the Requirements for the Degree

Doctor of Philosophy

By

Tulashi Dahal

December 2014

Study on Thermoelectric and Mechanical Properties of *n* and *p*-type Skutterudites, and Contact Alloy for Si-Ge

---

Tulashi Dahal

Prof. Zhifeng Ren

Department of Physics and T_CSUH

Prof. Wei Kan Chu

Department of Physics and T_CSUH

Prof. Oomman Varghese

Department of Physics

Prof. Shuo Chen

Department of Physics

Prof. Jiming Bao

Department of Electrical and Computer Engineering

Dean, College of Natural Sciences and Mathematics

Acknowledgments

I feel truly blessed to find Prof. Zhifeng Ren as my advisor for pursuing my doctoral degree. I am extremely indebted to him for his systematic and wise mentoring, detailed instructions, high-standard education, and fatherly generosity. Prof. Ren was always available for discussion and guidance. His guidance and character helped me not only make more substantial accomplishments as a professional, but also made me a good person in my daily life. I would like to express my sincere gratitude to the committee members of this dissertation who offered tremendous guidance and contributions to my efforts involved in this dissertation and to my general activities during the pursuit of my degree. It is truly a privilege to be working with and under the instruction of such a group of prestigious scholars, Prof. Zhifeng Ren, Prof. Wei-Kan Chu, Prof. Oomman Varghese, Prof. Jiming Bao, and Prof. Shuo Chen. My sincere thanks to Dr. Qing Jie for his fruitful discussion and guidance. I am thankful to my colleagues at UH, Dr. Yucheng Lan, Dr. Chuanfei Guo, Dr. Weishu Liu, Dr. Dezhi Wang, Mr. Hui Wang, Dr. Hee Seok Kim, Ms. Sonika Gahalwat, Mr. Lu Tang, Mr. Keshab Dahal, and Mr. Machhindra Koirala. I am equally thankful to Dr. Kenneth McEnaney at MIT for his help. I am equally indebted to my friend Dr. Giri Joshi and my senior Dr. Bed Poudel for their fruitful discussion. Finally, I would like to offer special thanks to my wife Indira (Muna) and daughters, Mridula and Manashi for their unconditional and unlimited support to my career and for the joy of my life. I would like to offer my sincere gratitude to my brother Nawaraj and his family for their inspiration all the time. It is certainly beyond thanks how much I owe to my beloved parents for their unconditional love and inspiration.

Study on Thermoelectric and Mechanical Properties of *n* and *p*-type Skutterudites, and Contact Alloy for Si-Ge

---

An Abstract of a Dissertation

Presented to

the Faculty of the Department of Physics and T_CSUH

University of Houston

In Partial Fulfillment

of the Requirements for the Degree

Doctor of Philosophy

By

Tulashi Dahal

December 2014

Abstract

Thermoelectric devices that consist of both *n* and *p*-type thermoelectric materials connected electrically in series and thermally in parallel is regarded as one of the alternative technologies to improve the system efficiency. Some of the unique features such as silence in operation, extreme reliability, no moving parts, low cost, and environmentally friendliness make thermoelectric devices attractive. The performance of these materials depends on the dimensionless figure-of-merit, ZT $(= \frac{S^2\sigma}{\kappa}T)$, where S, σ, κ, and T are the Seebeck coefficient, electrical conductivity, thermal conductivity, and absolute temperature, respectively. Most of the commercialized thermoelectric materials have ZT value ~1. To realize commercially competitive devices, a higher ZT value is required. Skutterudites compounds allow tuning both electrical and thermal conductivity simultaneously to improve their ZTs. A peak ZT ~1.4 at 550 ^{o}C obtained in $Yb_{0.35}Co_4Sb_{12}$ is higher than the previously reported value of ~1.2 for the same nominal composition. The enhancement in ZT is mainly due to the increased electrical conductivity, which may be due to the fewer defects in the sample made by pre-alloying the elements. By bringing a perturbation in Sb-planner ring replacing small amount of Sb by Sn and Te, a peak ZT above 1.1 at 500 ^{o}C is achieved in *n*-type $CoSb_{2.8}Sn_{0.005}Te_{0.195}$. The thermoelectric devices based on skutterudites requires higher ZT in *p*-type material to maximize the device efficiency. Experiments were carried out to improve the performance of *p*-type skutterudites. By tuning the (Fe/Ni) ratio and fillers concentration, a peak ZT ~1.1 at 475 ^{o}C in $Ce_{0.4}Nd_{0.4}Fe_{3.7}Ni_{0.3}Sb_{12}$ is achieved. A peak ZT ~1.1 at 425 ^{o}C in rare earth-based

misch metal-filled $Mm_{0.9}Fe_{3.1}Co_{0.9}Sb_{12}$ ($Mm=La_{0.25}Ce_{0.5}Pr_{0.05}Nd_{0.15}Fe_{0.03}$), and a peak *ZT* in excess of 1.1 at 500 ^{o}C in $La_{0.68}Ce_{0.22}Fe_{3.5}Co_{0.5}Sb_{12}$ are achieved. An output power density of ~8 W cm^{-2} for ΔT = 475 ^{o}C is estimated in a 2×2×12 mm^3 sample of $La_{0.68}Ce_{0.22}Fe_{3.5}Co_{0.5}Sb_{12}$. The mechanical property studies reveal that the hardness and Young's modulus of elasticity of skutterudites are better than that of Bi_2Te_3- and PbTe-based thermoelectric materials. Mismatch in thermal expansion coefficient and a weaker bonding between the contact alloy and Si-Ge material led to broken samples. Further experiment is required to resolve this issue.

Contents

List of Figures

Chapter 1

Chapter 2

Chapter 3

Chapter 4

Chapter 5

Chapter 6

Chapter 7

List of Tables

Abbreviation	Meaning
DC hot press	Direct current induced hot press
Fig.	Figure
XRD	X-ray diffraction
EDS	Energy dispersive spectroscopy
TEM	Transmission electron microscopy
SEM	Scanning electron microscopy
IR	Infra-red
PF	Power factor
RTG	Radio isotopic thermoelectric generator
TC	Thermocouple
TE	Thermoelectric
RT	Room temperature
ADP	Atomic displacement parameters
MP	Mechanical property
CTE	Coefficient of thermal expansion
IIT	Instrumented indentation technique
CSM	Continuous stiffness measurements

Symbol	Meaning
Z	Figure-of-merit
ZT	Dimensionless figure-of-merit
T	Temperature
S	Seebeck coefficient
π	Peltier coefficient
b	Thomson coefficient
E_f	Fermi energy
σ	Electrical conductivity
κ	Thermal conductivity
τ	Scattering time
e	Electronic charge
μ	Carrier mobility
m^*	Effective mass
κ_B	Boltzmann constant
n	Carrier concentration
ω	Frequency
ω_D	Debye frequency
l	Mean free path
κ_l	Lattice thermal conductivity

κ_e	Carrier thermal conductivity
η	Device efficiency
ϕ	Coefficient of performance
θ_D	Debye temperature
R_H	Hall coefficient
q	Heat flux
λ	Wavelength
ρ	Resistivity
$t_{1/2}$	Half time
α	Thermal diffusivity
C_p	Specific heat capacity at constant pressure
ε	Dielectric constant
J	Current density
H	Hardness
E	Young's modulus of elasticity
E_r	Reduced modulus of elasticity
υ	Poisson's ratio of test material
υ_i	Poisson's ratio of indenter
E_i	Modulus of elasticity of indenter
P	Load

Chapter 1

Introduction and Theory of Thermoelectrics

1.1 Introduction

Thermoelectricity is the direct conversion of heat into electrical energy or vice versa. This phenomenon is based on three reversible effects named for Seebeck, Peltier, and Thomson for their respective discoveries during the 18th century. However, this area did not get much attention from researchers until 1950, when Ioffe found that the doped semi-conductors alloy have better thermoelectric (TE) performance than pure metals or semi-conductors [1]. This observation expedited the research in the field and some significant results have been reported with different semi-conductor alloys [2-6]. Although the efficiency of thermoelectric devices is relatively lower than conventional power generators or compressors, these devices promise some revolutionizing features. The TE device does not have moving parts, is silent in operation, light in weight, reliable, environmentally friendly, and cost effective. Also, these devices are easy to fabricate into portable or small devices for local cooling, and have better temperature accuracy when required.

Followed by the fact that we have limited fossil fuels, burning fossil fuels impact the environment adversely, and we have limited sources of energy, the possibility of using thermoelectric devices as an alternate source of energy was given a closer re-examination to develop high performance thermoelectric materials in 1990's [7]. The ability of a thermoelectric (TE) material to convert heat into electricity is gauged by a dimensionless figure-of-merit, ZT defined as $ZT = \frac{S^2\sigma}{\kappa}T$, where σ is the electrical conductivity, S is the

Seebeck coefficient, $\kappa = \kappa_e + \kappa_l$, where κ_e and κ_l respectively represent the carrier contribution and lattice contribution to total thermal conductivity, and *T* is the absolute temperature [2]. To achieve a higher *ZT* value, a material should have high electrical conductivity, high Seebeck coefficient, and low thermal conductivity. But, the improvement on *ZT* value is limited due to the inter-relationship between various physical parameters involved in *ZT* calculation. However, in 1990 two important and independent concepts to develop the performance of TE devices were introduced; one using the low-dimensional material approach [8, 9] and the other by discovering the new classes of advanced bulk materials [10, 11]. The low-dimensional concept in thermoelectrics study has two strategies. The first approach is to enhance the number of available states per unit energy range near Fermi level, called the density of states. The enhancement in density of states can be achieved by reducing the dimension from bulk 3D materials to 0D quantum dots, where the density of states near Fermi level is like a delta function [7]. This approach helps tuning the Seebeck coefficient (*S*) and electrical conductivity (σ) somehow independently [8, 9]. The second strategy is to use numerous interfaces to scatter phonons more effectively than electrons as they differ in their mean free paths significantly [12]. The discovery of new bulk materials dealt with so called "phonon glass electron crystals (PGEC)", first introduced by Slack [4]. The PGEC materials are believed to have the electrical properties similar to a crystalline solid while the thermal properties are akin to that of glass. The key idea of PGEC approach is to discover materials that have very low thermal conductivity [4]. Skutterudites, complex chalcogenides, and half-Heusler intermetallic compounds are some of the material groups that represent PGEC material.

The proof of these concepts has been experimentally verified by bulk materials [10, 11, 13] and low-dimensional materials, especially on Bi_2Te_3/Sb_2Te_3 superlattices and PbTe/PbSeTe quantum dot superlattices [14, 15]. The success on improving the performance of the materials has attracted an increased attention for solid-state power generation and cooling applications. To fulfill the increasing demand, cost effective, environmental friendly, and scalable techniques to produce higher efficiency thermoelectric materials will be needed. In this dissertation, a brief review of thermoelectric phenomenon, current challenges, and our approach to develop cost effective and scalable technique to develop environmentally friendly thermoelectric materials with better performance will be discussed.

1.2. Theory of Thermoelectricity

1.2.1. Introduction

Thermoelectric effects are related to the creation of an electric field in a material due to a temperature gradient, called Seebeck effect, as well as the creation of temperature gradient in a material by passing electric current through it, known as Peltier effect. Those phenomenon were discovered in the early 19^{th} century. However, the realization to use those effects for power generation and refrigeration took almost 50 years. In this section I will discuss the physical principles to explain the thermoelectric effects and their use for the development of high performance thermoelectric materials.

(i) Seebeck Effect

The Seebeck effect is associated with the generation of potential difference across the two ends of a conductor when a temperature gradient is applied. As shown in Fig.1.2.1, two different metals, A and B, are connected to their ends at X and Y, where the end X is at high temperature and end Y is at low temperature. As a result, the carriers (electrons or holes) at the hot end gain thermal energy and start to diffuse from one end to the other, creating an internal electric field to further oppose the diffusion, creating a potential difference across the two ends called Seebeck voltage. The Seebeck voltage developed per unit change in temperature is known as Seebeck coefficient, S. Mathematically,

$$S = -\frac{\Delta V}{\Delta T} \qquad (1.2.1)$$

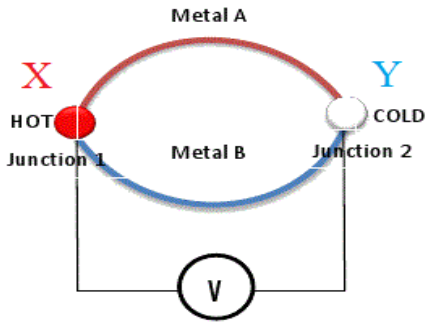

Fig. 1.2.1 Seebeck effect; a temperature difference across the two ends generates a potential difference.

(ii) Peltier Effect

The Peltier effect, first discovered by Peltier in 1834, is just a reverse process of the Seebeck effect. In this effect, if an electric current is passed through a junction of two dissimilar materials, either heat is produced or absorbed depending upon the direction of flow of current. A simple sketch of the Peltier effect is shown in Fig. 1.2.2.

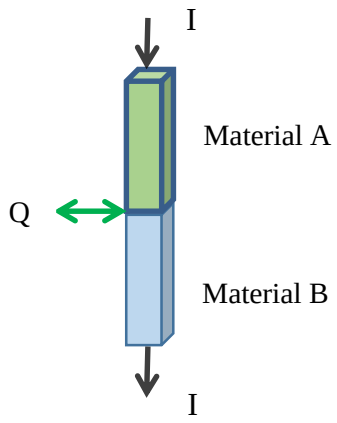

Fig. 1.2.2 Peltier effect in two dissimilar materials A and B. By passing an electric current, heat is either liberated or absorbed at the interface of the two dissimilar materials.

The rate of heat exchange at the junction of two materials due to the passage of current I is given as,

$$Q = \pi_{AB} I, \pi_{AB} = \pi_A - \pi_B \qquad (1.2.2)$$

where π_{AB} is called the Peltier coefficient of the entire thermocouple, and π_A and π_B are the Peltier coefficient of material A and material B, respectively. These Peltier coefficients represent the amount of heat current carried per unit charge in the given materials. Even though the charge current is continuous across the junction, the associated heat flow will develop a discontinuity if the Peltier coefficients π_A and π_B of the materials are different. The heat current is accompanied by electric current. Different materials have different drift velocities for the same electric current. The heat transfer mechanism at the junction is sketched in Fig. 1.2.3

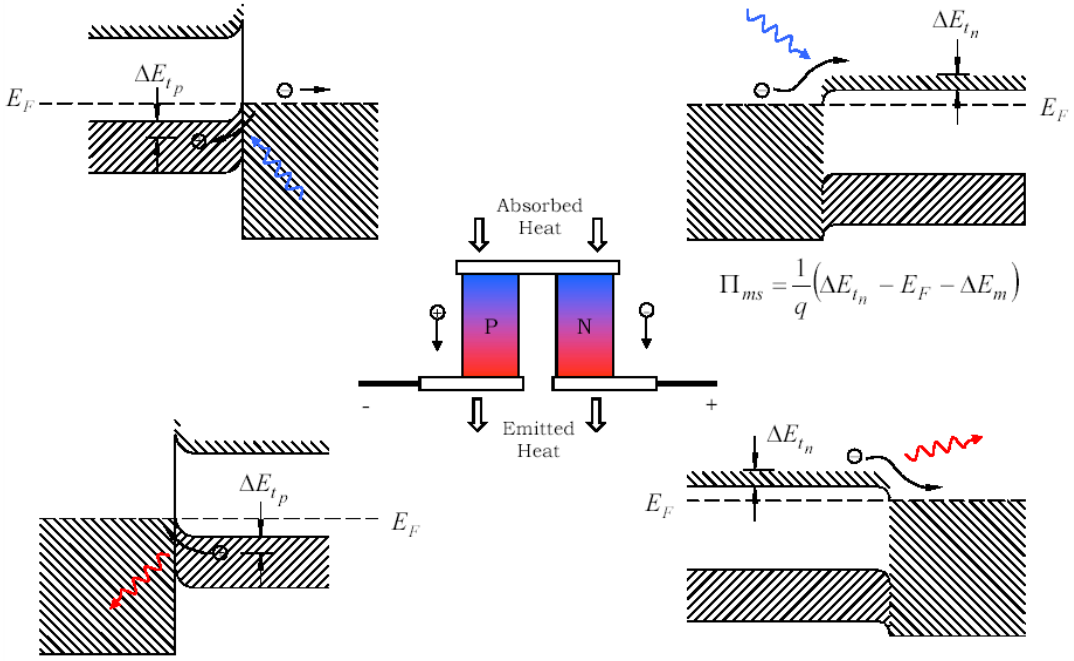

Fig. 1.2.3. A simple sketch showing heat transfer across the junctions (Presentation at DTEC by T. Hogan, Michigan State University).

Fig. 1.2.3 clearly shows that heat is absorbed at one junction and emitted from another junction, implying that the Peltier effect can be used to transfer heat from one junction to the other. Thermoelectric cooling is based on this principle. However, making efficient Peltier cooling devices using typical conductors is challenging due to a dominant Joule heating.

(iii) Thomson Effect

The Thomson effect describes the heating or cooling of an individual current-carrying conductor with a temperature gradient. Every current-carrying conductor either absorbs or emits heat, if subjected to a temperature gradient. The gradient of heat flux is given by,

$$\frac{dQ}{dx} = \tau_{AB} I \frac{dT}{dx} \qquad (1.2.3)$$

where x is a spatial co-ordinate, and τ is the Thomson coefficient.

(iv) Kelvin Relation

The Seebeck, Peltier, and Thomson effects described above are related to each other. Kelvin found the relationships between these thermoelectric effects, which are known as the Kelvins' relations, are given by

$$\pi = ST \qquad (1.2.4)$$

$$and\ b = T\frac{ds}{dT} \qquad (1.2.5)$$

where $b = \frac{dQ/dx}{IdT/dx}$ and T is the absolute temperature of the material.

1.2.2. Transport Properties

1.2.2.1 Electrical Conductivity

The general expression for electrical conductivity can be calculated using Boltzmann's transport equation given as,

$$\vec{\sigma} = \frac{e^2}{4\pi^3} \int \tau \vec{\upsilon}(\vec{\kappa}) \vec{\upsilon}(\vec{\kappa}) \frac{\partial f_0}{\partial E} d^3\kappa \qquad (1.2.6)$$

where $\vec{\sigma}$ is a symmetric second rank conductivity tensor, τ is the relaxation time, $\vec{\upsilon}(\vec{\kappa})$ is velocity of carriers, and f_0 is the Fermi distribution function. The integral evaluation [Eq. 1.2.6] over all *k*-space depends on the relation of $E(\vec{\kappa})$ with υ^2 terms. The temperature dependence on the electrical conductivity comes from the energy-dependent Fermi distribution function, $\frac{\partial f_0}{\partial E}$.

Assuming an isotropic, parabolic energy band, the electrical conductivity of a semi-conductor can be calculated using Fermi distribution function. With these approximations, electrical conductivity can be expressed as,

$$\sigma = \frac{2e^2}{m^*} \left(\frac{m^* \kappa_B T}{2\pi\hbar^2} \right)^{3/2} exp\left(-|E_F| / \kappa_B T \right) \qquad (1.2.7)$$

where E_f is the Fermi energy of the semi-conductor, κ_B is the Boltzmann constant, and m^* is the effective mass of the carriers.

1.2.2.2. Seebeck Coefficient

Using Boltzmann's equation, a general expression for the Seebeck coefficient can be written as,

$$S = \frac{1}{eT}\frac{\iiint \tau(\kappa)\upsilon_x(\kappa)\,(E(\kappa)-E_F)\left(-\frac{\partial f_0}{\partial E}\right)d^3\kappa}{\iiint \tau(\kappa)\upsilon_x(\kappa)\upsilon_x(\kappa)\left(-\frac{\partial f_0}{\partial E}\right)d^3\kappa} \qquad (1.2.8)$$

This equation can be further simplified as,

$$S = \frac{1}{eT}\frac{\int \sigma(E)(E-E_F)dE}{\int \sigma(E)}\ \alpha\,\langle E-E_F\rangle \qquad (1.2.9)$$

We have clearly seen from Eq. 1.2.9 that the Seebeck coefficient is proportional to the expectation value of energy difference of carriers and the Fermi energy. This relationship could prove useful to engineer a material such that low energy carriers are cut off and a higher Seebeck coefficient can be achieved, called the energy filtering effect. Several experimental results in the literature have reported increased Seebeck coefficient due to the energy filtering effect [16].

1.2.2.3 Mott Relation

For metals and degenerate semi-conductors, the expression 1.2.8 of Seebeck coefficient can be simplified to develop a relationship between the Seebeck coefficient (*S*) and electrical conductivity (σ). The microscopic relation that describes the relationship between *S* and σ was described by Mott and Cutler and is defined as [17],

$$S = \frac{\pi^2 {\kappa_B}^2}{3e}\left[\frac{dln\sigma(E)}{dE}\right]_{E=E_F} \qquad (1.2.10)$$

$$\text{with } \sigma(E) = n(E)e\mu(E) \qquad (1.2.11)$$

The Seebeck coefficient can be further simplified as,

$$S = \frac{\pi^2 {\kappa_B}^2}{3e}\left[\frac{1}{n}\frac{dn(E)}{dE} + \frac{1}{\mu}\frac{d\mu(E)}{dE}\right]_{E=E_F} \qquad (1.2.12)$$

where n is the carrier concentration and μ is the mobility of the charge carrier. Eq. 1.2.12 shows that for a given carrier concentration n, there are two different mechanisms to enhance the Seebeck coefficient S: a) by increasing the energy-dependent available states $dn(E)/dE$ near Fermi level or b) by increasing the energy-dependent mobility of the charge carriers. The enhancement on dn/dE can be achieved by increasing the dependence of density of states on energy, dg/dE, where g is the density of states. The enhancement on density of states can be achieved by decreasing dimensionality from 3D crystalline solids to 2D (quantum wells) to 1D (quantum wires) and finally to 0D (quantum dots) [7]. The energy-dependent mobility, $d\mu/dE$ can be increased by increasing the energy-dependent scattering time, $d\tau/dE$. For conventional semi-conductors with parabolic bands, the relaxation time can be ascribed by a power law as $\tau = \tau_0 E^{\lambda - 1/2}$, where λ is the scattering exponent, and is approximated for various scattering mechanism. For scattering of electrons on acoustic phonon, λ=0. The value of $\lambda = 1/2$ for the electrons scattered by neutral impurities and λ=2 for the electron scattered by ionized impurities [18]. The Seebeck coefficient of metal and degenerate semi-conductor can also be expressed in terms of effective mass m^* as,

$$S = \frac{8\pi^2 {\kappa_B}^2}{3e\hbar^2} m^* \left(\frac{\pi}{3n}\right)^{2/3} \qquad (1.2.13)$$

with $$g(E) = \frac{(m^*)^{3/2}}{\pi^2 \hbar^3} \sqrt{2E} \qquad (1.2.14)$$

The ZT value depends on the carrier's group velocity through electrical conductivity, the value of E_F that maximizes ZT is somewhat different from the value that maximizes the Seebeck coefficient (S) and the effective mass (m^*) [18].

1.2.2.4 Thermal Conductivity

Thermal conductivity gives the heat transport in solids. The thermal conductivity ($\vec{\kappa}$) is related to the heat-current density ($\vec{j}$) flowing through the material and the temperature gradient $\left(\partial T/_{\partial r}\right)$ in the material as,

$$\vec{j} = -\vec{\kappa}\left(\frac{\partial T}{\partial r}\right) \qquad (1.2.15)$$

The total heat conduction in solids is carried out by both the carriers and lattice vibrations (phonons). The total thermal conductivity is given by the sum of thermal contributions from carriers and phonons as,

$$\vec{\kappa} = \overrightarrow{\kappa_e} + \overrightarrow{\kappa_l} \qquad (1.2.16)$$

The carriers in solids transport both the heat and electricity. The contribution of carriers in thermal conductivity can be computed from Boltzmann's transport equation as,

$$\overrightarrow{\kappa_e} = \frac{1}{4\pi^3 T}\int \tau\vec{\upsilon}\,\vec{\upsilon}(E - E_F)^2\left(\frac{\partial f_0}{\partial r}\right)d^3r \qquad (1.2.17)$$

For metals, the above equation boils down to Wiedemann – Franz relation,

$$\overrightarrow{\kappa_e} = \frac{\pi^2}{3}\left(\frac{\kappa_B}{e}\right)^2\vec{\sigma}T \qquad (1.2.18)$$

In the above equation, the ratio $(\frac{\kappa}{\sigma T})$ is known as the Lorenz number and is constant and is equal to 2.45×10^{-8} W Ω K^{-2}.

In case of semi-conductors, assuming parabolic bands and non-degeneracy where $|E - E_F|$ is replaced by E, the electronic contribution can be written as

$$\kappa_{exx} = \sigma_{xx}T\left(\frac{\pi^2\kappa_B^2}{3e^2}\right) = ne\mu_{xx}T\left(\frac{35}{2}\right)\left(\frac{\kappa_B^2}{e^2}\right) \qquad (1.2.19)$$

Except for the numerical constant, the electronic contribution to thermal conductivity is similar to that of metal [19]. However, for degenerate semi-conductors and for the bands with non-parabolicity, a careful treatment is required. A major difference between metal and semi-conductor heat transport by electric carriers is that in semi-conductors the electrical conductivity is much smaller, and usually phonon contribution is dominant.

In a material, the heat conduction is carried by both carriers and lattice vibrations, known as phonons. By using classical kinetic theory, the lattice contribution to thermal conductivity of a solid can by written as,

$$\kappa_l = \frac{1}{3} C_v v_s l \qquad (1.2.20)$$

where C_v is the specific heat capacity at constant volume, v_s is the velocity of sound, and l is the mean free path of phonons. At low temperatures, the lattice part of thermal conductivity is dominated by Debye T^3 law for C_v, because the phonon scattering is insignificant at low temperature due to the small number of phonons excitations and due to their long wavelengths. At high temperatures (at a temperature higher than Debye temperature), the heat capacity of the solid and the velocity of sound of typical materials becomes essentially constant. Thus, the lattice part of thermal conductivity at higher temperatures is determined by phonon's mean free path. The minimum lattice thermal conductivity can be achieved when the phonon mean path is comparable to the interatomic distances in a crystal.

In a perfect infinite crystal at zero K temperature, the phonons would move without scattering, making thermal conductivity infinite. However, real crystals have different scattering mechanism which reduces the thermal conductivity significantly. The scattering

mechanisms involve the scattering of carriers and phonons. The major phonon-scattering mechanisms are phonon-phonon scattering, phonon-boundary scattering, and phonon-defect scattering. Those scattering mechanism will be discussed as below.

1.2.3 Scattering Mechanism

The scattering of electrons directly affects the electrical conductivity and Seebeck coefficient, while the scattering of phonon affects the thermal conductivity. This indicates that the scattering of carriers and phonon are important transport behavior to study. In this section, we will discuss different types of scattering mechanism.

1.2.3.1 Carrier-scattering Mechanism

The carriers in solids (electrons or holes) scatter through different mechanisms such as carrier-carrier, carrier-phonon, carrier-impurity, and carrier-defect [20]. Out of the many scattering processes, electron-phonon scattering process is most important. In metals, most of the Brillouin zone is occupied by electrons while it is mostly empty for semi-conductors. In metals, scattering takes place from one point to another on the Fermi surface with large momentum changes. But, for semi-conductors, the change in momentum wave vectors occurs only at a small angle, which makes the small angle scattering process very important.

Scattering probabilities for more than one scattering process is additive and proportional to the reciprocal of respective scattering time. So, the total scattering time can be written in terms of individual scattering time τ_i as,

$$\frac{1}{\tau_{total}} = \frac{1}{\tau_1} + \frac{1}{\tau_2} + \cdots \ldots \ldots \ldots \ldots + \frac{1}{\tau_i} \qquad (1.2.21)$$

In the electron-phonon scattering process in semi-conductors, the probability that an electron changes its state from initial to final state is proportional to availability of states, probability of absorbing or emitting phonon, and the strength of the electron phonon interaction. Some other well-known scattering processes are acoustic phonon scattering, optical phonon scattering, inter-valley scattering from one equivalent conduction band minima to another, scattering by dislocations, boundary scattering, and carrier-carrier scattering. Inter-valley scattering requires phonons with large momentum which consequently results in a large energy transfer. The details of each scattering mechanism are beyond the scope of this dissertation.

1.2.3.2 Phonon-Phonon Scattering

In most semi-conductors, at high temperature, phonon scattering is primarily dominated by its collision with other phonons. In the so-called normal process, the energy and momentum are conversed in the collision. Thus, the normal process only redistributes the phonons without introducing thermal resistance. But, in the so called Umklapp process, only the energy is conserved. Thus, the momentum which is not conserved, determines the high temperature thermal conductivity. Peierl's theory predicted that the lattice part of thermal conductivity at a temperature higher than Debye temperature should vary as 1/T.

Based on phonon – phonon scattering at high temperatures, an approximate relation for lattice thermal conductivity can be expressed as [21],

$$\kappa_l = B\frac{T_m^{3/2}\rho^{2/3}}{A^{7/6}} \qquad (1.2.22)$$

and

$$B = \frac{R^{3/2}}{3\gamma^2 \varepsilon_m^3 N_0^{1/3}} \qquad (1.2.23)$$

where ρ is the density, T_m is the melting temperature, A is the mean atomic weight, R is the universal gas constant, and γ is the Gruneisen parameter. The Gruneisen parameter measures the anharmonicity of the lattice vibrations, ε_m is a constant and is more or less the same for all materials (from Lindemann melting rule), and N_0 is the Avogadro's number. T_m, ρ, and A are easy to measure once the sample is measured. B is almost constant and does not vary too much from one material to another.

Generally, the thermal conductivity falls with increasing atomic weight, and also falls with increasing ionicity of the bonds. As shown in Fig. 1.2.4, the lattice thermal conductivities of the alkali halides are much lower than those of diamond-type elements and the III-IV compounds. This suggests that the ionic compounds should have a higher figure-of-merit than covalent semi-conductors. But, covalent materials usually have high carrier mobility and therefore have higher carrier thermal conductivity.

1.2.3.3 Umklapp Scattering

From the second-order perturbation theory, the relaxation time for three phonons Umklapp scattering at temperatures ≥300 K is given by [22],

$$\frac{1}{\tau_U} = 2\gamma^2 \frac{\kappa_B T}{\mu V_0} \frac{\omega^2}{\omega_D} \qquad (1.2.24)$$

Here γ is the Grüneisen anharmonicity parameter, μ is the shear modulus, V_0 is the volume per atom, and ω_D is the Debye frequency.

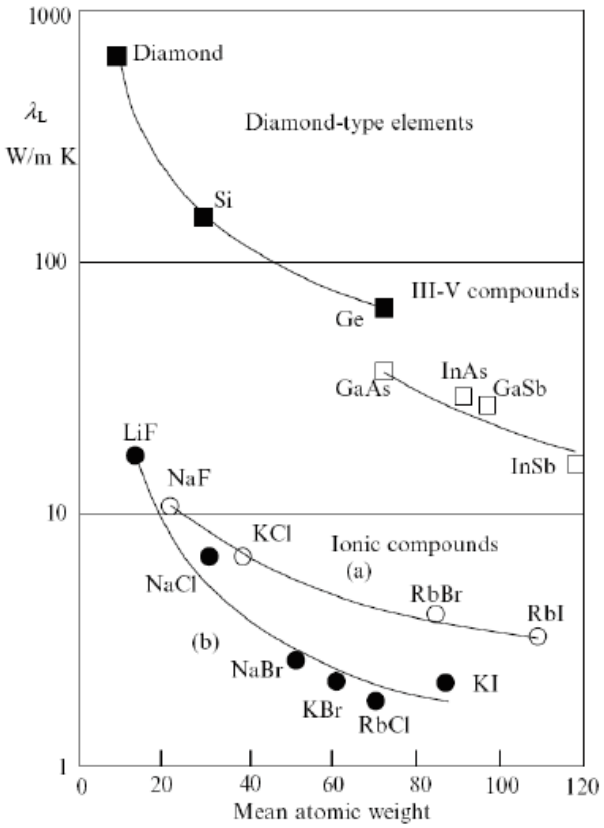

Fig. 1.2.4 Plot of lattice thermal conductivity against mean atomic weight for certain covalent and ionic crystals. The lattice thermal conductivity of diamond type compounds is much higher than that of ionic compounds. Fig. taken from Ref. 2.

1.2.3.4 Phonon- boundary Scattering

Phonon scattering at crystal boundaries is also an important scattering process, especially in samples prepared by powder processing. Due to scattering, the maximum mean free path of phonons is determined by the grain size of a poly-crystalline sample. The crystal boundaries not only scatter the phonons but also the carriers, which lowers the carrier mobility. However, the reduction in thermal conductivity outweighs the reduction in

mobility by carrier scattering which in turn improves the performance of thermoelectric devices [7]. The boundary scattering relaxation time is given by,

$$\frac{1}{\tau_B} = \frac{v}{D}(1-p) \qquad (1.2.25)$$

where D is the average grain diameter, υ is the group velocity of phonon, and p is the parameter that characterizes the interface roughness and its effect on the phonon boundary scattering [23]. The value of p represents the probability that the phonon is undergoing specular scattering at interface. The value of *1-p* represents the probability of the phonon that undergoes diffusive scattering. In case of purely diffusive scattering, the above equation [1.2.25] boils down to the well-known Casimir limit [24],

$$\frac{1}{\tau_B} = \frac{v}{D} \qquad (1.2.26)$$

1.2.3.5 Defect-phonon Scattering

Defect-phonon scattering process includes a variety of crystal defects, impurity sites, and different isotopes of the host material [22]. The phonon-relaxation time for this kind of point-defect scattering is given as,

$$\frac{1}{\tau_D} = \frac{V_0 \Gamma \omega^4}{4\pi\upsilon^3} \qquad (1.2.27)$$

where Γ is the strength of point-defect scattering given by

$$\Gamma = \sum_i f_i \left[\left(1 - \frac{M_i}{M}\right)^2 + 2\left\{6.4\gamma\left(1 - \frac{R_i}{R}\right)\right\}^2 \right] \qquad (1.2.28)$$

Here M_i and R_i are the mass and Pauling ionic radius of i^{th} impurity atom, and f_i is the fractional concentration of impurity atoms.

1.2.4 Thermoelectric Figure-of-Merit

The ability of a thermoelectric material to convert heat into electricity is gauzed by a dimensionless figure-of-merit, *ZT* defined as,

$$ZT = \frac{S^2\sigma}{\kappa}T \qquad (1.2.29)$$

where *S* is the Seebeck coefficient, σ is the electrical conductivity, κ is the total thermal conductivity, and *T* is the absolute temperature. To maximize the efficiency of the power generator and the coefficient of performance of a refrigerator, a material with high *ZT* value is required. This condition is fulfilled if a material has high Seebeck coefficient, high electrical conductivity, and low thermal conductivity. The main experimental focus of the present work is to improve the material properties to enhance the *ZT* of skutterudites by using different techniques.

As discussed above, a good thermoelectric material requires a high power factor ($S^2\sigma$) and low thermal conductivity (κ). But, the inter-relationship between various physical parameters (S, σ, and κ) makes the optimization of *ZT* really challenging. Fig.1.2.5 shows the variation of different physical parameters (S, σ, κ, $S^2\sigma$, and *ZT*) as a function of carrier concentration (n). It is clearly seen from Fig.1.2.5 that increasing carrier concentrations not only increases the electrical conductivity but also increases the thermal conductivity and decreases the Seebeck coefficient, giving a low power factor and hence low *ZT* value. In a low carrier concentration region, the Seebeck coefficient is very high and thermal

conductivity is very low. But, the electrical conductivity is very low, making the power factor and hence *ZT* of the material system low. The maximum *ZT* can be achieved when the carrier concentration is in the range of 10^{19} to 10^{20} cm^{-3}. This carrier concentration is achieved in heavily doped semi-conductors, making them one of the best choices for thermoelectric applications. In semi-conductors, the electrical conductivities, carrier concentrations, and carrier type can easily be changed by changing the dopant and doping concentration without affecting other properties too much. By suitably tuning the doping level and dopants, a fairly high electrical conductivity (~10^5 S m^{-1}) with significantly higher Seebeck coefficient (~200 μV K^{-1}) and a low carrier contribution to thermal conductivity (~0.5 W m^{-1} K^{-1}) can be achieved.

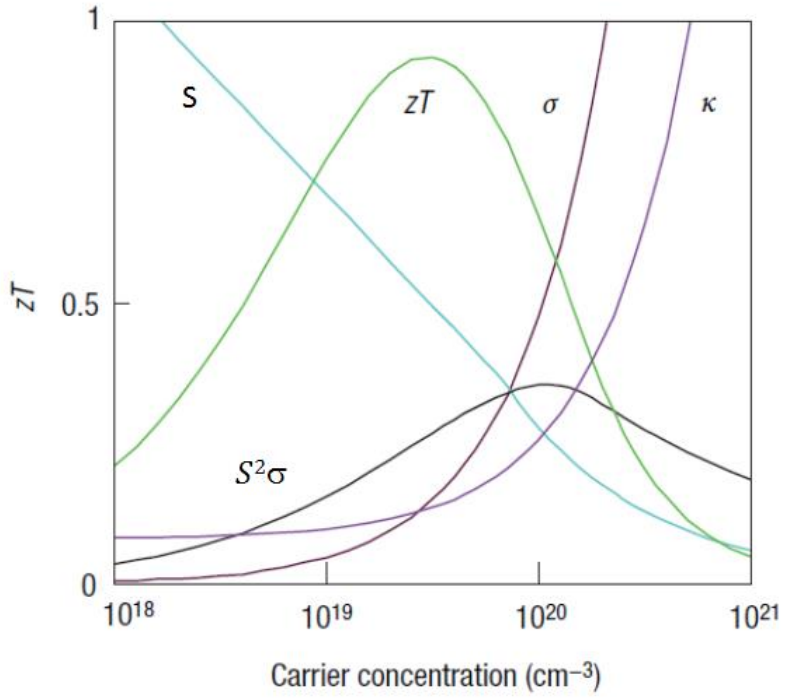

Fig. 1.2.5 Variation of *S*, *σ*, *κ*, $S^2\sigma$, and *ZT* as a function of carrier concentration (*n*).

1.2.5 Thermoelectric Devices

Thermoelectric devices consist of *p* and *n*-type of thermoelectric legs connected electrically in series and thermally in parallel, as shown in Fig. (1.2.6c). The thermoelectric devices are used either for power generation (Fig. 1.2.6a) or for thermoelectric cooling (Fig. 1.2.6b). The efficiency of a thermoelectric power generator is defined as the ratio of electrical power delivered to the load to the heat absorbed at the hot junction, given as,

$$`\eta = \frac{w}{q} = \frac{I^2 R_l}{K(T_{h-} T_c)+SIT_h} \qquad (1.2.30)$$

The efficiency of thermoelectric devices in terms of dimensionless figure-of-merit is given as,

$$\eta = \left(1 - \frac{T_c}{T_h}\right)\frac{(1+ZT)^{1/2} - 1}{(1+ZT)^{1/2} + \frac{T_c}{T_h}} \qquad (1.2.31)$$

The first term in the above Eq. (1.2.31) represent the Carnot efficiency, with the *ZT* given as, $ZT = \left(S^2\sigma/_{\kappa}\right)T$.

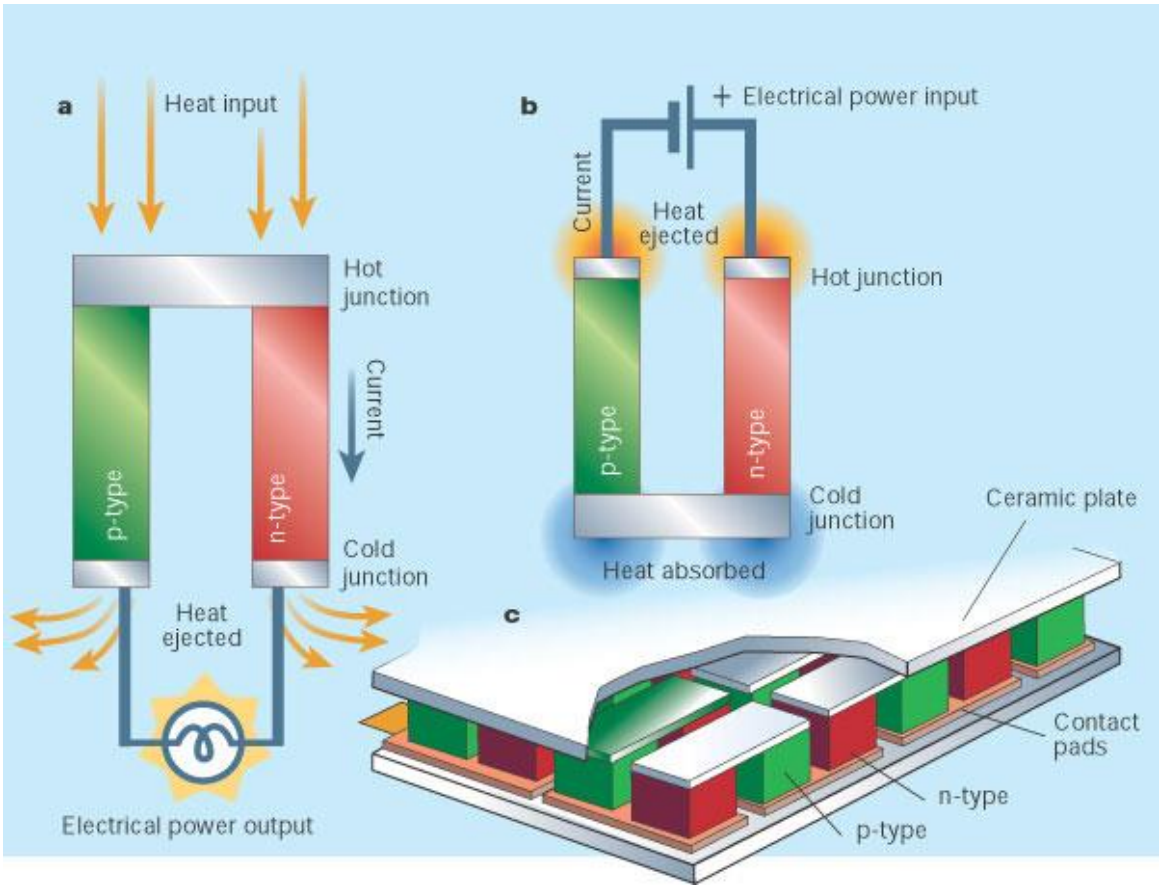

Fig. 1.2.6 Thermoelectric device a) for power generation, b) for active cooling, and c) thermoelectric module consisting *p* and *n*-type materials connected electrically in series and thermally in parallel.

Similarly, the efficiency of a cooling device is expressed in terms of the coefficient of performance (COP), which is defined as the ratio of cooling power produced to the rate at which electrical energy is supplied [6].

$$COP(\phi) = \frac{q}{w} \qquad (1.2.32)$$

where $$q = ST_c - \frac{1}{2}I^2R - K(T_h - T_c) \qquad (1.2.33)$$

and $$w = S((T_h - T_c) + \ I^2R \qquad (1.2.34)$$

With these values, the optimized COP with respect to electrical current is,

$$\phi = \frac{T_c\left[(1+ZT)^{1/2} - {T_h}/{T_c}\right]}{(T_h - T_c)\left[(1+ZT)^{1/2}+1\right]} \qquad (1.2.35)$$

From the Eqs. [1.2.31] and [1.2.35], we have clearly seen that conversion efficiency of a power generator and coefficient of performance of a cooling device directly depends on *ZT*, implying that higher *ZT* is required for the better performance of thermoelectric devices. Fig. 1.2.7 shows the efficiency of a thermoelectric device as a function of the temperature difference between source and sink for materials with different *ZT* values. For a temperature difference of 500 K and a *ZT* value ~10, the conversion efficiency of the generator is about 35%, comparable to the conversion efficiency of a steam engine.

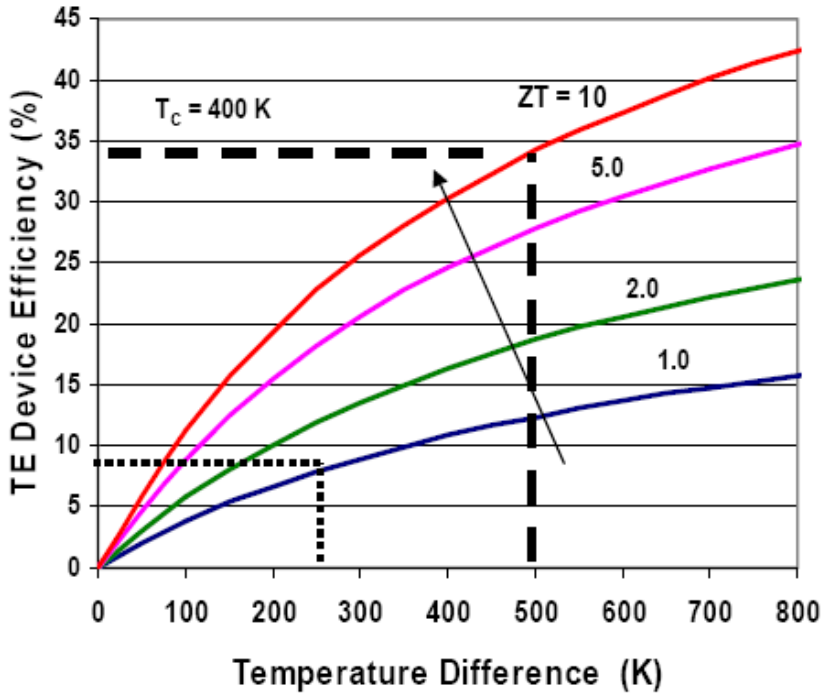

Fig. 1.2.7 Efficiency of TE device as a function of temperature difference for material with different *ZT* values.

The dimensionless figure-of-merit of some to the best state-of-art *n*-type and *p*-type thermoelectric material is summarized in Fig. 1.2.8.

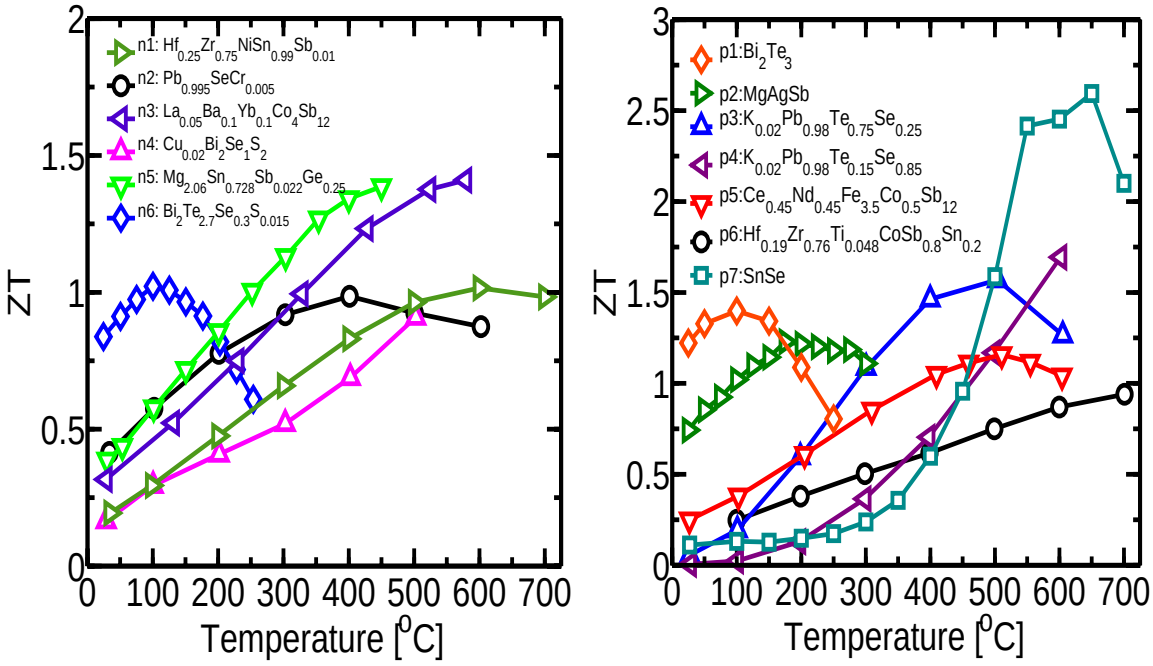

Fig. 1.2.8 State-of-art high *ZT* *n*-type and *p*-type materials. Figure courtesy Dr. Hee Seok Kim, post-doctoral fellow in Prof. Zhifeng Ren's lab.

1.2.6 Search for High Performance Thermoelectric Materials

For the systematic search of good thermoelectric materials, the transport parameters [Seebeck coefficient (S), electrical conductivity (σ), and thermal conductivity (κ)] should be expressed by more fundamental properties such as carrier concentration (n), band gap (E_g), mobility (μ), effective mass (m^*), and so on. Extensive work has been carried out to relate these parameters to practically useful parameters such as crystal structure or constituent elements both theoretically and practically [6], and a few general guidelines are

made to search for new or advanced thermoelectric materials with better performance. The following is a list of some of the most important guidelines.

Carrier concentration (*n*) should be in the range of 10^{18} to 10^{20} cm^{-3}, implying that heavily doped semi-conductors are the best thermoelectric materials, not metals and insulators.

The energy gap (E_g) should be in the order of $10\kappa_B T$ for better performance in refrigeration application, where κ_B and T are the Boltzmann constant and the absolute temperature, respectively. However, a high performance material employed in thermoelectric refrigeration is usually not suitable for power generation application.

Mobility, effective mass, and thermal conductivity: Since $Z \sim \frac{\mu}{\kappa_l}\left(\frac{m^*}{m}\right)^{3/2}$, a good thermoelectric material must have a good carrier mobility (μ), high effective mass (m*), and a low lattice thermal conductivity (κ_l).

Atomic weight: High average atomic weight materials are preferred since they will help in scattering high frequency phonons [1].

Crystal structure: Usually complex crystal structure alloys are preferable for phonon scattering. Also, materials with multi-valley band structure contribute to high performance.

1.2.7 Objectives and Organization of the Work

Most of the commercialized thermoelectric materials have *ZT* value around 1. This leads to quite a small efficiency and limits their applications in energy conversion. Skutterudites compounds, especially $CoSb_3$, has been identified as one of the novel thermoelectric materials. It has a great potential to be used in an intermediate high temperature range up

to ~550 ^{o}C, which is beneficial for extracting the waste heat from automobiles and from other industrial components.

The samples are prepared by melting-quenching-annealing-ball-milling and hot pressing the nano-powder in a graphite die using a DC hot press system. Making an ingot by melt-quench method will pre-alloy the elements which is further enhanced by the ball-milling process. The fine powder particles obtained through high energy ball-milling can lead to grain size confinement in the consolidated materials. Since the DC hot press method is a very fast process, the powders are sintered together in a short time period without a significant grain growth, which could help maintain the boundary interfaces to keep the thermal conductivity low.

Optimization of different sample preparation conditions such as ball-milling time, hot press temperature, hot pressing hold time, and hot pressing pressure were investigated. Once the best condition was achieved, further experiments were conducted to improve the thermoelectric performance of skutterudites by void filling and elemental substitution method. *p*-type skutterudites were also made through the substitution of Co or Ni by Fe. Some preliminary work on testing the mechanical properties of skutterudites material is presented Chapter 6.

In the last Chapter some work on exploring the contact alloy for Si-Ge will be discussed.

1.3 References

1. Ioffe, A. F., *Semi-conductor Thermoelements and Thermoelectric Cooling, Infosearch*, London, **1957**.
2. Rowe, D. M. (Ed.) CRC *Handbook of Thermoelectrics* **1995**, CRC Press, Boca Raton, FL, 157.
3. Rowe, D. M. *et. al.*(Ed.) CRC *Handbook of Thermoelectrics 2nd edition,* CRC Press Boca Raton, FL, 157, **2006.**
4. Nolas, G. S., Sharp, J., and Goldsmith, H. J. *Thermoelectrics: Basic principles and New Materials Developments* **2001**, Springer, New York.
5. Tritt. T. M. (Ed.) *Semi-conductors and Semimetals* **2001**, Vol. 69-71, Academic Press, San Diego, CA.
6. Goldsmith, H. J. *Thermoelectric Refrigeration* **1964**, Plenum Press, New York.
7. Dresselhaus et al., *Adv. Mater*. **2007**, 19, 1.
8. Hicks, L. D. and Dresselhaus, M. S. *Physical Review B* **1993**, 47, 12727.
9. Hicks, L. D. and Dresselhaus M. S. *Physical Review B* **1993**, 47, 16631.
10. Hsu, K. F. *et al. Science* **2004**, 303, 818.
11. Nolas *et al*, *J. Appl. Phys***. 1996**, 79, 4002.
12. Chen, G. *Phys. Rev. B: Condens. Mater. Sci* **1998**, 57, 14958.
13. Fluerial, J. P., Caillat, T., and Borshchevsky, A in *Proceedings of the 13th International Conference on Thermoelectric* **1994**, pp. 40.
14. Venkatasubramanian, R. *et al. Nature* **2001,** 413, 597.
15. Harman, T. C. *et al. Science* **2002,** 297, 2229.
16. Moss, T. S. *Handbook of Semi-conductors* **1992**, Elsevier Science Publishers, Amsterdam.

17. Cutler, N., and Mott, N. F. *Phys. Rev.*, **1969,** 181, 1336]

18. Mahan, G. D., and Sofo, J. O. *Proc. Natl. Scad. Sci. USA* **1996**, 93, 7436.

19. Tritt, T.M. *Encyclopedia of materials: Science and Technology*, **2002**.

20. Ashcroft and Mermin, *Solid State Physics*, **1976**.

21. Keyes, R.W. *Phys. Rev.* **1959,** 15, 564.

22. Sommerfeld, A. *Phys*. **1928**, 47, 1.

23. Rhodes, P. *Proc. Roy. Soc. A*, **1950**, 204, 396.

24. Covard, C *et. al. Phy. Rev. B* **2005**, 31, 2080.

Chapter 2

Measurement and Characterization of Thermoelectric Materials

2.1. Introduction

The efficiency of a thermoelectric (TE) device is related to the fundamental transport properties such as electrical conductivity (σ), Seebeck coefficient (S), and thermal conductivity (κ) of the material. To characterize the TE material, a detailed study on the various parameters such as electrical conductivity (σ), Seebeck coefficient (S), and thermal conductivity (κ) is required. These transport properties further depend on more fundamental parameters such as carrier concentration (n), mobility (μ), effective mass (m^*), and the specific heat capacity (C_p) of the material. The measurements are conceptually very simple but the results may vary considerably, particularly at high temperature where the thermal gradient contributes to the systematic inaccuracies. Thus, exploring principles and experiments to avoid those uncertainties to achieve precise measurements is extremely important.

One of the important aspects of reliable and accurate characterization is to identify and gauge the systematic errors in the experiment. To account the error in the measurement of the Seebeck coefficient and electrical resistivity, we used a standard sample made by Constantan whose data are available in literature [1]. The electrical resistivity and the Seebeck coefficient of our samples are generally lower than those of Constantan by an order magnitude of 2 and 3, respectively. Thus, if the measured value of electrical resistivity and the Seebeck coefficient of a standard Constantan sample does not vary

significantly from the reported value, we do not expect the measurement error of our material to be significant.

Another important aspect we need to consider about electrical and thermal transport properties lies in the crystallographic structure. For cubic crystals, the thermal and electrical transport properties are isotropic. But, for some of the crystals the transport properties measured in one direction is significantly different than from the other direction. For such crystals, measuring the thermal and transport properties along the same direction for both single crystals and the polycrystalline sample is necessary. Fortunately, skutterudites are cubic in structure; the transport properties are identical in all directions. Therefore, we do not need to consider the directional properties in skutterudites.

The electrical conductivity and the Seebeck coefficient from room temperature to about 550 ^{o}C is measured in the commercially available equipment ZEM-3 (Ulvac). The thermal diffusivity of the samples is measured using a commercially available laser flash (LFA 457, Netzsch) and the heat capacity at constant pressure is measured using a commercially available differential scanning calorimetry (DSC 400C, Netzsch). The carrier concentration and mobility in the samples are measured using commercially available Physical Property Measurement System (PPMS, Quantum Design). The microstructures of the samples are examined by using scanning electron microscopy (SEM) [LEO 1500, JEOL] and transmission electron microscopy (TEM) [JEM-2100F, JEOL]. The chemical composition of the samples is detected using an energy dispersive diffractometer [EDAX at JSM6330F, JEOL]. X-ray diffraction (X'pert pro, PANalytical) method is used to study the phase formation of the samples.

All the principles and experimental setup will be introduced in the remainder of this chapter.

2.2 Electrical Resistivity and Seebeck Coefficient Measurements

2.2.1 Principle of Electrical Resistivity Measurement

The four probe method [2] has been widely used for a long time to measure the resistivity of semi-conductors to minimize/eliminate the contact effect. The schematic representation of the four probe method is shown in Fig. 2.2.1. In Fig. 2.2.1, probe 1 and 4 measure the current flowing through the sample, while probe 2 and 3 measure the potential difference between these two points. To have a better contact of the voltage probes, they can be held in place either by using pressure, welding, or even by making a small hole in the sample [2]. During this measurement, we assume that the probes have negligible effects on the potential distribution and they are measuring the potential in the center, regardless of whatever is the thickness of the sample.

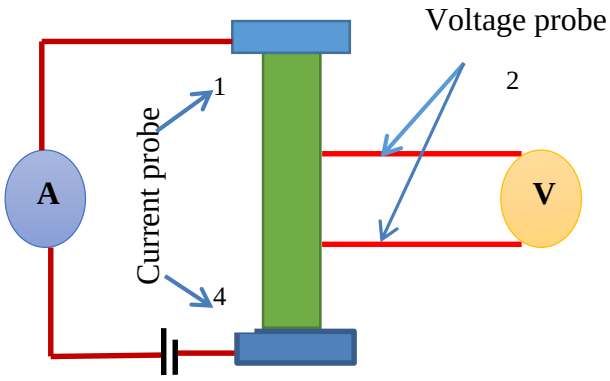

Fig. 2.2.1 Schematic of four probe measurement method.

In the case of thermoelectric research, the measurement of electrical conductivity is often challenging due to the Peltier effect produced by temperature gradient between two current probes when an electrical current passes through the sample. The temperature gradient will produce an additional Peltier voltage (V_o) which is added to the voltage V_r and V_H respectively during the electrical resistivity and Hall coefficient measurement. To take into account the Peltier voltage, alternate current is often used. However, small alternate voltage V_o is produced [3] because of the Peltier heat produced by the applied current. So far, the most dependable method to detect more accurate *Vr* is the high-speed, high-resolution dc measurement technique [4]. However, there are several other issues related to the accurate determination of correct voltage; for example, positions of the probes, surface conditions, methods of contacts, etc. For our experiments, we have measured electrical conductivity by using a commercial ZEM-3 (Ulvac) system [Fig. 2.2.1] based on high-speed, high-resolution current-switching dc measurement technique.

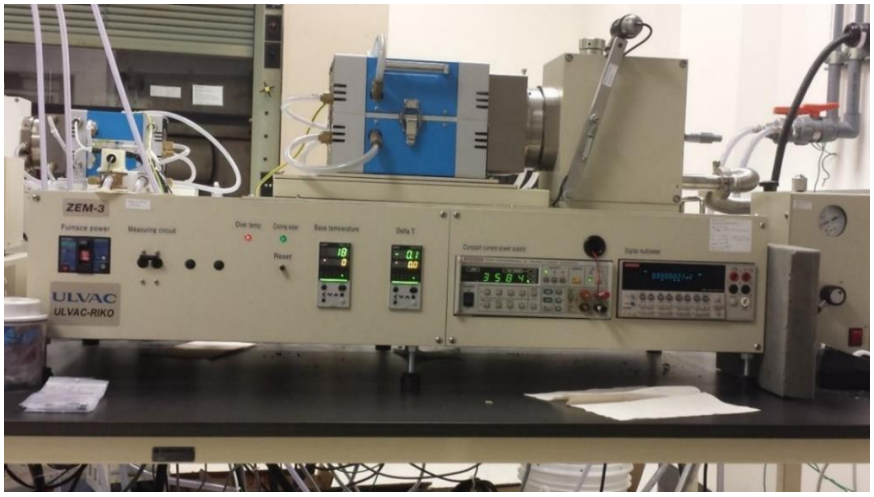

Fig. 2.2.2 Commercial ZEM-3 (Ulvac) system for electrical conductivity and Seebeck coefficient measurements.

In a ZEM-3 system, electrical conductivity is calculated by measuring the resistivity using the four probe technique [Fig. 2.2.1]. The four probe technique is developed to account for the resistance between the metal electrode and the semi-conductor samples. This intrinsic contact resistance, known as Schottky Barrier [5], is produced by the energy gap between the work function of the metal and the Fermi level of semi-conductor. The Schottky Barrier becomes more pronounced if the sample surface is oxidized. The contact resistance can be as much as hundreds of ohms, while the resistance of the sample is a few tens of milli ohms.

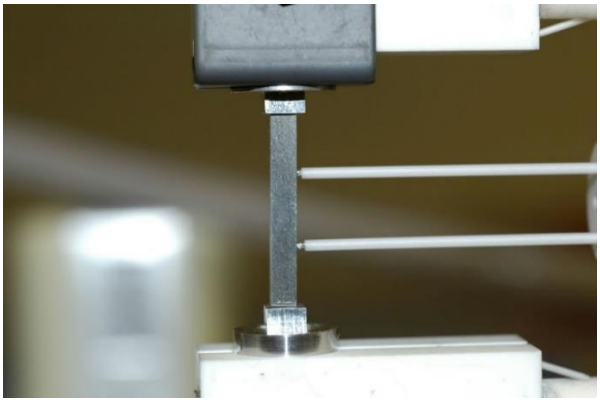

Fig. 2.2.3 Real sample mounted on ZEM-3 for measurement.

A real experimental set up for an electrical resistivity measurement is shown in Fig. 2.2.3. The sample is firmly held between the upper and lower electrodes. The complete set up is kept in the furnace as shown in Fig. 2.2.2 with low pressure He gas. The voltage and current controllers, data collection, and analysis are fully automated using a computer. The electrical resistivity is found from the relation

$$\rho = \frac{A}{l}\left(\frac{dV}{dI}\right) \qquad (2.2.1)$$

where $\left(\frac{dV}{dI}\right)$ is the slope of I-V plot, which gives the resistance (R), l is the distance between two voltage probes, and A is the cross sectional area of the sample. This set up is capable of measuring the resistivity at different temperatures where the temperature of the sample is measured using thermocouple. The electrical conductivity is then calculated by taking the reciprocal of ρ. The error in the measurement of electrical conductivity using ZEM-3 system is around 5%.

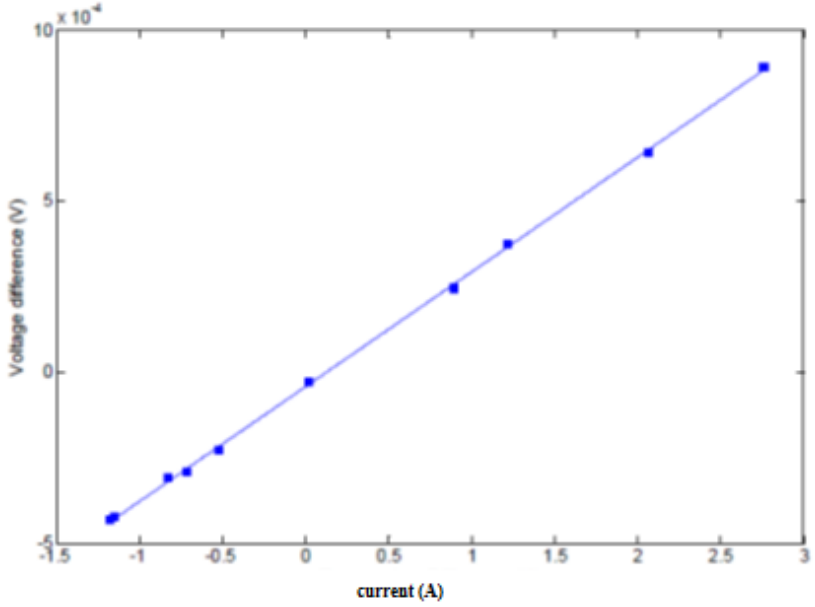

Fig. 2.2.4 I-V curve for current-resistance measurement.

As discussed earlier, the Peltier effect is one of the challenges encountered while measuring the electrical conductivity which causes a temperature gradient between two current probes when an electrical current is passed. The temperature gradient generates a Peltier voltage which is included in the measured voltage (V) across the resistance (R) and makes the voltage measurement inaccurate. The Peltier voltage for a small amount of current is

usually of the same order of magnitude as the resistive voltage (V_R). In ZEM-3, Peltier voltage is accounted by using a fast switching dc current. By this method, two equal and opposite Peltier voltages are produced for the same current and cancel each other by taking the average of two measured voltages across the resistance.

2.2.2 Principle of the Seebeck Coefficient Measurement

By definition, the Seebeck coefficient is measured as the potential difference (ΔV) developed as a function of temperature difference (ΔT) between the two measuring points. The precise measurement of the temperature difference between the two points makes it challenging to avoid the error in the Seebeck coefficient measurement. The contact resistance is the main problem for obtaining an accurate voltage measurement while the measurement of real temperatures at voltage probe is another important issue.

The schematic representation of the Seebeck measurement is shown in Fig. 2.2.5. The sample is placed vertically in between two electrodes, one at a higher temperature than the other, thus creating a temperature gradient in the sample. Thermocouples *A* and *B* are in contact with the sample by a pressure. These thermocouples are used to measure the temperature difference ΔT between two points in the sample. Concurrently, the two wires *A2* and *B2* measure the potential difference ΔV. *A1* and *B1* of two thermocouples are made by the same metal, while *A2* and *B2* are made from another kind of metal.

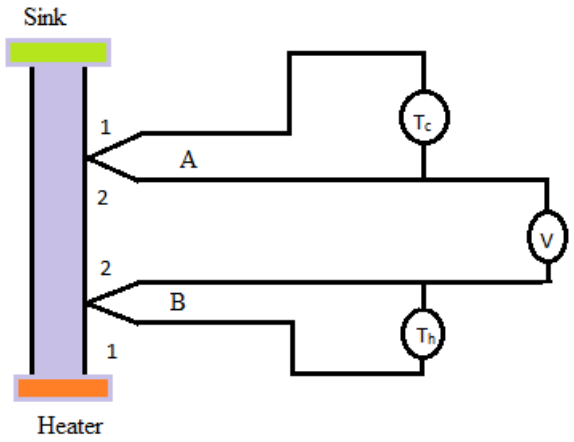

Fig. 2.2.5 Schematic setup of the Seebeck coefficient measurement.

A series of temperature gradients in the sample can be created by varying the output power heater. By doing so, a series of measurements of ΔT and ΔV will be achieved. A plot of ΔV as a function of ΔT is made which gives a straight line as shown in Fig. 2.2.6. The slope of the plot $d(\Delta V)/d(\Delta T)$ gives the Seebeck coefficient.

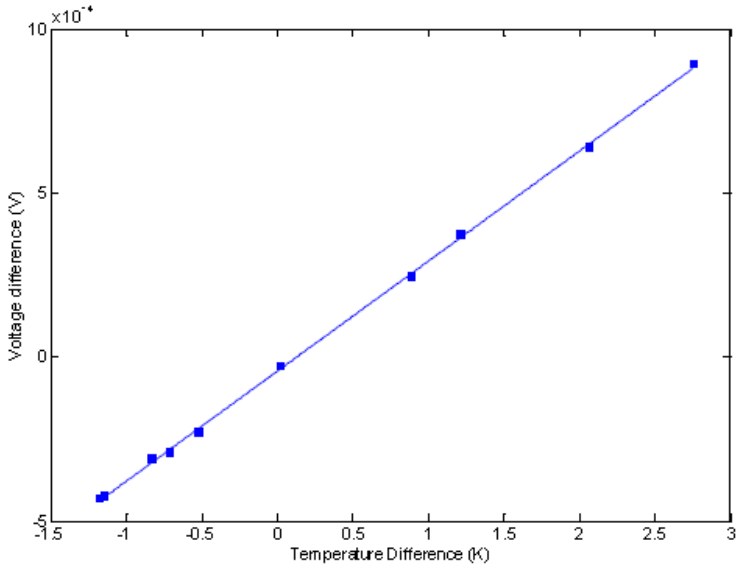

Fig. 2.2.6 ΔV-ΔT plot for the Seebeck coefficient measurement.

The error in the measurement of the Seebeck coefficient comes from the fact that the thermocouple may not take up the temperatures at the sample positions where the electric potential is measured [2]. Because of the heat radiation and transfer, the thermocouples measure the temperature between the thermocouples and the surrounding environments. To minimize this error, two methods can be applied [6]: a) evacuate the specimen enclosure to a pressure of about 10^{-4} torr or less, and b) use an extremely fine thermocouple wire. The error can also be minimized using thermocouple wires made from low thermal conductivity. By using the ZEM-3 system, the Seebeck coefficient can be measured within a precision of about 7%.

2.3 Thermal Conductivity Measurement

The thermal conductivity is defined as the amount of heat energy radiated per unit area per unit time per unit rise in temperature. The measurement of thermal conductivity is more difficult than the electrical conductivity measurement because the thermal insulation cannot be as good as the electrical insulation. A significant amount of heat is lost by different ways such as convection, radiation, and contacts. Thus the direct measurement of thermal conductivity requires extra care [7, 8].

The total thermal conductivity (κ) is given as the product of thermal diffusivity (α), mass density (ρ), and specific heat capacity (C_p) of the sample. The density of the sample is measured using Archimedes' kit. The development of the Laser flash method in 1961 by Parker has made the thermal diffusivity measurement of the bulk samples above ambient temperature very easy to find [9-11]. The laser source in the system eliminates the thermal

contact issue since a laser flash serves as the heat source. The heat loss through sample boundaries and the radiation is also minimized due to the quick measurement time. A simple sketch of the method is as shown in Fig. 2.3.1 and the picture of the equipment is as shown in Fig 2.3.2.

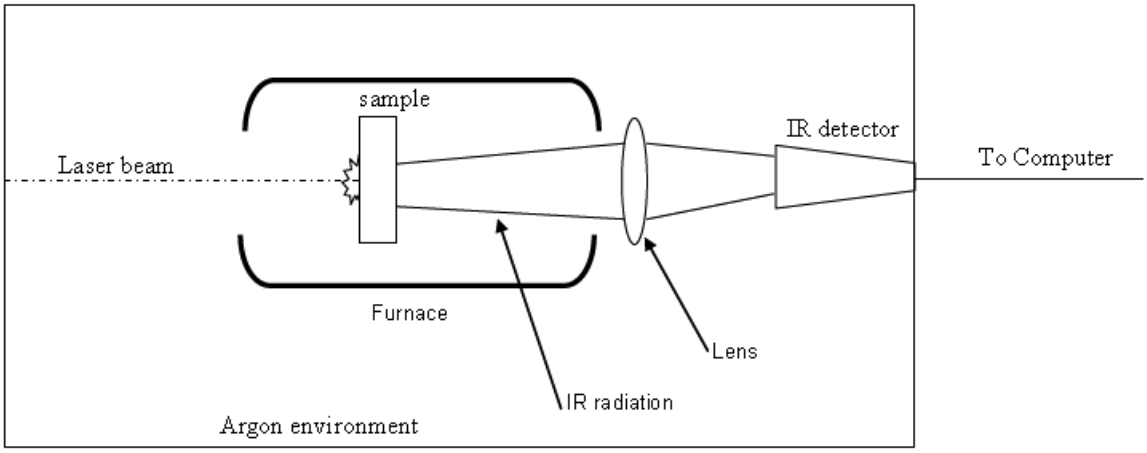

Fig. 2.3.1 Simple sketch of laser flash system

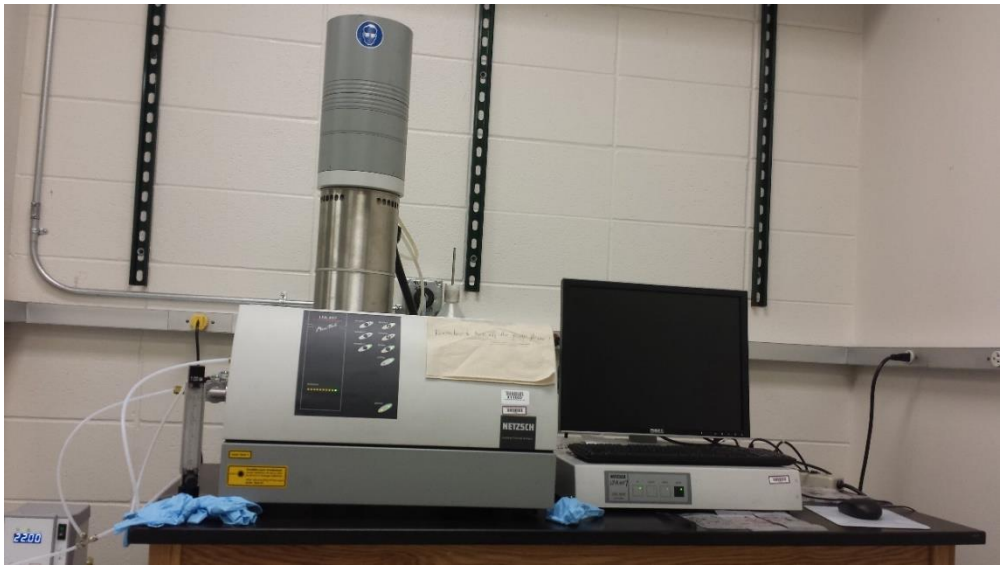

Fig. 2.3.2 Laser flash system [LFA 457, Netzsch]

In this method, the diameter of the sample is much larger than the thickness of the sample. The laser beam is irradiated on one face of the sample with pulses not more than a millisecond to minimize the heat loss and the temperature at the other face is measured with an IR detector as shown in Fig. 2.3.1. In the complete absence of heat loss from the sample, the temperature in the sample would rise monotonically to a limited value. But, in the real situation, the temperature will have a maximum value at certain T_{max} and then return to an ambient value as shown in Fig. 2.3.4. The thermal diffusivity of the sample is then calculated by using relation [12],

$$t_{0.5} = \frac{0.1388d^2}{\alpha} \qquad (2.3.1)$$

where $t_{0.5}$ is the time required to reach half of T_{max}, which can be found from Fig. 2.3.4, d is the thickness of sample, and α is the thermal diffusivity of the sample.

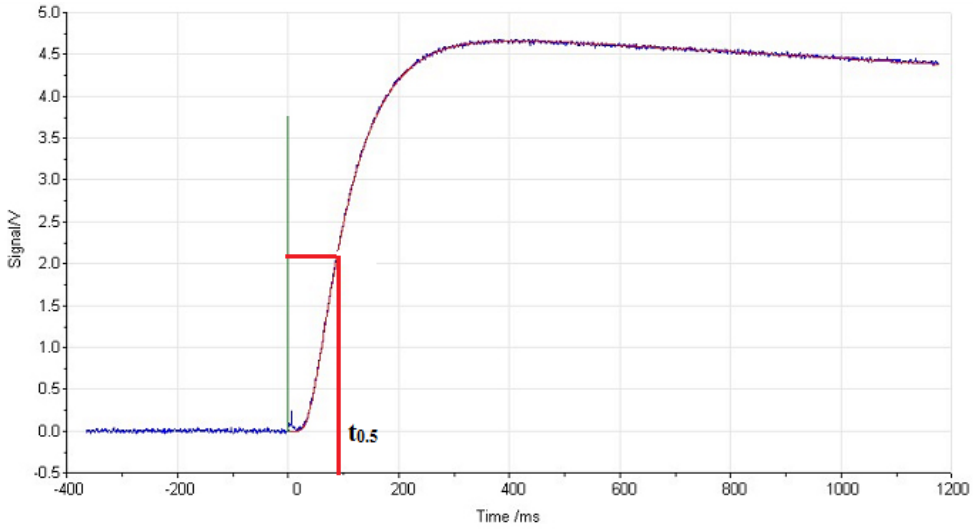

Fig. 2.3.3 Temperature-rise curve measured by an IR detector.

In the laser flash system, the laser spot is made uniform and has a greater area than the spot size of the temperature measurement to make approximately one-dimensional heat flow. Moreover, the sample must be thin enough that the heat pulse arrives before too much heat is lost and thick enough that the rise time is much greater than the laser pulse duration.

In the diffusivity measurement, the amount of energy from the laser beam does not need to be considered so the losses will not affect the measurement. However, the specific heat capacity is related to amount of laser energy (Q) by equation,

$$C = \frac{Q}{\rho d A \Delta T} \qquad (2.3.2)$$

Since laser energy is lost in various forms before hitting the sample, the specific heat measurement becomes inaccurate. In the laser flash technique the energy loss is taken into account by comparing the temperature-rise of the sample with a standard reference sample. Assuming that laser pulse energy (Q) and its coupling with both samples remain essentially unchanged,

$$Q = mC\Delta T = m_s C_s \Delta T \qquad (2.3.3)$$

$$C = \frac{m_s C_s}{m} \qquad (2.3.4)$$

where m is the mass of the sample and m_s and C_s are mass and specific heat capacity of the reference sample, respectively. The mass and specific heat capacity of the samples are known. With this information, the specific heat of the sample can be calculated using the temperature-rise plots of reference and actual samples.

In the experiment, a disc-shaped sample with a diameter ~12.7 mm and thickness ranging from 1-2 mm is used. All the samples together with the reference sample are coated with a graphite layer to absorb and match the absorptivity and emissivity of both samples, an important factor to be considered in specific heat calculation. The sample is put facing the laser beam and an indium antimonide (InSb) IR detector inside an argon environment furnace [Fig. 2.3.2]. A thermocouple in contact with the sample measures the temperature of the sample and its surroundings, and a heater is used to make the desirable furnace temperature for temperature-dependent diffusivity and the specific heat capacity measurement. A laser beam strikes and is absorbed by the front sample surface causing a heat pulse to travel through the sample's thickness. The resulting temperature is kept in optimum range of ~2 K by adjustable filters placed in between the sample and laser sources. The actual IR signal, which gives a temperature-rise curve, detected by the IR detector is shown in Fig. 2.3.4. The equipment is fully automated and controlled to record, analyze, and report the data of thermal diffusivity, specific heat and thermal conductivity is calculated using $\kappa = \alpha\rho C_p$ where α is the thermal diffusivity, ρ is the mass density, and C_p is the heat capacity at constant pressure.

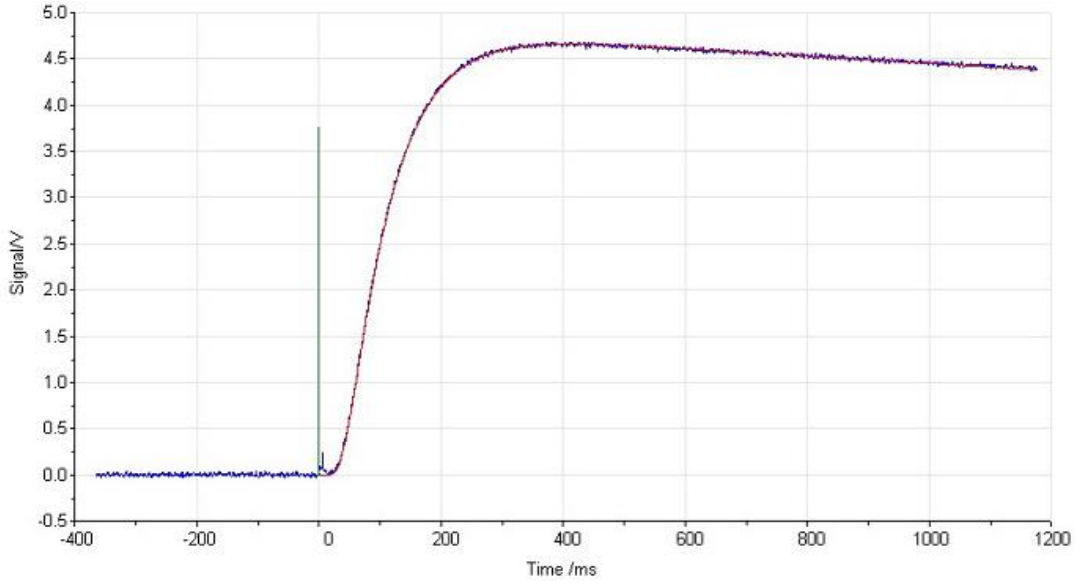

Fig. 2.3.4 Actual IR signal which gives temperature rise curve detected by an IR detector with respect to time.

Even though the laser flash technique is the most favored technique, there are a few issues related to accurate measurement of thermal diffusivity. A finite width of the laser pulse can affect the measurement of samples which are thin or have high diffusivity because the heating of the front surface cannot be considered instantaneous relative to the time to diffuse through the sample [13- 16]. Also, there are non-measurement errors related to heat losses and non-uniform heating [17]. These problems hinder the accurate determination of half time using the temperature-rise curve. These problems could be addressed using various models, the software used in the measurement system contains a set of theoretical analysis techniques to account for these issues. Then, the diffusivity measurement is corrected by choosing the right model that fits the experimental conditions and sample

properties. After all these corrections, the diffusivity and specific heat capacity can be measured with an accuracy of ~2% and 10% respectively using the laser flash system.

2.4 Specific Heat Capacity Measurement

The specific heat capacity of samples measured using laser flash method has a larger deviation ~10%. In order to get more accurate specific heat capacity measurement, DSC 400 C equipment from Netzsch Company is used. Fig. 2.4.1 shows the apparatus used for heat capacity measurement.

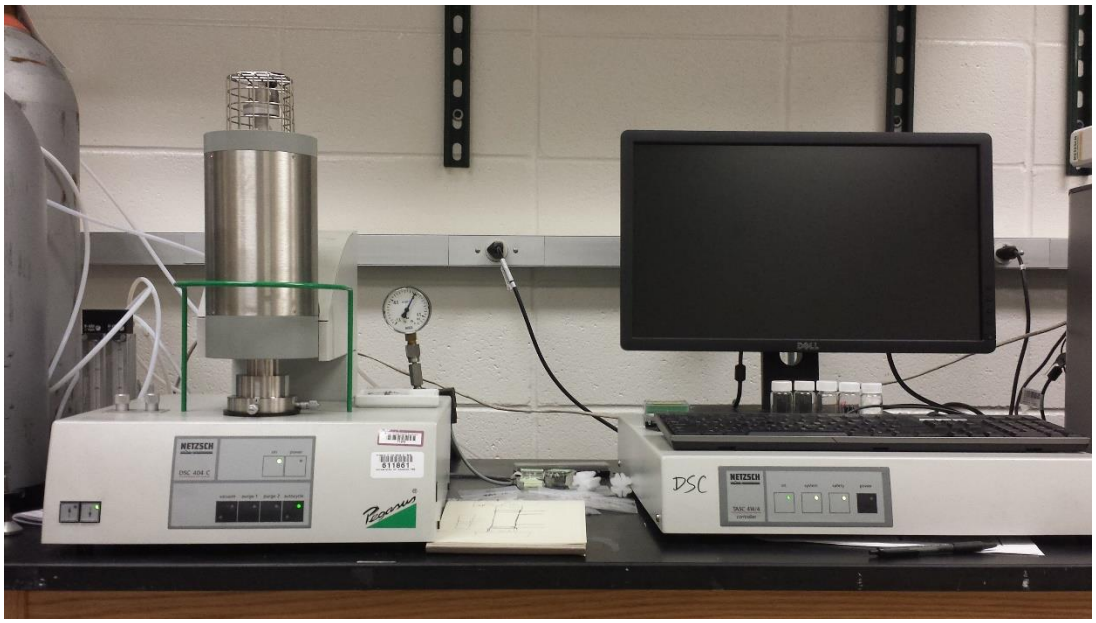

Fig. 2.4.1 DSC 400C (Netzsch) for heat capacity measurement.

The DSC system is a thermo-analytical technique in which the difference in the amount of heat required to increase the temperature of a sample and a reference are measured as a function of temperature [18]. Both the sample and reference samples are kept at nearly the same temperature throughout the measurement. The temperature program for DSC analysis

is designed so that the sample holder temperature increases linearly with time. The heat capacity of reference sample is well-defined over the temperature range to be scanned. In our system, the maximum temperature is 550 ^{o}C, and the standard sample is sapphire disc.

To minimize the error in the measurement of C_p, the sample dimensions should be comparable with that of a standard sample. In our case, the sample is polished to a small disk of about 6 mm diameter and a thickness of ~0.6-1.0 mm. Three measurements (baseline, the sapphire, and the sample) over the whole temperature range need to be collected. For accurate measurements of specific heat, all three measurements should be performed with the same crucibles under the same conditions. The specific heat capacity of the material is then calculated using the following formula:

$$C_p = \frac{Signal\ difference\ (sample - baseline)}{sample\ mass * heating\ rate * sensitivity}$$

where the sensitivity is calculated from the sapphire disc measurement and is given as,

$$Sensitivity = \frac{signal\ difference\ (sapphire - baseline)}{mass\ (sapphire) * heating\ rate * theoretical\ C_p(sapphire)}$$

There are always two crucibles: one for reference sample and the other for the sample to be measured. The reference crucible should be exactly the same as the one holding the sample and empty for all measurements. With all these conditions provided, the specific heat capacity of a sample can be measured within 2% using the DSC method.

2.5 Hall Coefficient Measurements

As mentioned in the previous chapter, the electrical conductivity, the Seebeck coefficient, and the thermal conductivity are related to some fundamental physical parameters such as carrier concentration (n), carrier mobility (μ), and effective mass (m^*) of the carrier. The Hall Effect measurement can be done to estimate the carrier concentration and carrier's mobility.

When a conductor carrying electric current is subjected to an external magnetic field, the moving charge carriers will be deflected and accumulate by Lorenz force to one side of the sample. A stable electric field perpendicular to both the electric current and magnetic field will build up due to the accumulation to counter the Lorenz force. The voltage developed is called Hall voltage. PPMS (Quantum Design) is used to measure the carrier concentration and mobility of carriers.

Fig. 2.5.1 PPMS (Quantum Design) for carrier concentration and mobility measurement.

A simple sketch of Hall Effect is shown in Fig. [2.5.2]

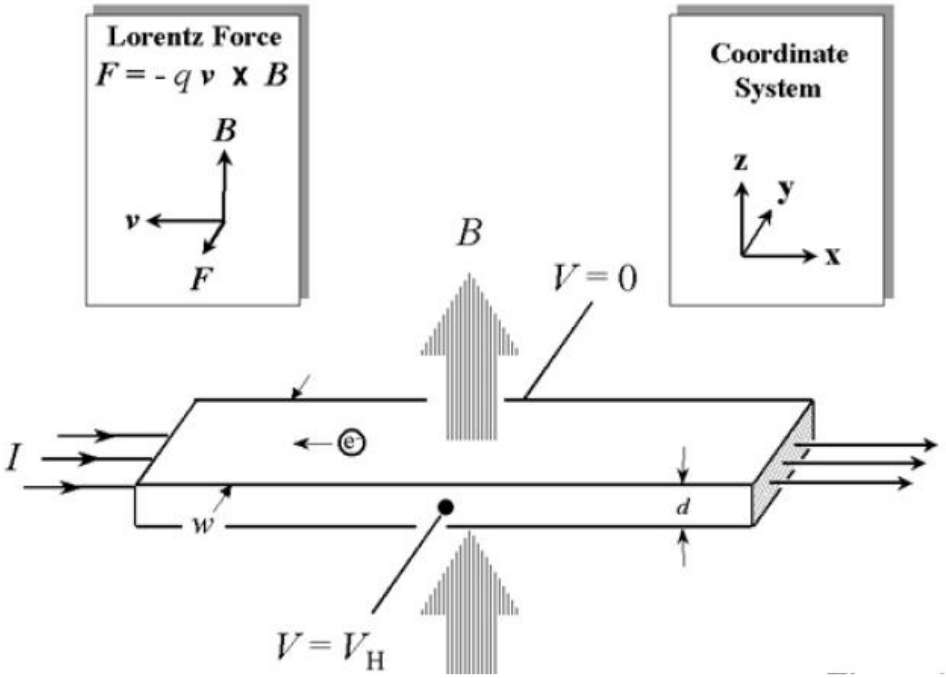

Fig. 2.5.2 Schematic of Hall Effect in a long thin bar of semi-conductor with four ohmic contacts. The direction of magnetic field is along z-axis and the sample has finite thickness.

If I is the current passed through the conductor of width w and thickness d, B is the applied magnetic field and V_H is the Hall voltage produced, then the Hall coefficient is calculated by using a relation

$$R_H = \frac{wV_H}{IB} \qquad (2.5.1)$$

and the carrier concentration is calculated by using equation

$$R_H = \frac{1}{ne} \qquad (2.5.2)$$

where e is the elementary charge of carrier. The electrical conductivity (σ) is found by measuring the voltage across the length of the conductor (l) by the equation

$$\sigma = \frac{V_l \,.\, w.\, t}{Il} \qquad (2.5.3)$$

Then, the mobility (μ) is calculated by the equation

$$\mu = \frac{\sigma}{ne} \qquad (2.5.4)$$

2.6 References

1. Muta *et al., J. Alloys and Compds*. **2003**, 359, 326.
2. Nolas, G. S., Sharp. J., and Goldsmith, H.J. *Thermoelectrics, Basic Principles and New Materials Development*, Springer **2001,** New York.
3. Herman, T. C. *Thermoelectric Materials and Devices*, Reinhold **1967,** New York.
4. Buist, R. J. *Thermoelectric News* **1991**, Thermoelectric Technology, Inc., 6.
5. Sze, S. M. *Physics of Semi-conductor Devices*, Wiley Inter-Science **1981,** New York.
6. Goldsmith, H. J. *Thermoelectric Refrigeration*, Plenum Press, New York, **1964**.
7. Goldsmith H. J. *Proc. Phys. Soc. London Sec. B* **1956**, 69, 203.
8. Bowers, R., Ure, R.W., Bauerle, J. E., and Cornish, A. J. *J. Appl. Phys*. **1959**, 30, 930.
9. Righini, F., and Cezarliyan, A. *High Temp-High Pressure*. **1973,** 5, 481.
10. Taylor, R. E. and Maglic, K. D. in *Compendium of Thermo-Physical Property Measurement Method*, Vol. 1, Plenum Press, NY, **1984** pp 305.
11. Taylor, R. in *First European Conference on Thermoelectrics*, London, **1987** pp 107.
12. Parker, W. J. *et al*., *J. Appl. Phys*. **1961**, 32, 1679.
13. Cowan, R. D. *J. Appl. Phys.* **1963**, 34, 926.
14. Taylor, R., and Clark, L. *High Temp-High Pressure*. **1974**, 6, 65.
15. Clark, L., and Taylor, R. *J. Appl. Phys.* **1975**, 46, 714.
16. Koski, J. A., *in Proc. 80th Symp. Thermophysical Prop*. **1981**, Vol II, Amer. Soc. Mech. Eng., NY.
17. K. Kobayashi, *The Japan Society of Mechanical Engineers II*, **1991**, 31, 1.
18. O'Neill, M. J. *Anal. Chem*. **1964**, 36, 1238.

Chapter 3

Preparation of $CoSb_3$-based Skutterudites and Thermoelectric Properties of $Yb_xCo_4Sb_{12}$ and $CoSb_{2.8}Sn_xTe_{0.2-x}$

A part of this chapter contains our previously published works: *Thermoelectric property enhancement Yb doped n-type skutterudites $Yb_xCo_4Sb_{12}$, Acta Materialia* ***75****, 321 (2014)* and *Substitution of antimony by tin and tellurium in n-type skutterudites $CoSb2.8Sn_xTe_{0.2-x}$, JOM* ***66****, 2282 (2014).*

3.1 Introduction

Thermoelectric materials directly convert heat into electricity and offer a reliable solid state means for power generation and cooling. Their uniqueness in operation such as no moving parts, silence in operation, economic, environmentally friendly, and reliability have made thermoelectric materials promising for practical application.

The thermoelectric materials used for commercial devices are Bi_2Te_3-Sb_2Te_3 alloys for refrigeration and Si-Ge - based alloys for power generation at high temperature. However, the dimensionless figure-of-merit of these materials is low and thermoelectric devices made using those alloys have very low efficiency, lower than the efficiency of steam engines. So, an intense research worldwide has identified several materials which can potentially use in thermoelectric devices to further enhance the device efficiency.

In mid-1990's, two important theories were proposed to improve the material properties [1, 2], which aroused the further experiments in the field. Slack proposed the phonon glass electron crystal (PGEC) concept, a paradigm in which electrical transport is akin to that of a crystalline solid, while the thermal transport is similar to that of glass [2]. Filled skutterudites is one of the PGEC materials, indicating that skutterudites could be one of the prominent thermoelectric materials for device application.

This chapter will focus on experiments carried out to investigate and optimize the $CoSb_3$-based skutterudites system and explore the mechanism which could substantially reduce thermal conductivity while keeping the power factor unaltered so that the dimensionless figure-of-merit, *ZT*, can be improved significantly.

3.2 General Properties of $CoSb_3$-based Skutterudites

3.2.1 Introduction

The skutterudites compound derives its name from naturally occurring mineral, $CoAs_3$, first found in Skutterud, Norway. Binary skutterudites are body-centered cubic that belong to the space group *Im3* and are of the form MX_3, where M is the metal atoms such as Co, Rh, or Ir, and X represents the pnictogen atoms such as P, As, and Sb. The crystal structure of skutterudites is as shown in Fig. 3.2.1. Only six out of eight cubic boxes are occupied with Sb rings, giving two voids in the structure.

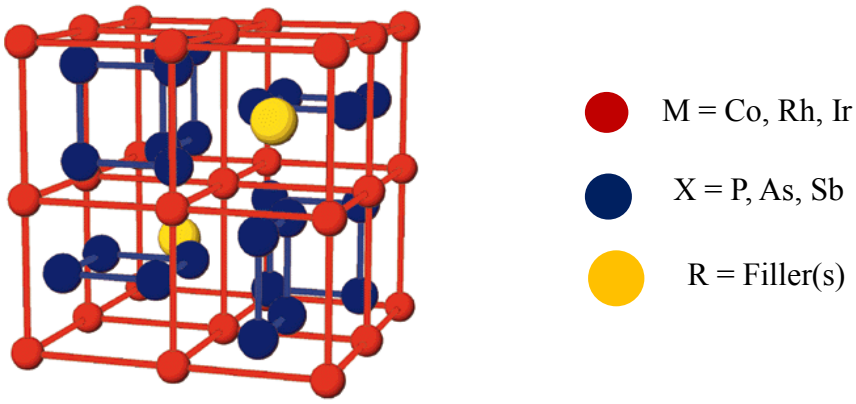

. **Fig. 3.2.1** The unit cell of binary skutterudites of structure. The metal atoms (red solid circle) form a simple cubic sub lattice. The pnictogen atoms (blue solid circles) are arranged in planner rectangular four membered rings that form linear array along the (100), (010), or (001) crystallographic directions.

Thus, the general formula for skutterudites is $RM_4X_{12,}$ where *R* is the void and can be filled with varieties of guest atoms [3, 4, 5]. By filling the voids, simultaneous tuning of electrical transport properties and thermal transport properties is possible. The filled atom mainly does two tasks. First, it donates carriers to the host frame, which alters the carrier concentration, mobility, and scattering rate of the carriers and tunes the electrical property. Second, the filled atom is loosely bound with the Sb ring by a spring constant, and starts to vibrate about its mean position. If the frequency of vibration of the rattler is close to the soft mode vibration of Sb rings, a broad range of phonons will be scattered, thus lowering the lattice thermal conductivity. Another approach to tune the thermoelectric properties of skutterudites can be achieved by distorting the Sb-planner ring. The elemental substitution

method has been proven to be an effective way to enhance the phonon scattering via alloy effect and mass fluctuation scattering, leading to an improved *ZT* value [6, 7]. The details of the elemental substitution method will be discussed later in this chapter.

3.2.2 Crystal Structure

Generally, binary skutterudites are semi-conductors with small band gaps of ~0.1-0.2 eV, high carrier mobility, and a relatively high Seebeck coefficient. However, the thermal conductivity of the skutterudites system is very high. Nevertheless, the presence of two voids per unit cell of skutterudites structure makes it one of the potential material for thermoelectric materials. As discussed earlier, filling the voids with foreign elements suppresses the lattice thermal conductivity significantly and tunes the electronic properties to improve the power factor, leading to an enhanced figure-of-merit, *ZT*.

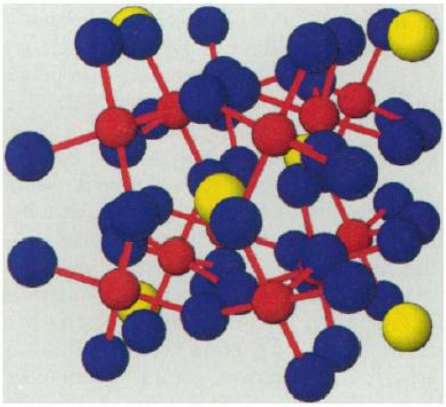

Fig. 3.2.2 Crystal structure of filled skutterudites. Large yellow spheres represent filler atoms, Sb atoms are depicted by blue spheres, and red spheres represent Co or Fe. The vibration of filler(s) atom markedly reduces lattice thermal conductivity. Fig. is taken from Ref. 10.

The reduction in lattice thermal conductivity depends on how effectively an atom can rattle about its mean position. The atomic displacement parameter (ADP), which measures the mean square displacement amplitude of an atom about its equilibrium lattice site, depends on how strongly the atoms are vibrating. Generally, the ADP values of the ions increases with decreasing ionic size. If the ionic radii of the caged element is small, they may rattle and interact with lattice phonons significantly, causing a substantial phonon scattering and leading to an improved *ZT* values [8]. Fig. 3.2.3 shows the temperature-dependent ADP in $La_{0.75}Fe_3CoSb_{12}$. The ADP values of La are larger than that of Fe, Co, and Sb and increases for all elements with increasing temperature, indicating that ADP is strongly temperature-dependent. The larger ADP value of the La suggest that La is loosely bounded with the host and its rattling about its mean position and therefore creates localized dynamic disorder.

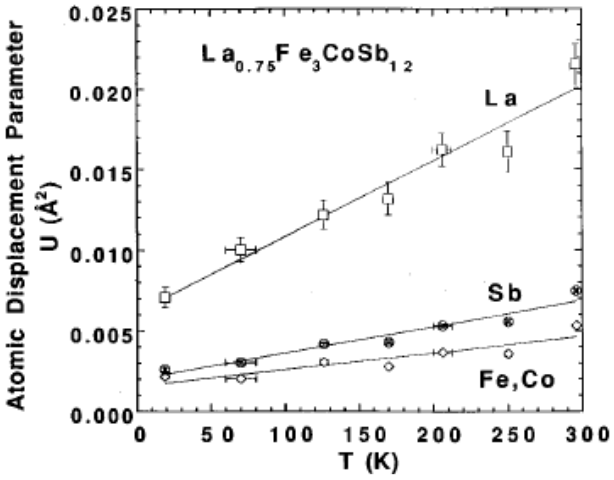

Fig. 3.2.3 Atomic displacement parameter obtained on a single crystal of $La_{0.75}Fe_3CoSb_{12}$. The large value of ADP of the La atom is an indication of the rattling of La in an oversized atomic cage.

The atomic displacement parameter strongly depends upon the atomic mass and ionic radii of the fillers caged in the void. Schnelle *et.al*,. [9] studied the effect of atomic mass and ionic radii of various fillers in ADP of skutterudites. It is observed that the ADP of Ba is much smaller than Ca, which is due to the higher mass of Ba. Likewise, one expects smaller ADP in Yb than La since Yb is heavier than La. This phenomenon can be understood by considering the ionic radii of fillers. Since the ionic radius of La is larger than Yb, its confinement in the void is much tighter than Yb, resulting in smaller vibration leading to lower ADP. Thus, while filling the void, attention should be paid to choose the filler(s) with suitable atomic mass and ionic radii. In fact, the filler atoms are loosely bounded with the Sb-planner ring and have Einstein-like vibration [10, 11]. If the vibrational frequency of filler is comparable to the vibrational frequency of soft mode phonons, substantial reduction in thermal conductivity is possible.

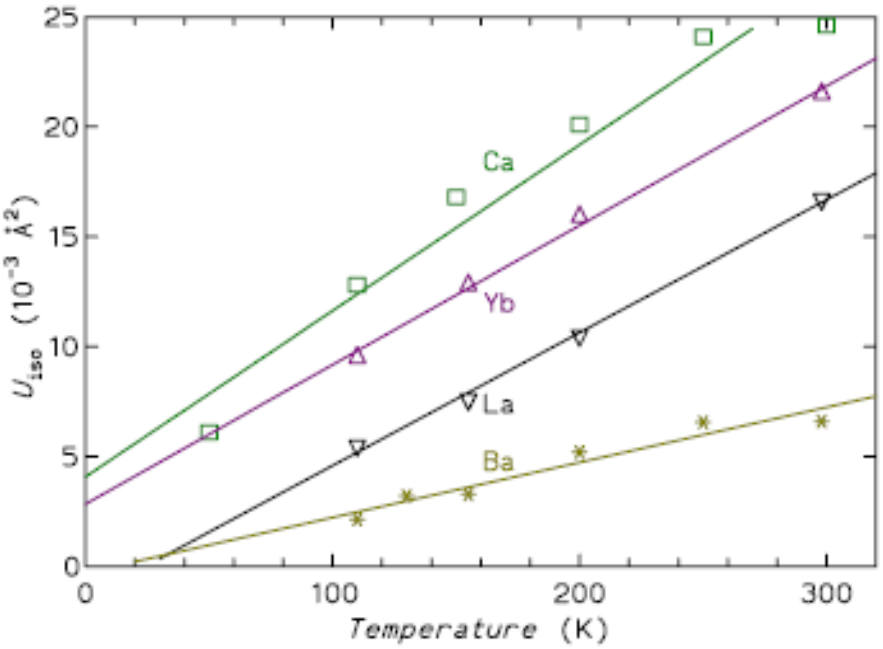

Fig. 3.2.4 Temperature-dependent ADP of MFe_4Sb_{12} (M=Ca, Ba, La, and Yb).The sample with lighter mass and smaller ionic radii shows much larger ADP.

3.2.3 Bonding and Band Structure

In skutterudites structure (RM_4X_{12}), each X atom has four nearest neighbors, two metal atoms and two nonmetal atoms situated at the corners of a distorted tetrahedron. Both M-X bond distances and the X-X bond distances are short and nearly equal to the sum of the covalent radii, indicating a strong covalent bond. However, the M-M distances are large, which indicates that the bonding between metal atoms is not significant. Each X atom (s^2p^3) contributes two of its valance electrons to bond with the two nearest neighbors in the X_4 groups via σ bonds. The remaining three electrons will participate in the two nearest M-X bonds. Since each metal atom is octahedrally coordinated by six X atoms, a total of (3/2)×6=9 X electrons are available for bonding in each MX_6 octahedral. The metal atoms M (d^7S^2) contribute 6×1/2=3 electrons to the bonding with 6 neighboring pnictogen atoms. All these electrons occupy the octahedral d^2sp^3 hybrid orbitals that are the essence of the M-X bonding.

The binary semiconducting skutterudites have very narrow band gaps. However, the band gap calculation shows that there is an indirect band gap of about 0.71, 0.57, and 0.73 eV for $IrSb_3$, $CoSb_3$, and $CoAs_3$, respectively [12]. In addition, there is a single band that crosses the gap and touches the conduction band near to the Fermi level. The presence of this band is reflected in the transport properties measurements. Based on measured the Seebeck coefficient, it was concluded that the conduction band is very flat, implying the large carrier effective mass and potential for excellent thermoelectric properties in *n*-type skutterudites [13]. However, the band crossing makes the Seebeck coefficient of *p*-type material less sensitive to carrier concentration than in the case of semi-conductors with

parabolic dispersion [14]. The electronic band-structure calculation performed on $LaFe_4P_{12}$ using tight binding approximation concluded that the compound was metallic having predominantly phosphorus character [15]. The band-structure calculation of $LaFe_3CoSb_{12}$ using the LAPW approach displays an indirect band gap of about 0.6 eV [16]. Similar to the conclusions of Harima [17], the highest occupied state is derived from bands with mostly Sb *p* character, but there are Fe/Co derived *d*-bands, whose tops are situated about 100 meV below the top of the *p*-like states. These *d*-bands states have a very low dispersion which results high effective mass of the carrier, leading to a high Seebeck voltage.

3.2.4 Thermal Conductivity

It is well known that $CoSb_3$ has relatively large thermal conductivity [18], which could be partially due to its covalent cubic crystal structure [14]. The lattice contribution to total thermal conductivity in $CoSb_3$ can be estimated by subtracting the electronic contribution from the total thermal conductivity. The electronic contribution of the carrier in thermal conductivity can be calculated by using Wiedemann-Franz relation, which is given by $\kappa_e = \sigma LT$, where σ is the electrical conductivity which can be measured using a four probe method, L is the Lorenz number, and T is the absolute temperature. The estimated lattice thermal conductivity in $CoSb_3$ suggests that thermal conductivity is far dominated by phonons. Even in heavily doped $CoSb_3$, the carrier thermal conductivity does not exceed more than 20% of total thermal conductivity. Thus, to lower the lattice contribution we must enhance the phonon-scattering mechanism. Several methods have been proposed to reduce the lattice contribution in the total thermal conductivity [19, 20]: a) by controlling the fine structures, the boundary scattering could be increased, b) point defect scattering

can be introduced by doping impurities and preparing solid solutions, c) charge carrier transfer from dopants in certain mixed-valance systems might enhance the phonon scattering, d) in heavily doped compounds, the electron-phonon scattering might be beneficial, and e) the intrinsic voids can be filled with loosely bounded atoms. The effect of fillers to suppress the lattice thermal conductivity in skutterudites was first demonstrated by using La as a rattler in $La_xCo_4Sb_{12}$ [21]. Experimental results show that even a small amount of La (x = 0.05) is enough to suppresses the lattice thermal conductivity by an order magnitude compared with unfilled skutterudites.

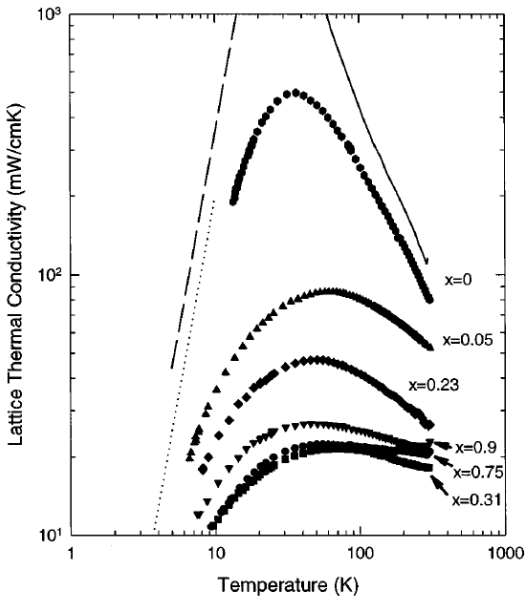

Fig. 3.2.4 Lattice thermal conductivity of $La_xCo_4Sb_{12}$ with x = 0.05, 0.23, 0.31, 0.75, and 0.9. Result shows that a small amount of filler is good enough to suppress the lattice thermal conductivity by an order magnitude compared with unfilled skutterudites.

Experiments were carried out to study the effect of filler(s) in lattice thermal conductivity of *p*-type skutterudites [8]. The observed suppression in lattice thermal conductivity was significant at lower temperature. At room temperature, the lattice thermal conductivity of fully filled or partially filled *p*-type skutterudites was about 6 to 8 fold smaller than unfilled $CoSb_3$.

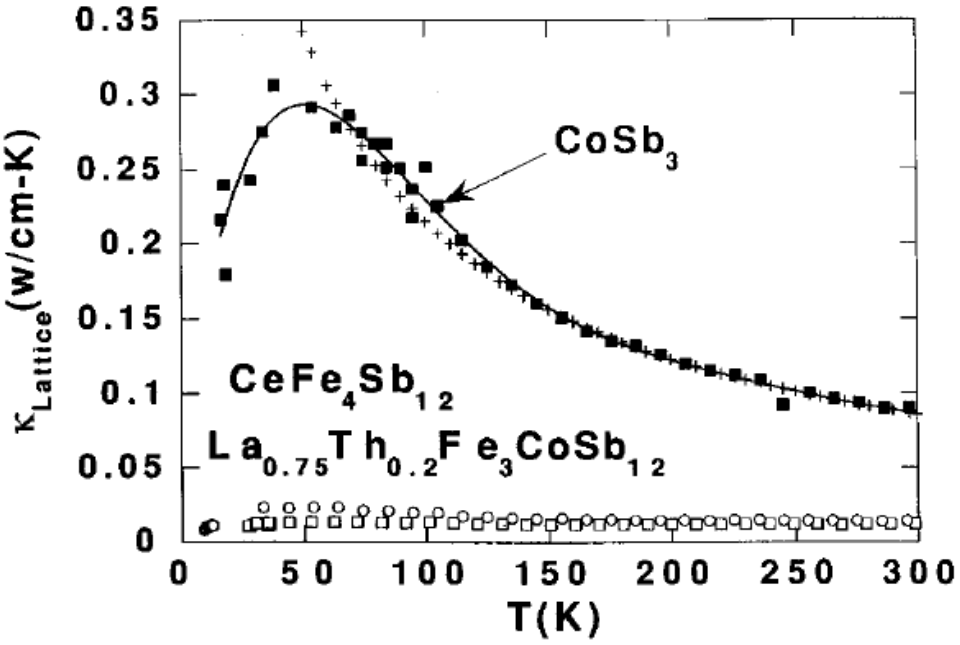

Fig. 3.2.5 Temperature-dependent lattice thermal conductivity of $CeFe_4Sb_{12}$ (open circle), $La_{0.75}Th_{0.2}Fe_3CoSb_{12}$ (open square), and unfilled skutterudites $CoSb_3$ (filled square). The lattice thermal conductivity in filled skutterudites is suppressed by 6-8 folds at room temperature compared to unfilled skutterudites.

As stated earlier, the significant enhancement on *ZT* can be achieved by reducing the lattice thermal conductivity which requires strong phonon scattering without affecting electron

scattering too much. The different phonon scattering mechanism described in the previous paragraph scatters phonons in a particular frequency range while interacting weakly with all other frequency phonons, the combination of certain or all of these phonon scattering mechanisms will result in a large reduction in lattice thermal conductivity. Therefore, it is critical to benefit from all these mechanisms and affect phonon scattering in a broad frequency range without significantly affecting the electronic properties.

3.3 Sample Preparation Method

To study the physical properties of material that might be useful for thermoelectric application, one needs sufficiently large and homogenous samples. So, it is necessary to identify appropriate growth conditions that result in at least a millimeter-size single crystal or, if it is difficult to achieve, a homogenous polycrystalline specimen that can be used in its as-grown form or subjected to further processing [22]. Although the single crystals are always an advantage, they are not an absolute necessity. Since skutterudites have cubic structure, anisotropy is not a concern. The key to successful crystal growth is a complete understanding of the respective phase diagram that describes the thermodynamic equilibrium between various phases of the system. The phase diagram of one of the active skutterudites $CoSb_3$ is shown in Fig. 3.3.1 [23]. As shown in Fig. 3.3.1, three different stable phases are possible for skutterudites in a higher pnictogen region: metallic γ phase CoSb, semiconducting δ phase $CoSb_2$, and semiconducting ε phase $CoSb_3$, each forming peritectically. A peritectic reaction involves the formation of a homogenous compound or

solid solution from another solid phase and a liquid at a specific fixed temperature, called peritectic temperature T_p. In case of $CoSb_3$, the reaction can be described as:

$$\delta\text{-Phase} + \text{Liquid} \leftrightarrow \varepsilon\text{-phase at } T_p = 823\ ^{o}C$$

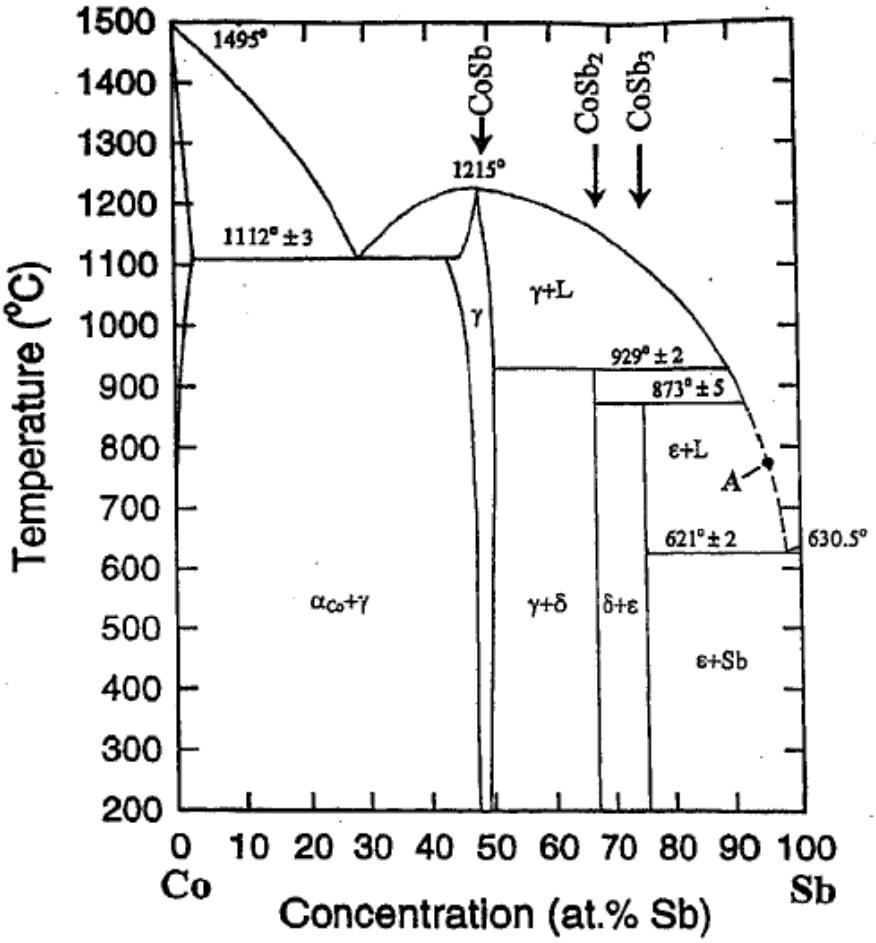

Fig. 3.3.1 Phase diagram of $CoSb_3$. Point *A* indicates a possible starting composition to grow a single crystal from melt (Ref. 23).

Because of very slow kinetics, growth rarely proceeds under such conditions that the peritectic reaction is fully complete. Keeping this fact in mind, there are several ways to prepare skutterudites samples of either a polycrystalline or single crystal nature [22].

1. Seal the stoichiometric amount of constituent elements in an evacuated quartz tube and heat the mixture at a temperature below the peritectic temperature for a week or two, followed by grinding and annealing.
2. Melt Co and Sb under argon environment and quench the melt. Annealing the ingot at 580-800 ^{o}C range gives a pure skutterudites phase.
3. There is a non-stoichiometric melt composition (such as represented by point A in Fig. 3.3.1) where the melt is richer in pnictogen isotherm with the liquids, but not as rich as the eutectic point near the pnicogen's end point. Cooling the melt will give $CoSb_3$.
4. Other techniques such as flux-assisted growth and chemical vapor transport method can be used to grow $CoSb_3$.

We are using a 3-step method to synthesize $CoSb_3$ based skutterudites: 1) Seal the stoichiometric amount of elements in a carbon coated quartz tube and melt them at 1100 ^{o}C for 24 hours and quench in water, 2) Put the cleaned ingot in a steel jar under an argon environment and ball mill it for certain period of time, and 3) Consolidate the nano-powder using a DC hot press.

3.3.1 Preparation of Powder for $CoSb_3$-based Skutterudites

As discussed in previous section the nano-powder of $CoSb_3$ based skutterudites was made by ball-milling the ingot using a high-energy ball mill (SPEX 8000M). The details of ingot preparation process is described below.

The stoichiometric amount of elements were loaded in a carbon coated quartz tube, pumped down to a low pressure of 2×10^{-6} mbar and sealed. The sealed quartz tubes were kept in a furnace and melted at a high temperature, usually 1050-1100 ^{o}C range for 24 hours and quenched in water to get the ingot. The ingot was then taken out of the tubes, cleaned using a steel brush and put in ultra-sonication in ethanol for further cleaning. The dried ingot was then loaded into a stainless steel jar with stainless steel balls in an argon protected glove box and ball milled for a certain time with an intermediate loosening of powder. The ingot is ball milled through a sequence of collision between grinding balls and ingot inside a high energy ball mill. Although the average temperature inside the ball-mill jar is normally less than 100 ^{o}C, the local temperature can be high enough close to alloying temperature. [19]. Although the ingots made by melting-quenching-annealing methods are pre-alloyed, the local high temperature further facilitates the alloying process due to the diffusion of the particles. However, there are some shortcomings of this method. After a long time ball-milling, the material might be amorphous. Although the size of the particles becomes really small, uniformity in the particle size is another issue. Fig. 3.3.2a, 3.3.2b, and 3.3.2c shows the pumping system, ball-mill jar, and ball-mill apparatus, respectively.

Fig. 3.3.2 a) Pumping system, b) Stainless steel jar and ball, and c) Ball-milling machine (SPEX 8000 M)

During the experiment, about 25 grams of Cobalt slugs (99.98%, Alfa Aesar), and Sb chunks (99.999%, Chengdu Chemphys Chemical Industry, China) and other filling or substitution elements are weighted stoichiometrically and loaded into a carbon-coated quartz tube. The ingot was made as described in the previous paragraph. The cleaned and dried ingot is then loaded in a stainless steel jar under argon protection and put in to the ball-milling machine and run for a certain amount of time. During the ball-milling process, the balls move back and forth and force to break the ingot into nano-powder. After a certain time of the ball-milling process, the powder sticks on the wall of the jar and makes a hard shell-like form, which makes the further ball-milling ineffective. Thus, we loose powder inside the glove box every 3 hours until we completely ball milled the ingot to the required time. Once the ball-milling process was over, the powder was used to make a sample disk.

3.3.2 Consolidation of Powder into Bulk Pellet

The next step after the ball-milling process was to consolidate the powder into a dense disk. The nano-powder was loaded into a graphite die inside the glove box and a DC hot press system was used to consolidate the powder into the disk. The schematic representation of the graphite die and hot press system is as shown in Fig. 3.3.3a and 3.3.3b, respectively.

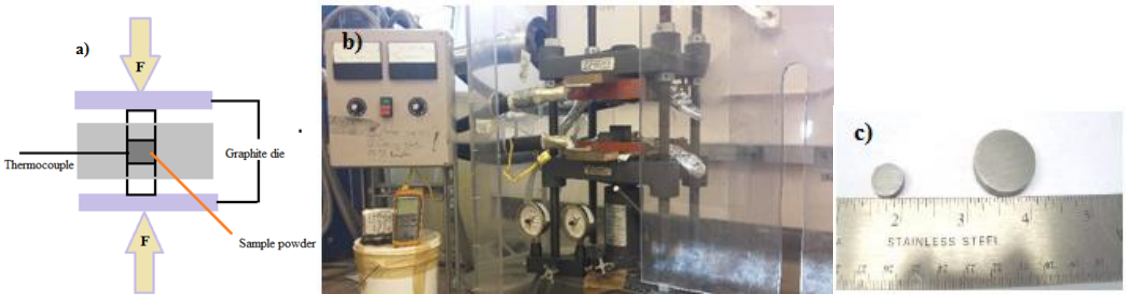

Fig. 3.3.3 a) Schematic picture of hot press, b) Lab-made hot press-system, and c) Consolidated sample disk of different size.

The graphite die is a hollow cylinder in which nano-powder is loaded almost at the center and then sealed with graphite rods on top and bottom. The loading is done inside the glove box. The whole set up was taken out and put on a carver press. A constant pressure of around 80 MPa was maintained to the powder. At the same time, the current was slowly increased with a ramping rate of 400 Amp per minutes until it was about 1000 Amp. The current then went through the plunger to the powder and produces heat via Joule's heating. In order to monitor the temperature, a thermocouple was inserted into a graphite die close to sample. When the temperature was close to the desired hot press temperature, the current was adjusted to achieve the required steady high temperature. In this hot press system, we

can achieve 750 ^{o}C in about 4 minutes. The cooling process is fast. It takes about 8 to 10 minutes for the sample to cool down to room temperature. During the disk preparation process, we wanted to preserve the small grain size to achieve a lower thermal conductivity. However, there is always grain growth during the hot press process. The fast cooling process in the DC hot press method might help reduce the grain growth. The sample that was ejected out from graphite die is as shown in Fig. 3.3.3c. It is cut into nearly equal sized disk. One of them was polished to get a uniform thickness disk for thermal diffusivity measurement while the other was cut into a 2×2×12 mm^3 bar for the measurement of electrical resistivity and the Seebeck coefficient measurement.

X-ray diffraction was done on the pellet after the hot press to examine the phase formation. As shown in Fig. 3.3.4. The peaks can be well indexed, indicating that the sample forms pure skutterudites phase.

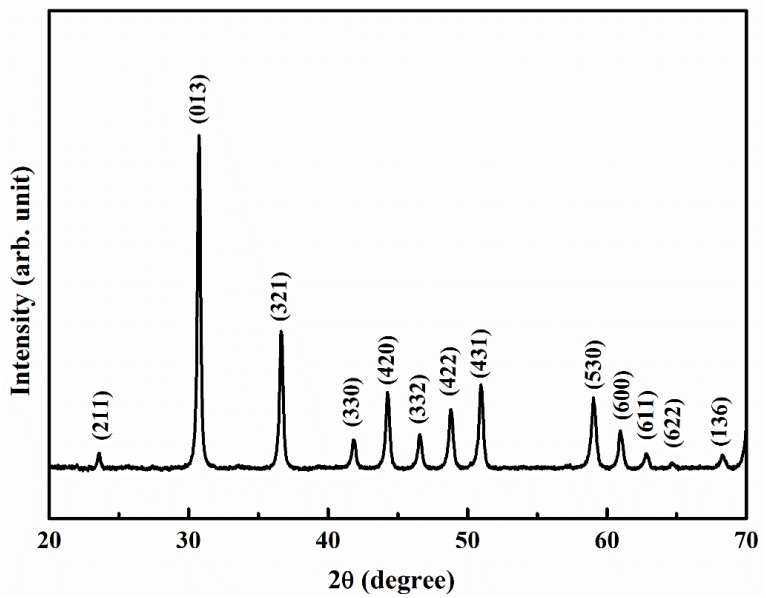

Fig. 3.3.4 XRD analysis of consolidated sample.

3.4 $Yb_xCo_4Sb_{12}$ Samples: Results and Discussion

As mentioned earlier, skutterudites has two voids per unit cell, intrinsic of its crystal structure. The void can be filled with foreign atoms which act as phonon rattlers. The fillers atoms are loosely bound with a Sb-planner ring. When the frequency of vibration of the rattler is comparable to the soft-mode vibration, it strongly scatters phonon and drastically reduces the thermal conductivity without degrading the electrical properties significantly [23, 24]. Heavy but small elements give a significant reduction in thermal conductivity. Yb is one of the ideal rattling species [24, 25, 26]. Nolas *et al*., reported a peak *ZT* of about 1 at about 600 K in $Yb_{0.19}Co_4Sb_{12}$ [25], Geng *et al*., reported a peak *ZT* of about 0.7 at 673 K in $Yb_{0.15}Co_4Sb_{12}$ [26], and Yang *et al*., reported a peak *ZT* of 1.2 at about 823 K in nanostructured $Yb_{0.35}Co_4Sb_{12}$ made by ball-milling elements of Yb, Co, and Sb and hot pressing the ball milled nano-powders [28]. In literature, the solubility of Yb was reported to be 0.19, the so-called solubility limit, in samples made by melting and slow cooling [20]. Li *et al*. reported the bulk solubility of Yb to be 0.3 in the samples made by melting and fast spin-cooling method with a higher *ZT* of 1.3 [27], and Yang *et al*. achieved even higher solubility of 0.35 by creating nanostructured skutterudites using ball-milling and hot pressing to achieve a peak ZT of 1.2 [28]. This indicates that the issue on the solubility limit of Yb in filled skutterudites is not completely settled down and clearly depends on the sample preparation method. Therefore, it may still be possible to enhance the solubility of Yb in the voids if an appropriate preparation method can be found. Here, we report our success on increasing the bulk solubility of Yb in $Yb_xCo_4Sb_{12}$ (x = 0.2, 0.35, 0.45, and 0.5) by first making an alloy ingot, which resulted in a higher peak *ZT*. The result of this work

is compared with the previously reported value obtained on samples made by hot pressing ball-milled powder from elements [28].

The structures of the samples were characterized by X-ray diffraction (X'pert PRO PANalytical diffractometer with Cu Kα radiation source), scanning electron microscopy (SEM, LEO 1500), and transmission electron microscopy (TEM, JEOL 2100F).

The XRD spectra of the hot pressed samples [Fig. 3.4.1] show the single skutterudites phase even for x = 0.5, which means that the Yb solubility can be as high as 0.5. However, we observed some extra peaks for x = 0.6, indicating the existence of impurity phases, which means the solubility of Yb in skutterudite is about 0.5 by this method.

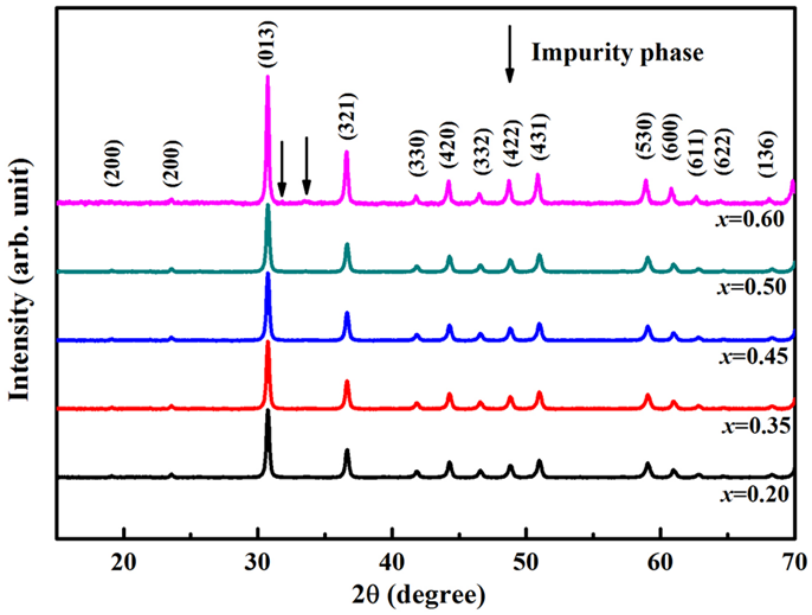

Fig. 3.4.1 XRD patterns of dc hot pressed skutterudites $Yb_xCo_4Sb_{12}$ samples with x = 0.2, 0.35, 0.45, 0.5, and 0.6. All samples except for x = 0.6 show pure skutterudites phase without impurity phases.

Fig. 3.4.2a and Fig. 3.4.2b show the low and high magnification SEM images of the hot pressed sample, respectively. Fig. 3.4.2c and Fig. 3.4.2d are the TEM images of the hot pressed sample which show the grain size and crystallinity, respectively. The grain size is widely distributed. Most of the grains are a few hundred nanometers (100 – 500 nm) with some grains as big as 1 μm, but the percentage of such big grains are low, which is very different from the more uniform grain-size distribution in the previous report [28]. The bigger grains may be due to higher hot press temperature of 750 ^{0}C. The wide distribution of grain size may help scatter phonons with different phonon mean free paths [29, 30]. The SEM image shows that the crystallized grains are closely packed, indicating a high volume mass density. This observation is consistent with the measured Archimedean volumetric mass density of 7.65 g cm^{-3} for x = 0.35, close to full theoretical density of 7.80 g cm^{-3}.

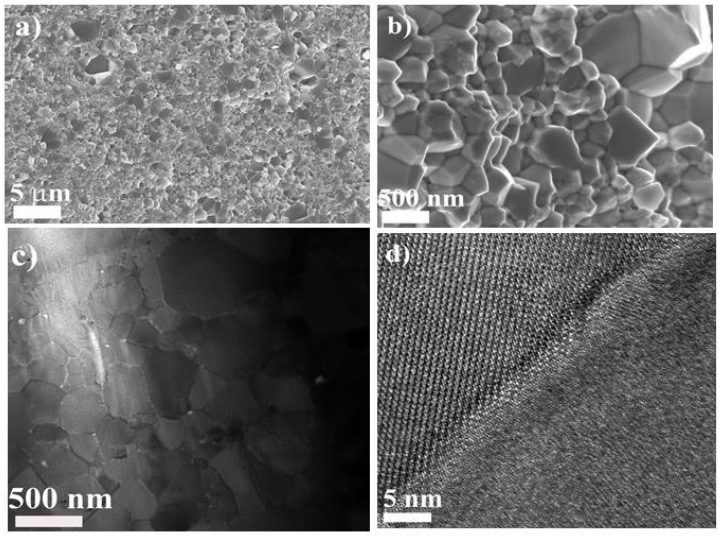

Fig. 3.4.2 SEM images at (a) low and (b) high magnification and TEM image at low (c) and high (d) magnification of $Yb_{0.35}Co_4Sb_{12}$ samples, showing the grain sizes, crystallinity, and clean grain boundary.

The temperature-dependent specific heat capacity (*Cp*) of $Yb_xCo_4Sb_{12}$ (x = 0.2, 0.35, 0.45, and 0.5) is shown in Fig. 3.4.3. The specific heat capacity of all samples increases with temperature. The *Cp* value of the sample with higher Yb concentration is lower.

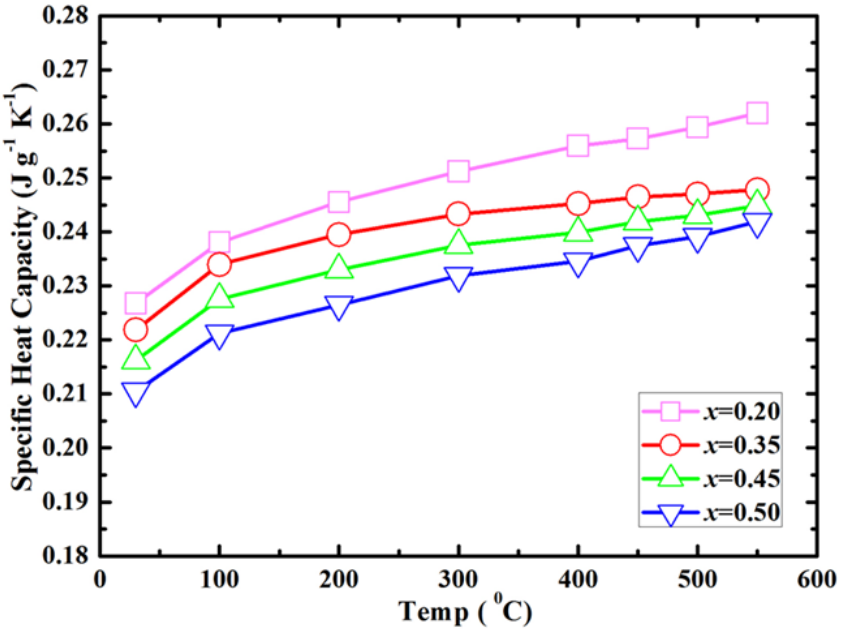

Fig. 3.4.3 Temperature-dependent specific heat capacity of $Yb_xCo_4Sb_{12}$ (x = 0.2, 0.35, 0.45, and 0.5). The specific heat capacity increases with temperature.

The temperature-dependent thermoelectric properties are shown in Fig. 3.4.4. The data from reference 28 are included for comparison [28]. In the previous work, the author had mentioned about the difficulty to get a sample disk with x = 0.2 [28]. We overcame the difficulty and made the sample with x = 0.2. Fig. 3.4.4a shows the temperature-dependent electrical conductivity of all the $Yb_xCo_4Sb_{12}$ (x = 0.2, 0.35, 0.45, and 0. 5) samples. In this

work, we do not show the results for $x = 0.6$ owing to its poor thermoelectric properties. From Fig. 4(a), we have the following observations: a) the electrical conductivity of samples increases with increasing Yb concentration because more electrons are donated to the system by Yb, b) the electrical conductivity of all samples decreases with increasing temperature showing a heavily doped semi-conductor nature, and c) the electrical conductivity of sample $Yb_{0.35}Co_4Sb_{12}$ made in the present work is higher than that with the same composition reported previously [28]. The higher electrical conductivity of the sample made in the present work may come from the different sample preparation method. In this work we pre-alloyed the elements by making ingot before ball milling. Compared with directly ball milling the pure elements, pre-alloying may have reduced defects in the final sample.

Fig. 3.4.4b shows the temperature-dependent Seebeck coefficient. The negative Seebeck coefficient indicates that electrons are the dominant charge carriers. The absolute value of the Seebeck coefficient increases with temperature. The Seebeck coefficient measured in the present work is lower than the previously reported data for the same composition.

The temperature-dependent power factor (*PF*) is plotted in Fig. 3.4.4c. The PF of all samples increases with temperature. A maximum power factor of ~53 $\mu W\ cm^{-1}\ K^{-2}$ at 550 ^0C was obtained for the $Yb_{0.35}Co_4Sb_{12}$ sample in the present work, which is higher than the maximum power factor of the previously reported value ~48 $\mu W\ cm^{-1}\ K^{-2}$ [28]. The higher power factor is achieved mainly due to the higher electrical conductivity.

The temperature-dependent thermal conductivity is shown in Fig. 3.4.4d. For the samples with $x = 0.2$, the thermal conductivity first decreases with increasing temperature, attains a

minimum value at 300 ^{0}C and then increases with temperature. But, for the samples with x = 0.35, 0.45, and 0. 5, the thermal conductivity keeps rising all the way from room temperature to 550 ^{0}C. The thermal conductivity of $Yb_{0.35}Co_4Sb_{12}$ is the lowest in the entire temperature range and varies from 2.8 W m^{-1} K^{-1} at room temperature to 3.2 W m^{-1} K^{-1} at 550 ^{0}C.

To better understand the phonon scattering, we have calculated the lattice thermal conductivity by subtracting the electronic contribution from the total thermal conductivity. The electronic contribution to total the thermal conductivity is calculated using Wiedemann-Franz relation ($\kappa_e = \sigma LT$, where σ is the electrical conductivity, L is the Lorenz number, and T is the absolute temperature). In the previous work [28], the carrier part of thermal conductivity was calculated using a constant Lorenz number 2×10^{-8} W Ω K^{-2}. In this paper, we assumed that the acoustic phonon scattering is dominant for carrier scattering and evaluated the temperature-dependent Lorenz number from the reduced Fermi energy deduced from the Seebeck coefficient at room temperature based on single parabolic band model [31]. We also calculated the lattice part of thermal conductivity for the sample reported previously in the same way. Fig. 3.4.4e shows the temperature-dependent lattice thermal conductivity. The lattice contribution to total thermal conductivity for the sample with x = 0.35 prepared in the present work is lower than the sample previously reported. It varies from 1.5 W m^{-1} K^{-1} at room temperature to ~1.1 W m^{-1} K^{-1} at 550 ^{0}C. Such a lower lattice thermal conductivity may be due to stronger phonon scattering off the different grain sizes [30].

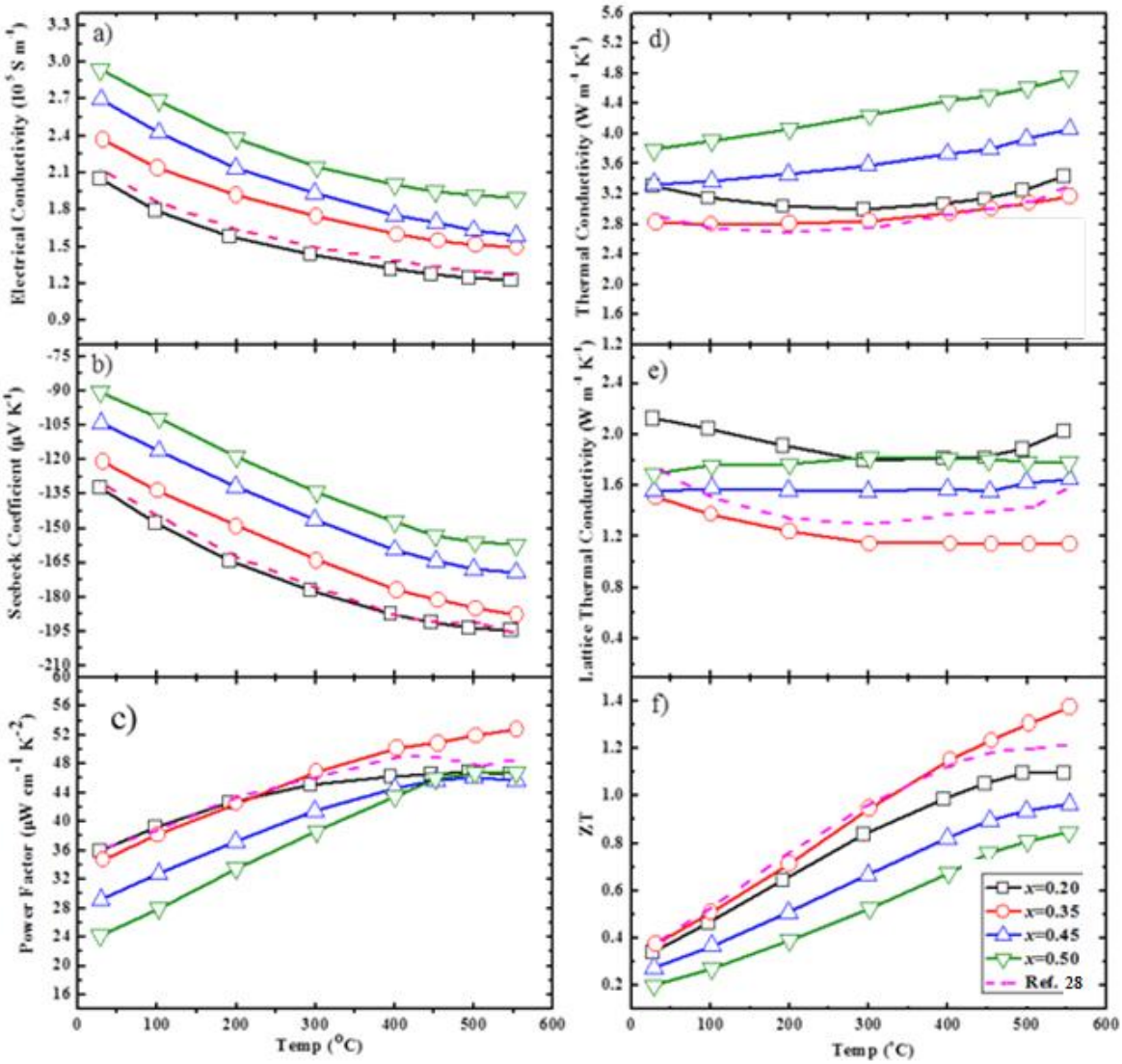

Fig. 3.4.4 Temperature-dependent thermoelectric properties of $Yb_xCo_4Sb_{12}$ (x = 0.2, 0.35, 0.45, and 0. 5) samples: (a) electrical conductivity, (b) Seebeck coefficient, (c) power factor, (d) thermal conductivity, (e) lattice thermal conductivity, and (f) figure-of-merit, *ZT*.

The temperature-dependent *ZT* from room temperature to 550 ^{0}C is shown in Fig. 3.4.4f. The highest *ZT* is of ~1.4 for the sample with $x = 0.35$ at 550 ^{0}C. This peak *ZT* is higher than the peak *ZT* of 1.2 at about the same temperature reported previously [28]. It is also comparable to most of the double-filled [32-34] and close to the triple-filled skutterudites [35, 36]. The improvement in peak *ZT* mainly comes from the improved power factor due to increased electrical conductivity and slightly lowered thermal conductivity because of the wider distribution of the grain sizes resulted from a different sample preparation method.

3.5 Elemental Substitution Method

Most of the works to improve thermoelectric performance of *n*-type skutterudites are based on tuning the electrical and the thermal transport properties void-filling methods. However, both the electrical and thermal transport properties in skutterudites can be tuned by bringing a distortion in Sb-planner ring via elemental substitution method [37].

As discussed earlier, the skutterudites structure consist of Sb-planner rings mutually perpendicular to each other. If we remove one Sb from the planner ring by an element left to it such as Sn or Ge, then the ring becomes positively charged center. So, it is possible to replace Sb from the ring by an element right to Sb such as Se or Te. The schematic representation of such method is shown in Fig. 3.5.1.

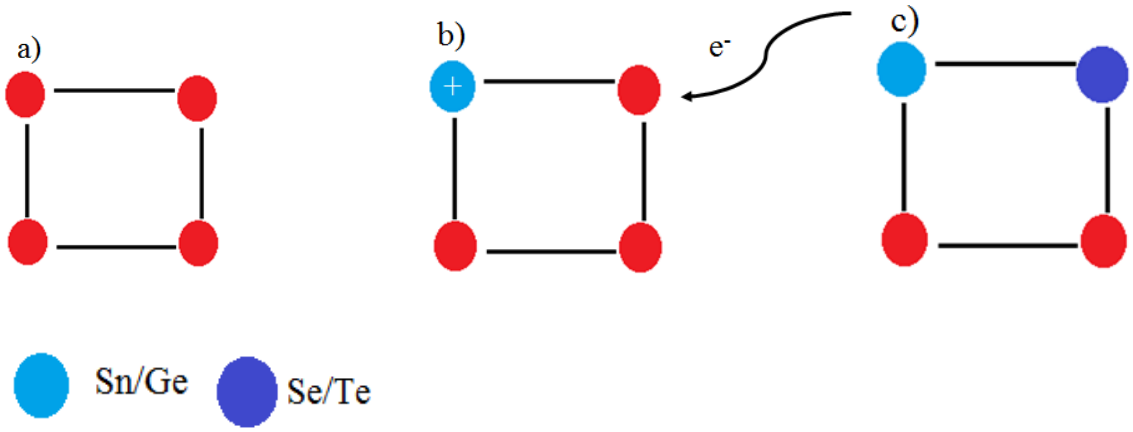

Fig. 3.5.1 Schematic representation of elemental substitution method.

Since the elements are connected to each other by a spring, the vibrational frequency along Sn or Ge/Sb will be different than Se or Te/Sb. This vibrational frequency will be different than Sn or Ge/Se or Te vibration and Sb/Sb vibration, giving a wide range of vibrational frequencies. Thus, elemental substitution method on the Sb-planner ring has also been proven to be an effective way to reduce the lattice thermal conductivity by significantly scattering phonons via mass fluctuation.

3.6 $CoSb_{2.8}Sb_xTe_{0.2-x}$ Samples: Result, and Discussion

The thermoelectric performance of *n*-type skutterudites is mostly improved by tuning the electrical transport properties and the thermal transport properties by void-filling methods. Besides filling the voids by foreign atoms, one can tune both thermal and electrical properties of skutterudites by elemental substitution [38, 39]. There have been many reports on improvements on thermoelectric properties of skutterudites by elemental substitution. A peak *ZT* of ~0.9 at 530 ^{o}C was reported for $CoSb_{11.4}Te_{0.6}$ made by a solid-state reaction method followed by a spark plasma sintering [39], and a peak *ZT* of ~1 at

530 ^{o}C in $CoSb_{2.625}Ge_{0.125}Te_{0.25}$ by melt-quench-annealing followed by spark plasma sintering [41].

To demonstrate the effect of elemental substitution in pnictogen rings to improve the thermoelectric performance, we here studied skutterudites compounds of compositions $CoSb_{2.8}Sn_xTe_{0.2-x}$ with x = 0.005, 0.01, and 0.03 by the melting-quenching-annealing method followed by ball-milling and hot pressing. The ingot was annealed at 600 ^{o}C for 7 days and ball milled for 5 hours. The nano-powder was then hot pressed at 560 ^{o}C for 5 minutes to a sample disk. Thermoelectric property investigation revealed that a small amount of Sn is good enough to suppress the transport of heat-carrying phonons, lowering the total thermal conductivity. The incorporation of Sn in Sb site enhanced the solubility of Te, which improves the power factor to a moderate value. The best *ZT* value of ~1.1 was achieved at 530 ^{o}C in $CoSb_{2.8}Sn_{0.005}Te_{0.195}$.

The crystallographic phase of the samples was characterized by X-ray powder diffraction (X'pert PRO PANalytical diffractometer with Cu Kα radiation source), and the microstructure of the samples was studied by scanning electron microscopy (SEM, LEO 1500) and transmission electron microscopy (TEM, JEOL 2100F).

Fig. 3.6.1 shows the XRD patterns of three compositions studied. The compositions with x = 0.005 and 0.01 show the presence of more minor secondary phase than the composition with x = 0.03. The minor phases are probably $CoSb_2$ and/or $CoTe_2$.

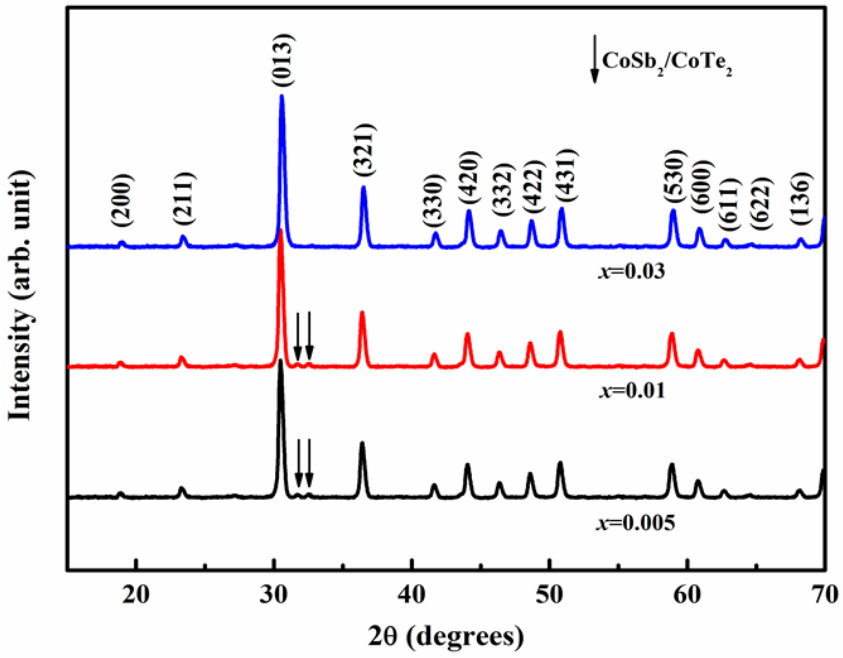

Fig. 3.6.1 XRD patterns of DC hot pressed skutterudites samples $CoSb_{2.8}Sn_xTe_{0.2-x}$ with x = 0.005, 0.01, and 0.03. Sample with x=0.005 and 0.01 show minority phase(s).

Fig. 3.6.2 shows the lattice parameter, a, as a function of Sn content, x. The lattice parameter decreases with increasing Sn content, an indication of lattice contraction, which is due to the smaller ionic radii of Sn compared with Te.

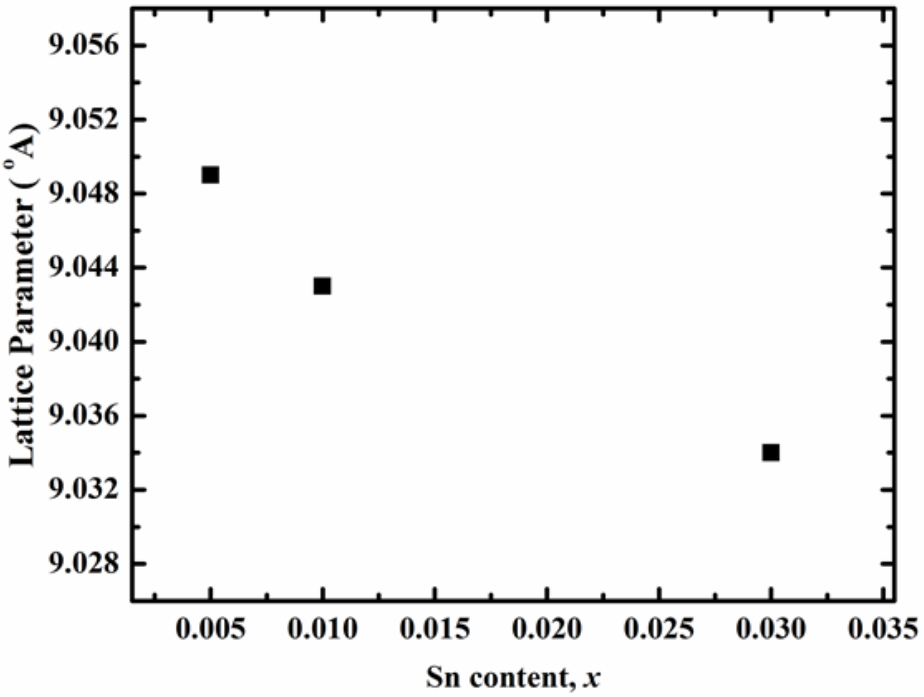

Fig. 3.6.2 Lattice parameter of $CoSb_{2.8}Sn_xTe_{0.2-x}$ samples as a function of Sn content, *x*. The lattice parameter decreases with increasing Sn concentration.

Fig. 3.6.3 shows the SEM images at low (Fig. 3.6.3a) and high (Fig. 3.6.3b) magnifications of freshly broken surface of the hot pressed samples. Fig. 3.6.3c and Fig. 3.6.3d show the TEM images of the hot pressed sample at low and high magnifications, respectively. From the SEM images, we observed that the most grains are about 200-300 nm in size with some big ones about 500 nm, which is further confirmed by the TEM image as shown in Fig. 3.6.3c. The grains with a wide size distribution may help scatter phonons with different phonon mean free paths [29, 30]. The SEM images show that the crystallized grains are closed packed, an indication of high volume mass density. The high magnification TEM

image shown in Fig. 3.6.3d shows that the grain boundaries are clean and the orientations are of large angles, which may also scatter more phonons.

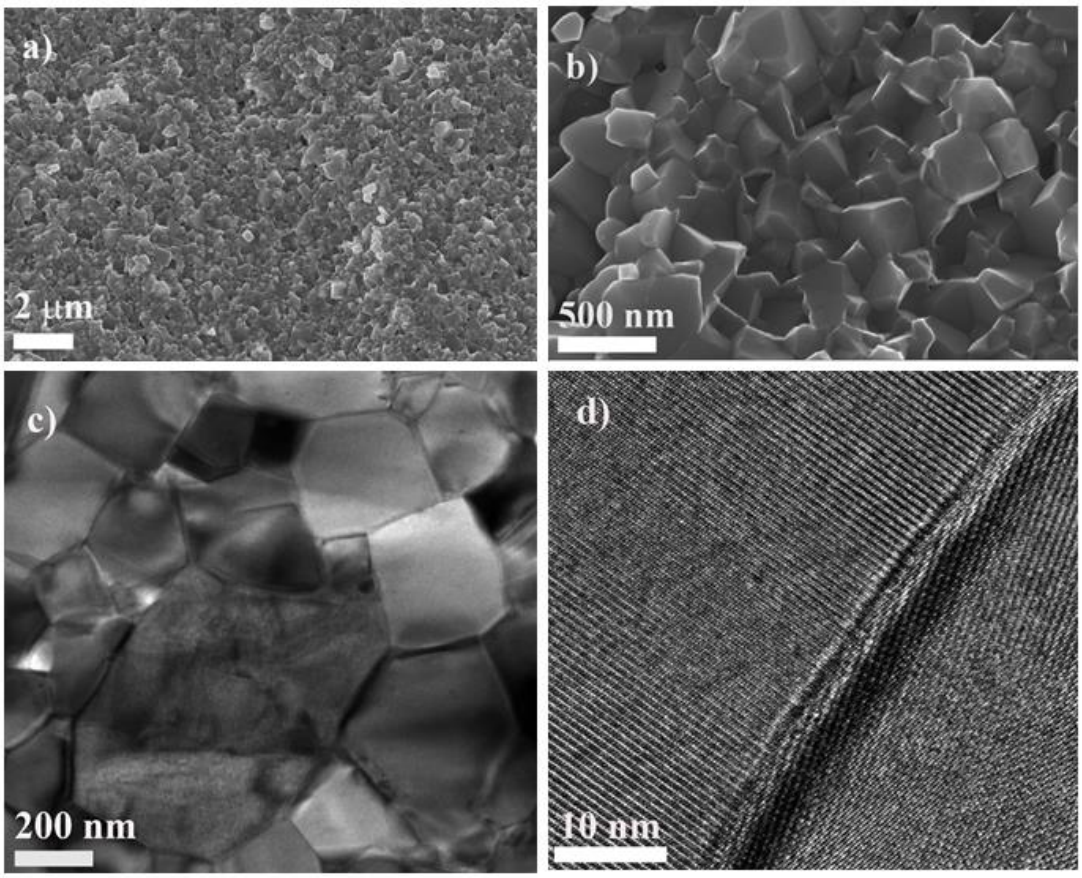

Fig. 3.6.3 SEM images at (a) low and (b) high magnification and TEM image at low (c) and high (d) magnification of sample $CoSb_{2.8}Sn_{0.005}Te_{0.195}$, showing the grain size, crystallinity, and clean grain boundary with large angle.

Fig. 3.6.4 shows the carrier concentration at room temperature as a function of Sn content, *x*. The carrier concentration of all samples is in the order of 10^{20} cm^{-3}, and decreases with

increasing Sn concentration. Since Sn is in the left of Sb in periodic table, the lower carrier concentration with higher Sn is because that Sn acts as electron acceptor instead of donor.

The electrical conductivity of the samples as a function of temperature is plotted in Fig. 3.6.5a. From the plot, we observed: a) the electrical conductivity of the Sn/Te doped skutterudites decreases with increasing Sn content, which is due to decreased carrier concentration as shown in Fig. 3.6.4; and b) the electrical conductivity of all samples decreases with temperature up to about 450 ^{o}C and then increases. The increased electrical conductivity at high temperature is the result of the sum of contributions from both the electrons and holes.

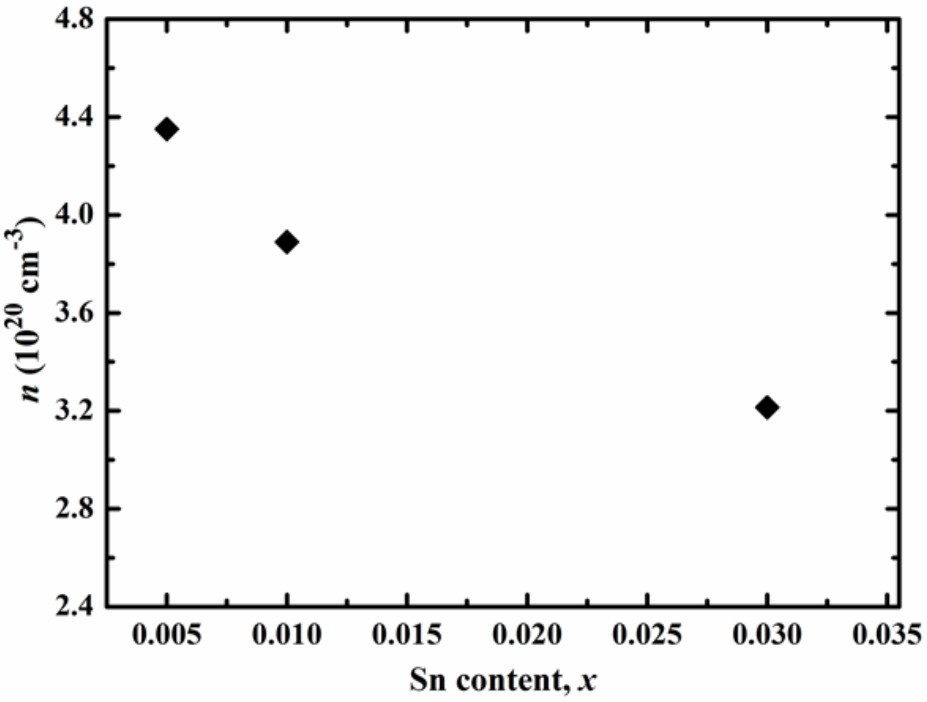

Fig. 3.6.4 Carrier concentration of $CoSb_{2.8}Sn_xTe_{0.2-x}$ samples as a function of Sn content, *x*. Carrier concentration decreases with increasing Sn concentration.

The temperature-dependent Seebeck coefficient is shown in Fig. 3.6.5b. The Seebeck coefficient of all samples is negative, implying that the dominant charge carriers are electrons. The absolute value of Seebeck coefficient of all samples increases up to about 450 ^{o}C. Above this temperature, the Seebeck coefficient of all samples decreases, a signature of bipolar effect. The upturn in Seebeck coefficient for $CoSb_{2.8}Sn_{0.03}Te_{0.17}$ above 450 ^{o}C is faster than the other two samples, implying that higher Sn content produces stronger bipolar effect at elevated temperatures. The Seebeck coefficient of such a doped semi-conductor can be expressed as [2],

$$S = \frac{S_e \sigma_e + S_h \sigma_h}{\sigma_e + \sigma_h} \ldots\ldots\ldots\ldots\ldots\ldots\ldots (3)$$

where σ_e and σ_h are the conductivities from electrons and holes respectively, S_e and S_h are the Seebeck coefficients from electrons and hole, respectively. At higher temperatures, both the electrons and holes move across the band gap, resulting in decreased Seebeck coefficients owing to the opposite effect of two types of carriers. From the temperature-dependent Seebeck coefficient measurement, the band gap (E_g) of various samples can be roughly estimated using the equation $E_g = 2eS_{max}T_{max}$, where e is the elementary charge, S_{max} is the peak Seebeck coefficient, and T_{max} is the temperature corresponding to the maximum Seebeck coefficient [42]. Based on this equation, the band gaps of the samples were estimated to be in the range of 0.30-0.33 eV, consistent with the literature value [43].

The temperature-dependent power factor is as shown in Fig. 3.6.5c. The power factor of all samples increases with temperature in the entire range except for $CoSb_{2.8}Sn_{0.03}Te_{0.17}$. A

maximum power factor ~42 μW cm^{-1} K^{-2} is achieved for $CoSb_{2.8}Sn_{0.005}Te_{0.195}$ at 530 ^{o}C. This power factor is higher than the reported one (25-36 μW cm^{-1} K^{-2}) [44, 45].

The temperature-dependent total thermal conductivity of all samples is plotted in Fig. 3.6.5d. The thermal conductivity decreases with decreasing Sn content. The reduction is due to the perturbation in thermal transport caused by Sn and Te in Sb planner rings [12]. The thermal conductivity of the samples with x = 0.005, and 0.01 is almost flat up to about 400 ^{o}C. Above this temperature, the thermal conductivity increases due to bipolar effect. But, for the sample with x = 0.03, the total thermal conductivity decreases with temperature up to about 400 ^{o}C and then increases also due to bipolar effect. The total thermal conductivity is the sum of the electronic thermal conductivity (κ_e) and lattice thermal conductivity (κ_l). The electronic part of thermal conductivity can be calculated using Wiedemann-Franz law: $\kappa_e = \sigma L T$, where σ is the electrical conductivity, L is the Lorenz number, and T is the absolute temperature. The Lorenz number can be calculated as [46],

$$L = \left(\frac{\kappa_B}{e}\right)^2 \left[\frac{\left(r+\frac{7}{2}\right)F_{r+\frac{5}{2}}(\xi)}{\left(r+\frac{3}{2}\right)F_{r+\frac{1}{2}}(\xi)} - \left(\frac{\left(r+\frac{5}{2}\right)F_{r+\frac{3}{2}}(\xi)}{\left(r+\frac{3}{2}\right)F_{r+\frac{1}{2}}(\xi)}\right)^2\right] \ldots\ldots\ldots\ldots\ldots\ldots (4)$$

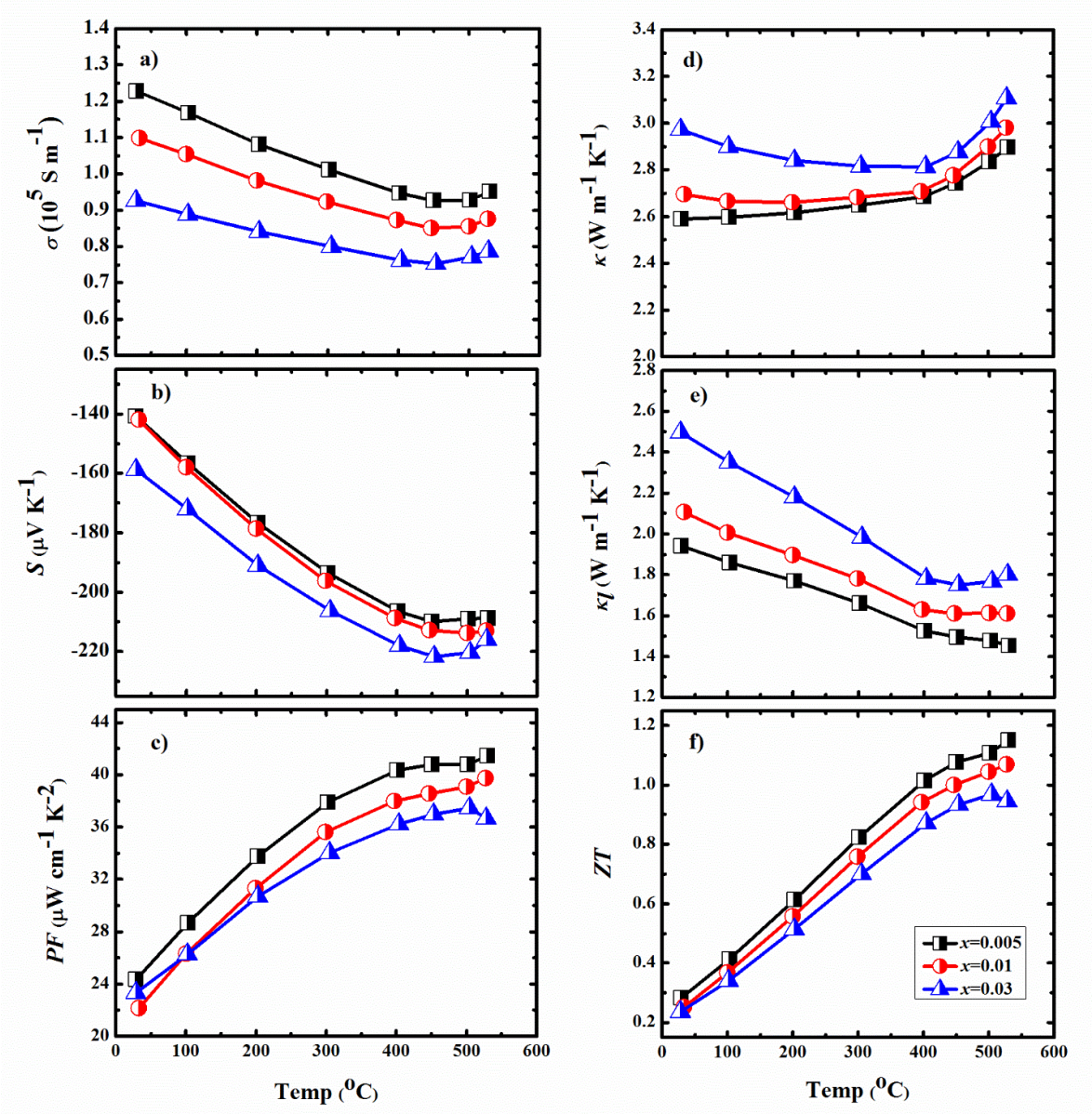

Fig. 3.6.5 Temperature-dependent thermoelectric properties of $CoSb_{2.8}Sn_xTe_{0.2-x}$ samples (x = 0.005, 0.01, and 0.03): (a) electrical conductivity, (b) Seebeck coefficient, (c) power factor, (d) thermal conductivity, (e) lattice thermal conductivity, and (f) figure-of-merit, *ZT*.

where r is the scattering parameter, κ_B is the Boltzmann's constant, e is the electronic charge, $F_n(\xi)$ is the Fermi integral given by

$$F_n(\xi) = \int_0^\infty \frac{x^n}{1 + e^{x-\xi}} dx \ldots\ldots\ldots\ldots\ldots\ldots\ldots\ldots (5)$$

where ξ is the reduced Fermi energy that can be calculated from the Seebeck coefficient S as well as the scattering parameter r, given as

$$S = \pm\frac{\kappa_B}{e}\frac{\left(r + \frac{5}{2}\right)F_{r+\frac{3}{2}}(\xi)}{\left(r + \frac{3}{2}\right)F_{r+\frac{1}{2}}(\xi)} - \xi \ldots\ldots\ldots\ldots\ldots\ldots\ldots (6)$$

In our calculation, the Lorenz number is evaluated from the reduced Fermi energy based on the Seebeck coefficient at room temperature and two-band model with a temperature-dependent band gap of E_g = *0.45-0.0004 T* eV for $CoSb_3$, where T is the absolute temperature [31, 45]. The lattice thermal conductivity is then obtained by subtracting the electronic contribution from the total thermal conductivity. The temperature-dependent lattice thermal conductivity is shown in Fig. 3.5.6e. The sample with x = 0.005 has the lowest lattice thermal conductivity in the entire temperature range. The substitution of Sn and Te in Sb planner rings yields stronger scattering of phonons by mass-fluctuation because of the mass difference of Sn, Te, and Sb atoms. The scattering strength of such a system can be written in the form of

$$A = \frac{\Omega_0}{4\pi v^2} x(1-x)\left(\frac{\Delta M}{M}\right)^2 \ldots\ldots\ldots\ldots\ldots\ldots\ldots (7)$$

where, Ω_0, υ, x, ΔM, and M represent the volume of unit cell, the velocity of sound, the fraction of guest atoms, the atomic mass difference between the guest and host, and the average mass of the cell, respectively [47, 48]. According to this equation, the lattice thermal conductivity should decreases with increasing Te content due to an increase in point defect, consistent with the experimental observation. The lattice thermal conductivity for $CoSb_{2.8}Sn_{0.005}Te_{0.195}$ varies from ~1.85 W m^{-1} K^{-1} at room temperature to ~ 1.4 W m^{-1} K^{-1} at 530 ^oC, comparable to lattice thermal conductivity of multiple filled skutterudites [35].

The temperature-dependent dimensionless figure-of-merit *ZT* of various samples was calculated from the measured electrical conductivity (σ), Seebeck coefficient (S), and thermal conductivity κ and is plotted in Fig. 3.6.5f. The *ZT* value increases with increasing Te content. The highest *ZT* ~1.1 is achieved at about 530 ^oC in $CoSb_{2.8}Sn_{0.005}Te_{0.195}$. This *ZT* value is competitive with some of the single filled *n*-type skutterudites [25, 28, 43].

3.7 Summary

In summary, we have synthesized *n*-type skutterudites samples by two different methods: by filling the intrinsic voids and by elemental substitution method. The Yb-filled skutterudites samples are made by general melting-quenching-ball-milling, and DC hot pressing the nano-powder in a graphite die at 750 ^oC under a pressure of 80 MPa for 7 minutes. XRD spectrum of $Yb_xCo_4Sb_{12}$ (x = 0.2, 0.35, 0.45, 0.5, and 0.6) shows that solubility of Yb can be enhanced by the melting method. We observed increased electrical conductivity with Yb concentration, which not only enhances the power factor but also

reduces the thermal conductivity significantly due to strong rattling effect. Comparing previously reported result, the higher power factor of $Yb_{0.35}Co_4Sb_{12}$ in the present sample could be due to better solubility of Yb in the host system. It could be also due to the presence of fewer defects due to pre-alloying the elements by melting method. The smaller lattice thermal conductivity of the best sample we have synthesized may be due to a broad range of phonon scattering from widely distributed grains.

By substituting Sn and Te for Sb, we have synthesized *n*-type skutterudites of the form $CoSb_{2.8}Sn_xTe_{0.2-x}$ by melting-quenching-annealing-ball-milling, and DC hot-pressing the nano-powder at 560 ^oC at 80 MPa for 5 minutes. XRD spectra shows the presence of secondary phases with small Sn concentration. However, the strength of such minority phases decreases with increasing Sn concentration. The decreased electrical conductivity of sample with increasing Sn is due to the decreased carrier concentration. However, we observed that small amount of Sn is good enough to bring the perturbation in Sb planner ring, suppressing the lattice thermal conductivity significantly. With a moderate high power factor and low thermal conductivity, we achieved a peak *ZT* above 1.1 at 500 ^oC in $CoSb_{2.8}Sn_{0.005}Te_{0.195}$.

3.8 References

1. Dresselhaus et al., *Adv. Mater*. **2007**, 19, 1.
2. Nolas, G. S., Sharp, J., and Goldsmith, H. J. *Thermoelectrics: Basic Principles and New Materials Developments* **2001**, Springer, New York.
3. Pei *et al., Appl. Phys. Lett.* **2006**, 89, 221107.
4. Shi *et al., Appl. Phys. Lett*. **2008**, 92, 182101.
5. Shi *et al., J. Am. Chem. Soc*. **2011**, 133, 7837.
6. Liu et al., *J. Appl. Phys.* **2007**, 102, 103717.
7. Dahal *et al., JOM* **2014**, 66, 2282.
8. Sales *et al., Phys. Rev. B* **1997**, 56, 15081.
9. Schnelle *et al., Phys. Rev. B* **2008**, 77, 094421.
10. Sales *et. al*., Science **1996**, 272, 1325.
11. Singh *et. al.,* Mater. Res. Soc. Sym. Proc. **1999**, 545, 3.
12. Keppens *et al., Nature* **1998**, 395, 876.
13. Singh *et al., Phys. Rev. B* **1994**, 50, 111235.
14. Nolas *et al., Annu. Rev. Mater. Sci*. **1999,** 29, 89.
15. Caillat *et al., J. Appl. Phys.* **1996**, 80, 4442.
16. Jung *et al., Inorg. Chem*. **1990**, 29, 2252.
17. Harima et al., *J. Magn. Magn. Mater*. **1998**, 117, 321.
18. Caillat *et. al., J. Appl. Phys*. **1996,** 80, 4442.
19. Rowe D. M. (Ed), *CRC Handbook of Thermoelectrics, Micro to Nano*, **2006,** CRC Press, Boca Raton, FL.

20. Uher C., *In Semi-conductors and Semimetals, Ed Tritt T. M.*, Academic Press, New York, (**2001**), 69, pp 139-253.
21. Nolas *et. al., Phys. Rev. B* **1998**, 58, 164.
22. Feshoctte *et. al., J. Less-common Metals* **1989**, 155, 255.
23. Fleurial et al., Proceeding of 15th International Conference of Thermoelectrics (Unpublished) **1996**, p91.
24. Sales *et al., Phys. Rev*. B **2000**, 61, 2475.
25. Nolas *et.al, Appl. Phys. Lett*. **2000,** 77, 1855.
26. Geng *et.al, Appl. Phys. Lett*. **2007**, 91, 022106.
27. Li *et. al., Appl. Phys. Lett.* **2009**, 93, 252109.
28. Yang *et.al, Phys. Rev. B* **2009**, 80, 115329.
29. Poudel *et. al., Science* **2008**, 320, 634.
30. Biswas *et. al., Nature* **2012**, 489, 414.
31. Liu *et. al., Adv. Eng. Mater*. **2011**, 1, 577.
32. Peng *et. al., J. Appl. Phys*. **2009**, 105, 084907.
33. Salvador *et. al., J. Appl. Phys*. **2010**, 107, 043705.
34. Li *et. al., Appl. Phys. Lett*. **2009**, 94, 102114.
35. Liu *et al., Chem. Mater.* **2008**, 20, 7529.
36. Graff et. al., *J. Elec. Mater.* **2011**, 40, 696.
37. Ballikaya et. al., *J. Elec. Mater.* **2011**, 40, 571.
38. Dimitrov *et. al., Phys. Rev. B* **2010**, 82, 174301.
39. Liu *et. al., Chem. Mater*. **2008**, 20, 7526.
40. Duan *et. al., J. Mater. Sci: Mater. Electron* **2012**, 23, 1822.

41. Su *te al., J. Elec. Mater*. **2011**, 40, 1286.

42. Goldsmith *et. al., J. Elec. Mater*. **1999**, 28, 869.

43. Mandrus *et. al., Phy. Rev. B* **1995**, 52, 4926.

44. Li *et. al., J. Appl. Phys*. **2005**, 98, 083702.

45. Liu *et. al., J. Appl. Phys*. **2007**, 102, 103717.

46. Rowe, D. M., Bhandari, C. M., *Modern Thermoelectrics,* Reston Publishing, Reston, VA **1983**.

47. Meisner *et. al., Phys. Rev. Lett.* **1998**, 80, 3551.

48. Yang *et. al., Phys. Rev. B* **2000**, 63, 0114410.

Chapter 4

Optimization of $CoSb_3$-based Skutterudites and Their Thermoelectric Properties

4.1 Introduction

The thermoelectric properties of TE materials widely depends on the sample synthesis process. The ball-milling time, hot press temperature, hot pressing holding time, and pressure during hot pressing are different parameters that affects the TE properties of the system. This chapter will discuss the detailed experimental data of Yb-filled $Yb_{0.35}Co_4Sb_{12}$ made under different conditions to achieve a high figure-of-merit, *ZT*.

4.2 Optimization of Ball Milling Time

The ball-milling time determines the grain size of the particle which plays an important role on determining the electrical and thermal properties. For short ball-milling times, the grains are bigger. So, electrons and phonons do not suffer significant scattering, giving higher values of electrical and thermal conductivity. A longer ball-milling time makes the grain size very small, which significantly scatters both electrons and phonons and lowers both the electrical and thermal conductivity. However, even longer ball-milling times may introduce some defects which may deteriorate the electrical conductivity significantly. So, optimization of ball-milling time is required to tune the thermoelectric properties of the sample to achieve higher *ZT* values. The details of the experimental findings with a different ball-milling times is presented below.

To systematically study the effect of the ball-milling time, we kept all parameters except ball-milling time fixed. The samples were hot pressed at 600 ^{o}C at a pressure of 80 MPa for 5 minutes.

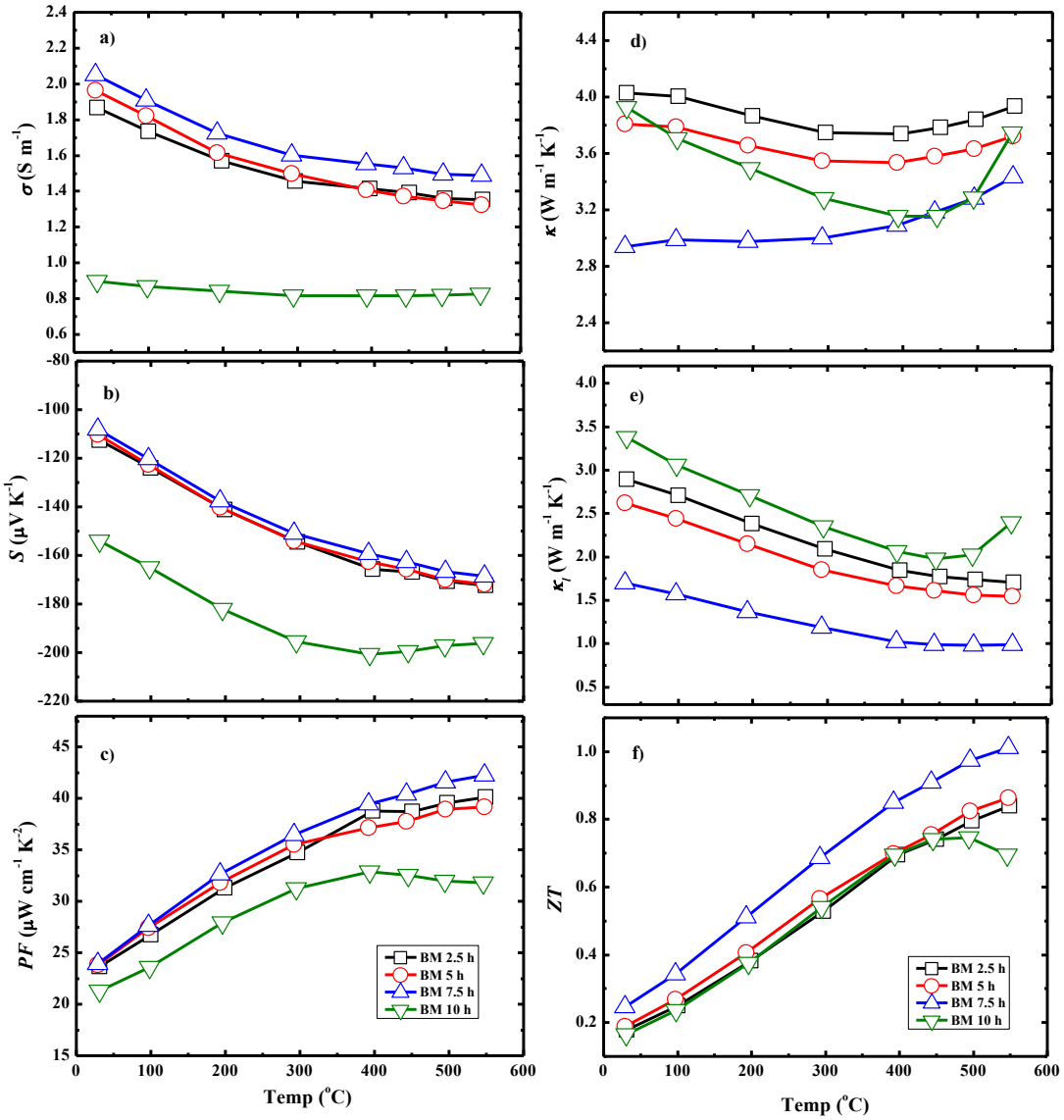

Fig. 4.2.1 Temperature-dependent thermoelectric properties of $Yb_{0.35}Co_4Sb_{12}$ at different ball-milling time: a) electrical conductivity, b) Seebeck coefficient, c) power factor, d) thermal conductivity, e) lattice thermal conductivity, and f) *ZT*.

The temperature-dependent electrical conductivity of the samples made after different ball-milling time is presented in Fig. 4.2.1a. The electrical conductivity of the samples made after 2.5 h and 5 h ball-milling is almost the same in the entire temperature range. The electrical conductivity of the sample made after 7.5 h ball-milling has better electrical conductivity than the sample made from 2.5 h and 5 h ball-milled powder. In general, the electrical conductivity of the sample decreases with ball-milling time due to a significant scattering of carriers from smaller grains. The observed higher electrical conductivity from a longer ball-milled sample may be due to the higher mobility of the charge carrier from dense sample (the measured densities of the samples hot pressed after 2.5 h, 5 h, 7.5 h, and 10 h are 7.56, 7.64, 7.71, and 7.72 g cm^{-3}, respectively). Another possibility of higher electrical conductivity may be the better solubility of Yb in the matrix due to longer ball-milling time. However, the electrical conductivity of the sample made after 10 h ball-milling has the lowest electrical conductivity, which may be due to the defects in the sample due to a longer high energy ball-milling.

The temperature-dependent Seebeck coefficient is plotted in Fig. 4.2.1b. The measured Seebeck coefficient of all samples are negative, implying that electrons are majority charge carriers. The observed Seebeck coefficient is consistent with the electrical conductivity measurement.

The temperature-dependent power factor is plotted in Fig. 4.2.1c. The *PF* of all samples increases with temperature in the entire temperature except for 10 h ball-milled sample. The power factor of the sample ball milled for 7.5 h is the highest in entire temperature

range. A maximum power factor of ~42 μW cm^{-1} K^{-2} at 550 ^{o}C is obtained in 7.5 h ball-milled sample.

The temperature-dependent thermal conductivity is plotted in Fig. 4.2.1d. The thermal conductivity decreases with ball-milling time, attains the minimum value for 7.5 h ball milled sample in the entire temperature range and then increases again for 10 h ball milled sample. The decrease in thermal conductivity can be understood as the phonon scattering off from numerous boundaries created due to nanostructuring [1]. The high magnification SEM images shown in Fig. 4.2.2 shows decreased grain size with increasing ball-milling hours. Higher thermal conductivity in a 10 h ball-milled sample may be due to the presence of defects. The electronic contribution to thermal conductivity can be calculated using Wiedemann-Franz relation: $\kappa_e = \sigma LT$, where σ is the electrical conductivity, L is the Lorenz number, and T is the absolute temperature. The lattice contribution is then enumerated by subtracting the electronic contribution from the total thermal conductivity. The temperature-dependent lattice thermal conductivity is shown in Fig. 4.2.1e. The lattice thermal conductivity decreases with ball-milling time. The lowest lattice thermal conductivity is achieved in a sample ball milled for 7.5 h.

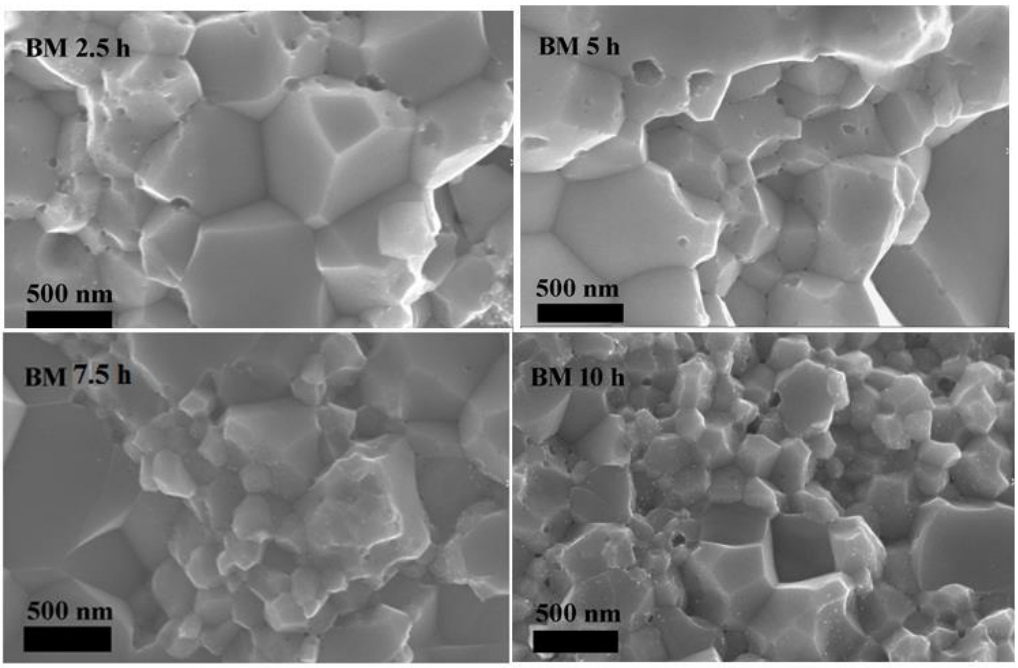

Fig. 4.2.2 High magnification SEM images of the sample hot pressed after different ball-milling time. Longer ball-milling time reduces the grain size.

The temperature-dependent dimensionless figure-of-merit, *ZT* of all samples is plotted in Fig. 4.2.1f. The *ZT* of the sample ball milled for 7.5 h is the highest in the entire temperature range, indicating 7.5 h is the optimized ball-milling time.

4.3 Optimization of Hot Press Temperature

One of the various factors that affects thermal and electrical transport is the grain size, which depends on the ball-milling time and the hot press conditions. In general, the grain size becomes bigger with higher hot press temperature. To study the effect of hot pressing temperature, we fixed the ball-milling time, hot pressing pressure and hot press holding

time and varied the hot press temperature from 600 ^{o}C to 800 ^{o}C, and their thermoelectric properties were measured. The details of experimental observation is discussed in the following paragraphs.

The temperature-dependent electrical conductivity is shown in Fig. 4.3.1a. The electrical conductivity of the sample hot pressed at 600 ^{o}C is the lowest while the sample hot pressed at 800 ^{o}C has the highest electrical conductivity. With the lower hot press temperature, the grain size becomes smaller which will scatter more carriers. However, grain size becomes larger with a higher hot press temperature and the scattering of the charge carrier is less affected, resulting higher electrical conductivity. The temperature-dependent Seebeck coefficient plotted in Fig 4.3.1b is consistent with the general expectation except for the sample hot pressed at 600 ^{o}C. The temperature-dependent power factor of the sample is shown in Fig 4.3.1c. The *PF* increased with hot press temperature and has a maximum value for the sample hot pressed at 750 ^{o}C. The sample hot pressed above this temperature has inferior power factor.

The temperature-dependent thermal conductivity is plotted in Fig 4.3.1d. The thermal conductivity of the sample increases with an increasing hot press temperature. The increases in thermal conductivity of the sample hot pressed at a higher temperature can be attributed to reduction of phonon scattering from bigger grains. The SEM images plotted in Fig. 4.3.2 confirms the bigger grain in a sample hot pressed at a higher temperature. We observed a wide range of grain size distribution (from about 200 nm to 1 micron) in the sample hot pressed at 750 ^{o}C. With such a grain-size distribution, we expect the scattering of phonons of different length scale [2]. With bigger grains, we have few interfaces for

phonon scattering. Since the electrical conductivity of the sample hot pressed at a higher temperature is high, the electronic contribution to total thermal conductivity increases, which makes higher thermal conductivity.

The temperature-dependent dimensionless figure-of-merit, *ZT* is plotted in Fig 4.3.1e. The highest *ZT* value is found in a sample hot pressed at 750 ^{o}C. So, for Yb-filled skutterudites, the optimized hot pressed temperature was taken as 750 ^{o}C.

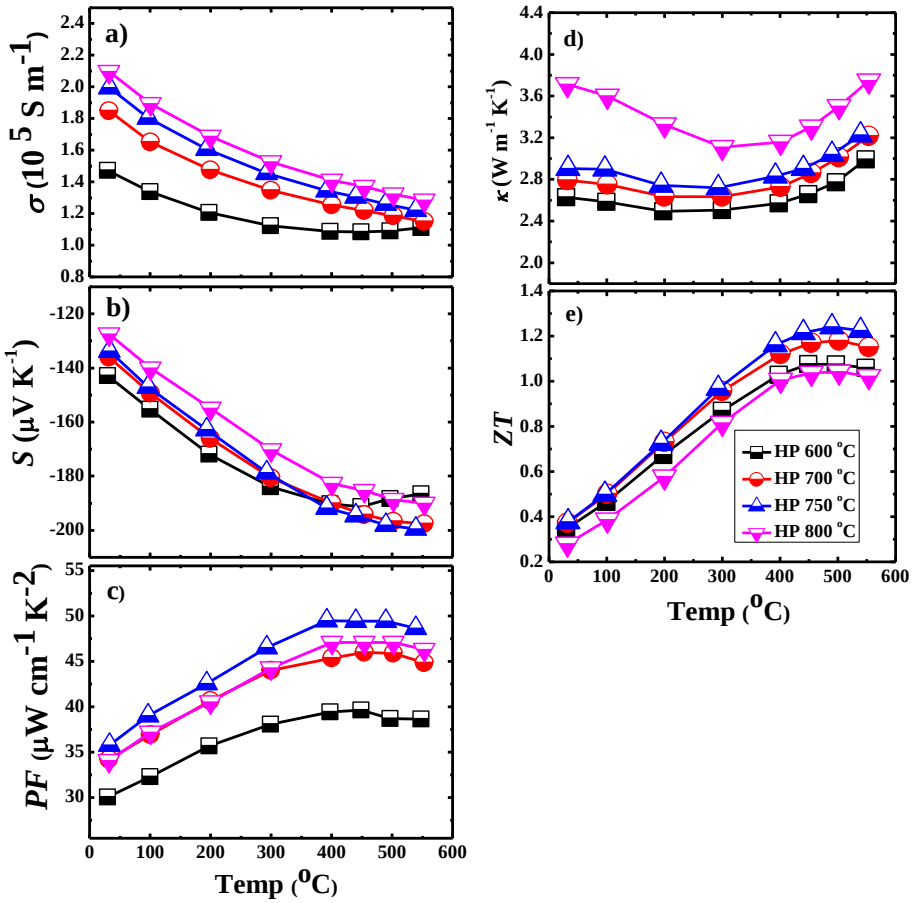

Fig 4.3.1 Temperature-dependent thermoelectric properties of $Yb_{0.35}Co_4Sb_{12}$ hot pressed at different temperature: a) electrical conductivity, b) Seebeck coefficient, c) power factor, d) total thermal conductivity, and e) *ZT*.

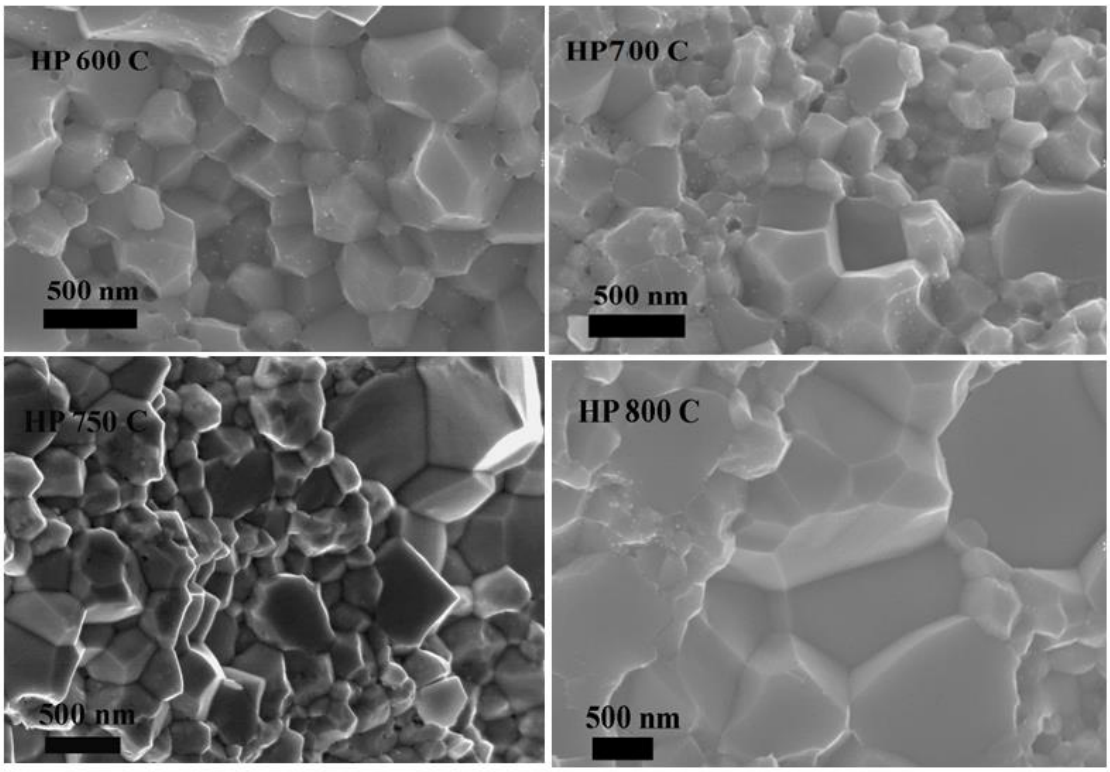

Fig. 4.3.2 High magnification SEM images of the sample hot pressed at different temperatures. The grain becomes bigger with higher hot press temperature.

4.4 Optimization of Hot Pressing Pressure

Once the hot pressing temperature and ball-milling time were optimized, another parameter that was optimized is hot pressing pressure. Hot pressing pressure also has a direct effect on controlling the density and grain size of the sample. In this section, we will briefly discuss the effect of hot pressing pressure in TE properties of the samples.

The temperature-dependent electrical conductivities of the samples hot pressed at different pressure is shown in Fig. 4.4.1a. The electrical conductivity of the sample hot pressed at different pressure does not vary significantly. For the same hot pressing temperature, the sample hot pressed at higher pressure has a higher mass density and is believed to have higher electrical conductivity due to the higher mobility of the carrier. Considering the uncertainty in the electrical conductivity measurement by about 5% in ZEM-3 system, all of the data lie in the error range. The temperature-dependent Seebeck coefficient plotted in Fig. 4.4.1b is consistent with the electrical conductivity measurement. The temperature-dependent power factor is plotted in Fig. 4.4.1c. The power factor of the sample hot pressed at 55 MPa is the highest. The temperature-dependent total thermal conductivity plotted in Fig. 4.4.1d indicated that the thermal conductivity of samples hot pressed at various pressure does not vary significantly. The high magnification SEM images plotted in Fig. 4.4.2 show that the grain size distribution in the sample hot pressed at different pressures do not vary significantly, which is why the thermal conductivity of all samples is similar. The temperature-dependent dimensionless figure-of-merit is plotted in Fig. 4.4.1e. The *ZT* value of samples hot pressed at different pressure is almost the same in the entire temperature range. However, we achieved a peak *ZT* ~1.32 in the sample hot pressed at a pressure of 55 MPa. So, the optimized hot pressing pressure was determined to be 55 MPa for Yb-filled *n*-type skutterudites.

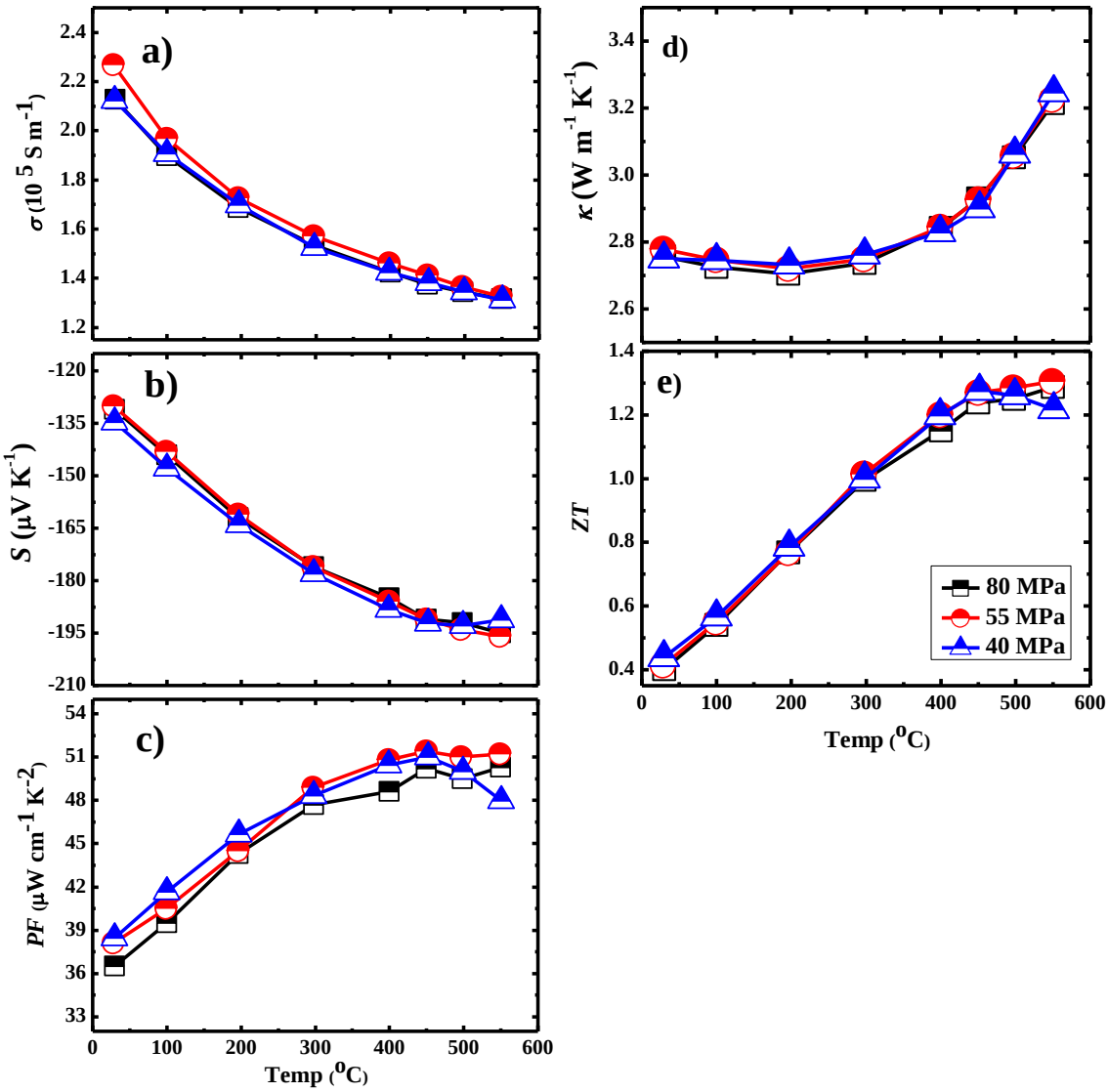

Fig 4.4.1 Temperature-dependent thermoelectric properties of $Yb_{0.35}Co_4Sb_{12}$ hot pressed at different pressure: a) electrical conductivity, b) Seebeck coefficient, c) power factor, d) total thermal conductivity, and e) *ZT*.

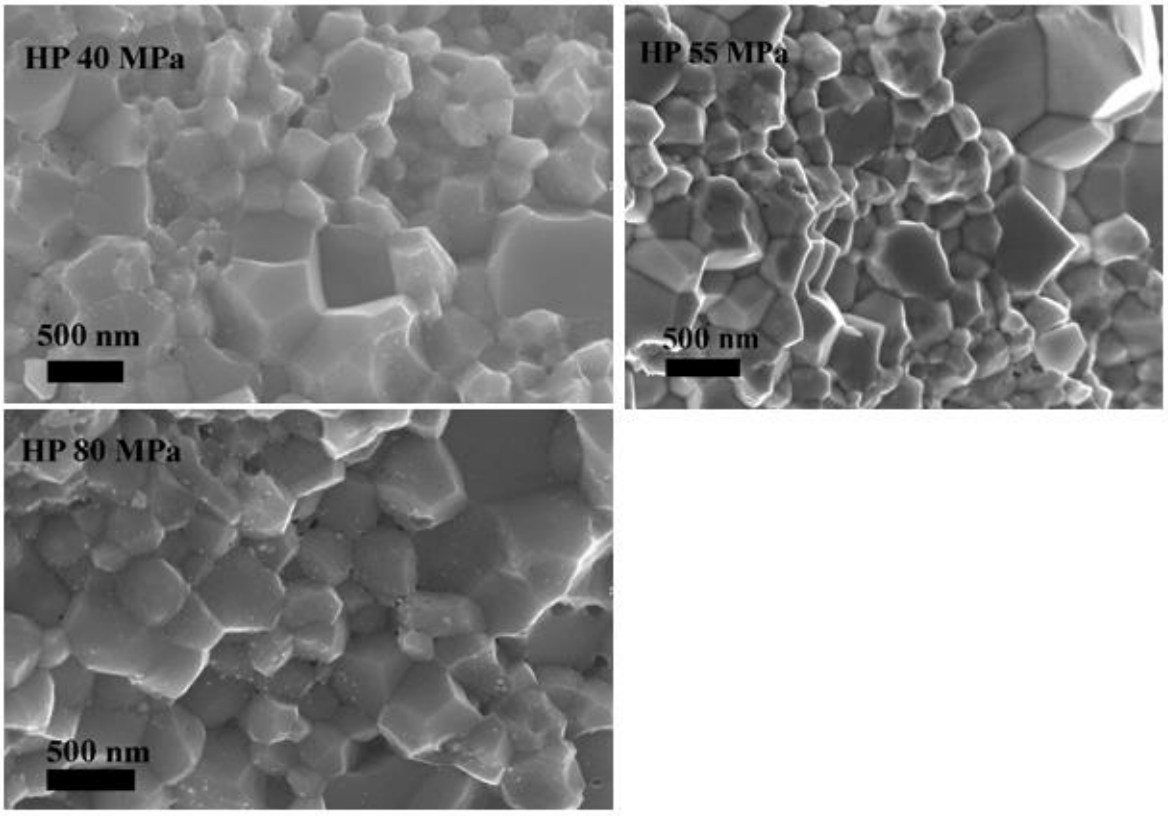

Fig. 4.4.2 High magnification SEM image of samples hot pressed at different pressure.

4.5 Optimization of Hot Press Holding Time

Another parameter that needs optimization is the hot press holding time at higher temperature**.** Once the ball-milling time, hot press temperature, and hot pressing pressure was optimized, we studied the thermoelectric properties of the samples made under different hot press holding time. The details of experimental findings are summarized in Fig. 4.5.1

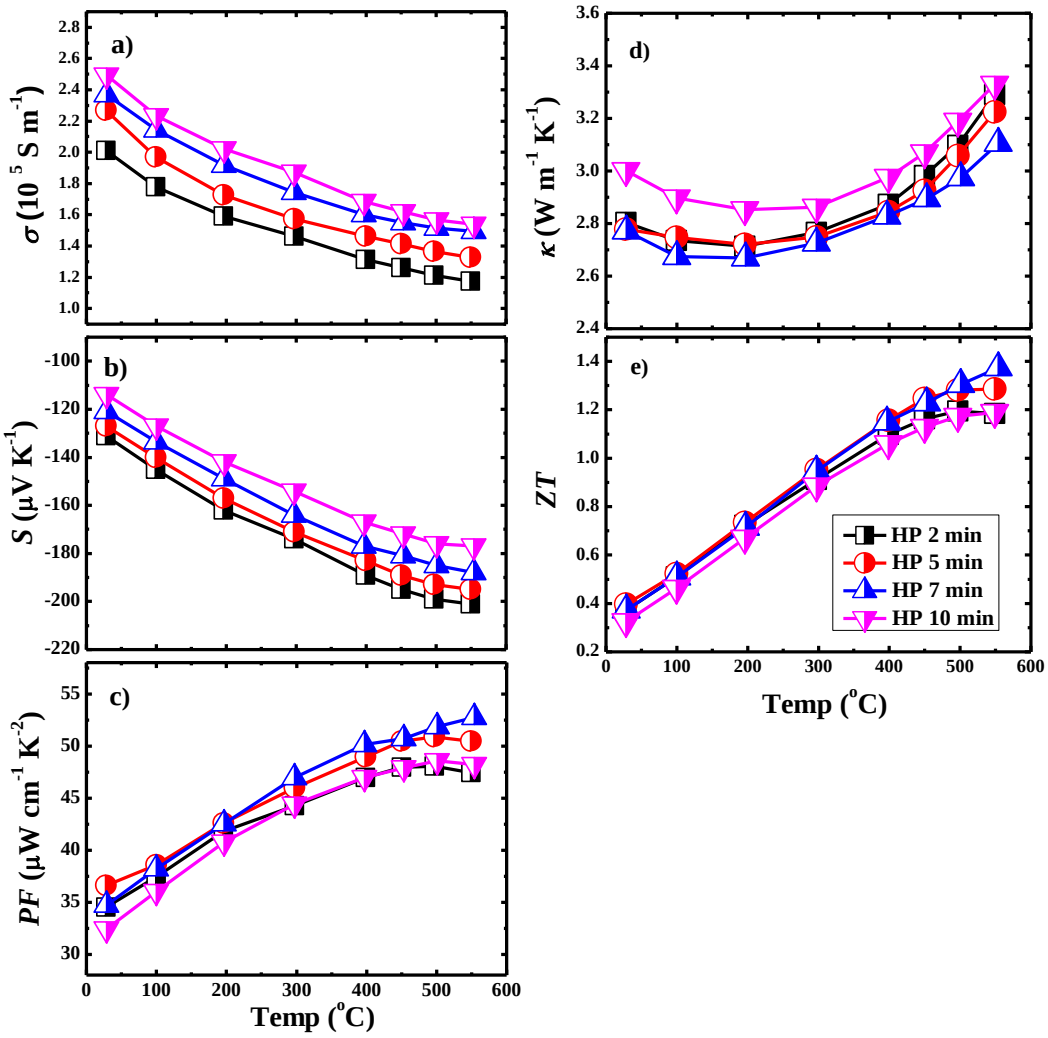

Fig 4.5.1 Temperature-dependent thermoelectric properties of $Yb_{0.35}Co_4Sb_{12}$ hot pressed at different hot press holding time: a) electrical conductivity, b) Seebeck coefficient, c) power factor, d) total thermal conductivity, and e) *ZT*.

With the longer holding time, the electrical conductivity (Fig. 4.5.1a) of sample was increased, possibly due to less scattering of the charge carrier from bigger grains. The

temperature-dependent Seebeck coefficient plotted in Fig. 4.5.1b is consistent with the electrical conductivity measurement. The temperature-dependent power factor (Fig. 4.5.1c) of the sample hot pressed for 5 minutes does not vary significantly with the *PF* of the sample hot pressed for 10 minutes. However, the *PF* of the sample (Fig. 4.5.1c) hot pressed for 7 minutes (~53 $\mu W\ cm^{-1}\ K^{-2}$) is higher than the *PF* (~49 $\mu W\ cm^{-1}\ K^{-2}$) of the sample hot pressed for 5 minutes, which is due to better electrical conductivity of the sample hot pressed for 7 minutes. The temperature-dependent thermal conductivity (Fig. 4.5.1d) shows that there is not much difference in thermal conductivity in the sample hot pressed for 2 minutes and 5 minutes. The SEM images shown in Fig 4.5.2 indicates that there is not significant difference in grain size in the samples made by hot pressing 2 minutes and 5 minutes respectively. The sample hot pressed for 10 minutes has the highest thermal conductivity, possibly because of the bigger grains. In the entire temperature range, the thermal conductivity of the sample hot pressed for 7 minutes is the least. The temperature-dependent dimensionless figure-of-merit, *ZT* is calculated from the measured power factor and thermal conductivity and is plotted in Fig. 4.5.1e. A peak *ZT* ~1.4 at around 550 ^{o}C is achieved in the sample hot pressed for 7 minutes.

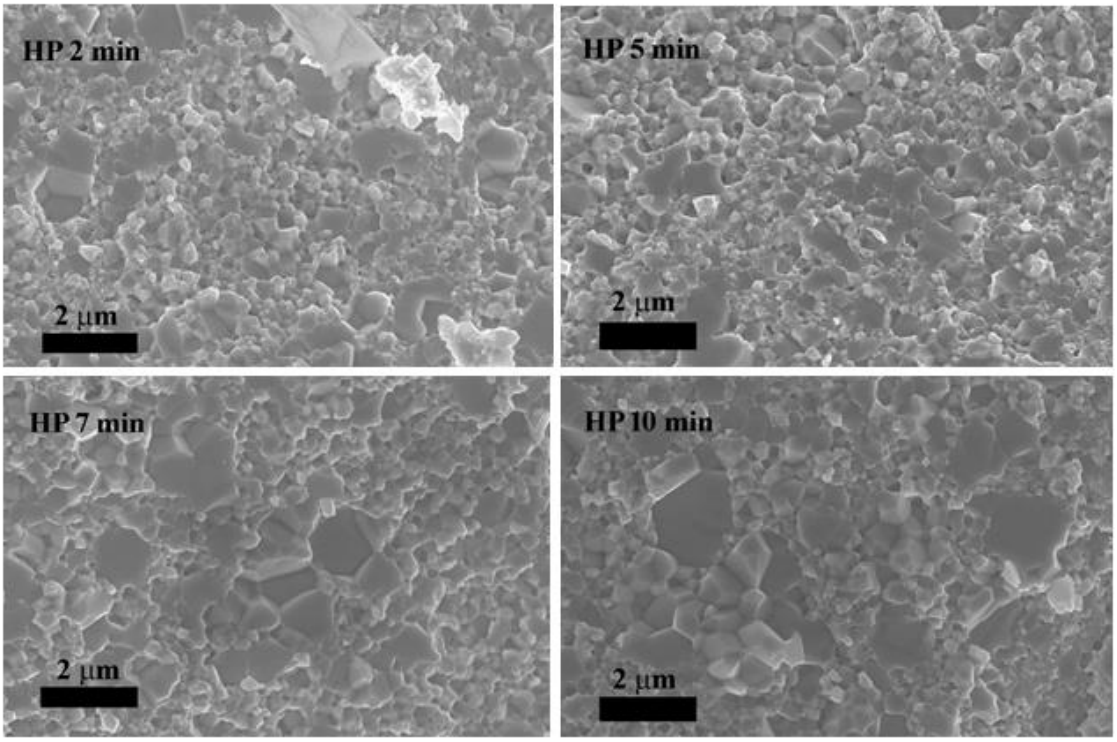

Fig. 4.5.2 Low magnification SEM images of the sample hot pressed for different holding time. Longer holding time results bigger grain size.

4.6 Summary

n-type skutterudites $Yb_{0.35}Co_4Sb_{12}$ samples were synthesized by general melt-quench-ball mill- hot press method. A systematic study on the effect of various physical parameters on thermoelectric performance of the material was investigated. Based on step-by-step experiments, the optimized ball-milling time, hot press temperature, hot pressing pressure, and hot press holding time were found to be 7.5 h, 750 ^{o}C, 55 MPa, and 7 minutes, respectively.

4.7 References

1. Poudel *et al.*, *Science* **2008**, 320, 634.

2. Biswas *et al.*, *Nature* **2012**, 489, 414.

Chapter 5

Thermoelectric Performance of *p*-type Skutterudites

A part of this chapter contains our previously published work *Thermoelectric performance of Ni compensated cerium and neodymium double-filled p-type skutterudites,* Phys. Chem. Chem. Phys. **16,** 18170 (2014).

http://pubs.rsc.org/en/content/articlepdf/2014/cp/c4cp00383g

A part of this chapter is submitted for publication in Physical Review Applied.

5.1 Introduction

p-type skutterudites are formed when Co is partially or fully replaced by Fe in "RCo_4Sb_{12}". Generally, "RFe_4Sb_{12}" is the host frame for *p*-type skutterudites. For the same filler *R*, "RFe_4Sb_{12}" has four electrons less than "RCo_4Sb_{12}", indicating a higher hole density in the *p*-type skutterudites. Higher hole density in this system suggests that the Fermi level is deep inside the valance band and therefore the number of available states near the Fermi level is low, making the Seebeck coefficient small. Together with void filling and alloying Fe with Co or Ni, the Fermi level can be pushed towards the edge of the valance band, resulting a higher Seebeck coefficient. However, the partial substitution of Fe by Co or Ni has an adverse effect on both electrical and thermal transport behavior. At a higher temperature, the minority charge carriers acquire enough thermal energy to move across the band gap, which suppresses the electrical conduction because electron conduction is negated by hole conduction due to their flow in opposite direction ($\sigma = \sigma_e + \sigma_h$). Besides

the suppressed electrical conductivity, a strong bipolar effect in thermal conductivity at a high temperature is observed. Both of these effects impact the optimization of *ZT* adversely.

Considering the thermoelectric device, a unit couple consisting of both *p*-type and *n*-type material is required. The device efficiency can be expressed as,

$$\eta = \left(1 - \frac{T_c}{T_h}\right) \frac{\sqrt{1 + ZT_{av}} - 1}{\sqrt{1 + ZT_{av}} + {T_h}/{T_c}} \qquad (5.1.1)$$

where *ZT* for the device can be expressed as,

$$ZT = \frac{(S_h - S_e)^2 T}{\left[\left(\rho_h \kappa_h\right)^{1/2} + \left(\rho_e \kappa_e\right)^{1/2}\right]^2} \qquad (5.1.2)$$

To have better device performance, improving the thermoelectric performance of *p*-type skutterudites is required.

In this chapter, we will present some of our investigation on improving the thermoelectric performance of *p*-type skutterudites.

5.2 Thermoelectric Performance of Misch Metal-filled *p*-type Skutterudites

Most of the research focused on improving the thermoelectric figure-of-merit, *ZT* of *p*-type skutterudites are based on using single or double fillers. However, few authors have reported a systematic study of effect of multiple fillers in the electrical and thermal transport properties of *p*-type skutterudites [1, 2]. Keeping in mind that multiple fillers with

different atomic masses and different ionic radii could possibly scatter off phonons of different mean free paths, leading to an improved *ZT*, a systematic study of TE properties of rare earth-based misch metal (Mm = $La_{0.25}Ce_{0.50}Pr_{0.05}Nd_{0.15}Fe_{0.03}$) filled *p*-type skutterudites was carried out. The samples were made by general melting-quenching-annealing-dc hot pressing the nano-powder in a graphite die at 650 ^{o}C at 80 MPa for 5 minutes. To investigate the effect of misch metal in the thermoelectric performance, we first tuned the concentration of misch metal keeping the Fe/Co ratio fixed to achieve the best results. Based on those experiments, we chose the best misch metal concentration and tuned the Fe/Co ratio to further improve the TE properties. The experimental findings are discussed in the following paragraphs.

Fig. 5.2.1a shows the XRD spectra of all four samples ($Mm_{0.9}Fe_{4-x}Co_xSb_{12}$, x = 0.7, 0.8, 0.9, and 1). Most of the samples show pure skutterudites phase except for the sample with x = 0.7. The secondary phase present in the sample with x = 0.7 may be Fe/$FeSb_2$. Fig. 5.2.1b shows the lattice parameter as a function of cobalt concentration, x. Since the ionic radii of Co is smaller than Fe, the lattice parameter of the sample decreases with increasing cobalt concentration and follows the Vegard law.

Fig. 5.2.2 shows SEM images at low (Fig. 5.2.2a) and high (Fig. 5.2.2b) magnification of the freshly broken surface of the hot pressed sample $Mm_{0.9}Fe_{3.1}Co_{0.9}Sb_{12}$. From SEM images, we observed that the majority of the grains are in the range of 200-500 nm, while some of them are as big as a micrometer. There is no grain texturing, which leads to isotropic properties. With smaller grains, we have numerous boundaries to scatter phonons [3]. The TEM image shown in Fig. 5.2.2c further confirms the grain size observed by SEM

images. The SEM images show that the crystalline grains are closely packed, an indication of high mass volume density. The measured densities (7.70, 7.73, 7.71, and 7.69 g cm^{-3} for x = 0.7, 0.8, 0.8, and 1.0, respectively) of all samples are more than 97% of the theoretical density. The high resolution TEM image (Fig. 5.2.2d) shows that boundaries between grains are very clean and sharp, which is also beneficial for electron transport.

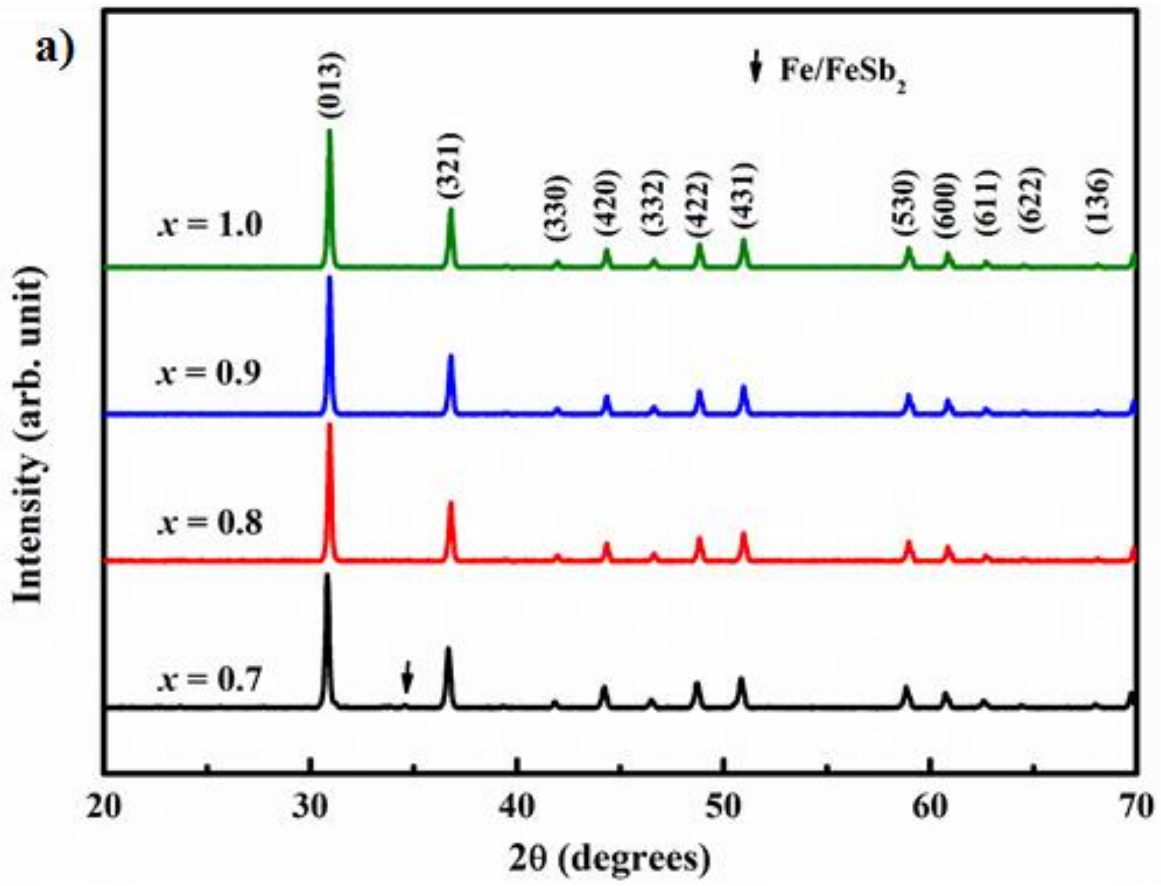

Fig. 5.2.1a XRD spectra of $Mm_{0.9}Fe_{4-x}Co_xSb_{12}$ (x = 0.7, 0.8, 0.9, and 1). Most of the samples show pure skutterudites phase except for the sample for x = 0.7.

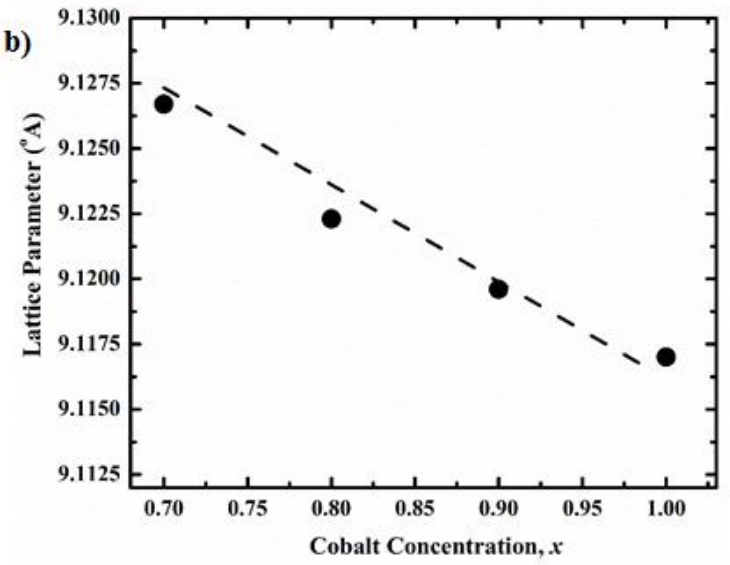

Fig. 5.2.1b Lattice parameter as a function of cobalt concentration.

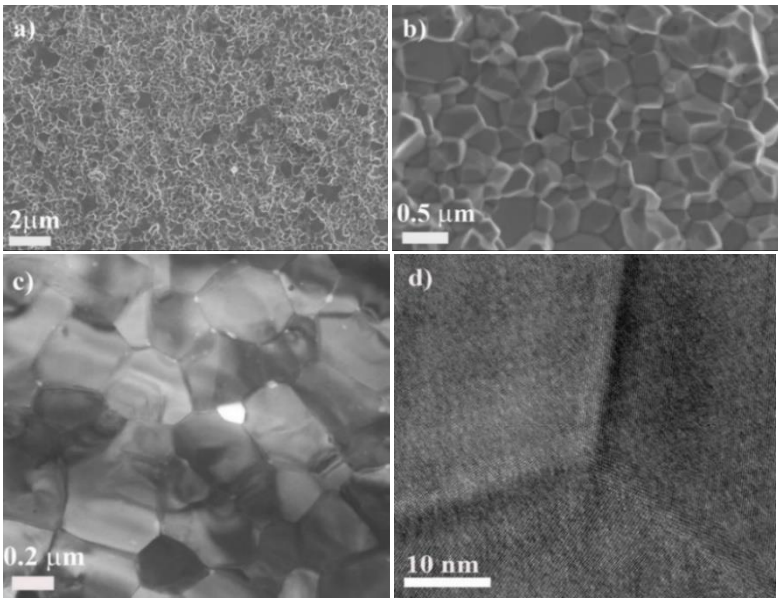

Fig. 5.2.2 SEM images at (a) low and (b) high magnification and TEM images at (c) low and (d) high magnification of $Mm_{0.9}Fe_{3.1}Co_{0.9}Sb_{12}$, showing grain size, crystallinity, and grain boundary.

The room temperature carrier concentration and the mobility of the charge carriers as a function of cobalt concentration x is plotted in Fig. 5.2.3. The carrier concentration decreases with increasing cobalt concentration and ranges from 4.96×10^{21} cm^{-3} for $x = 0.7$ to 2.67×10^{21} cm^{-3} for $x = 1$. Higher cobalt content gives more electrons to the host system and effectively lowers the hole concentration. The room temperature mobility of the charge carrier ranges from ~1.76 cm^2 V^{-1} S^{-1} for $x = 0.7$ to ~1.90 cm^2 V^{-1} S^{-1} for $x = 1$.

The temperature-dependent electrical conductivity of all $Mm_{0.9}Fe_{4-x}Co_xSb_{12}$ ($x = 0.7$, 0.8, 0.9, and 1.0) samples is shown in Fig. 5.2.4a. The electrical conductivity of all samples decreases with temperature, a signature of heavily doped semi-conductor. Since the filler concentration is fixed, the electrical conductivity is determined by the Fe/Co ratio. The electrical conductivity of the sample with lower cobalt concentration is high, which is due to the higher hole concentration (Fig. 5.2.3). The effect of higher cobalt concentration at an elevated temperature becomes more significant. At higher temperatures, the thermal energy is high enough to excite the minority charge carrier (electrons in this case) across the band gap, leading to a mixed conduction, which lowers the electrical conductivity.

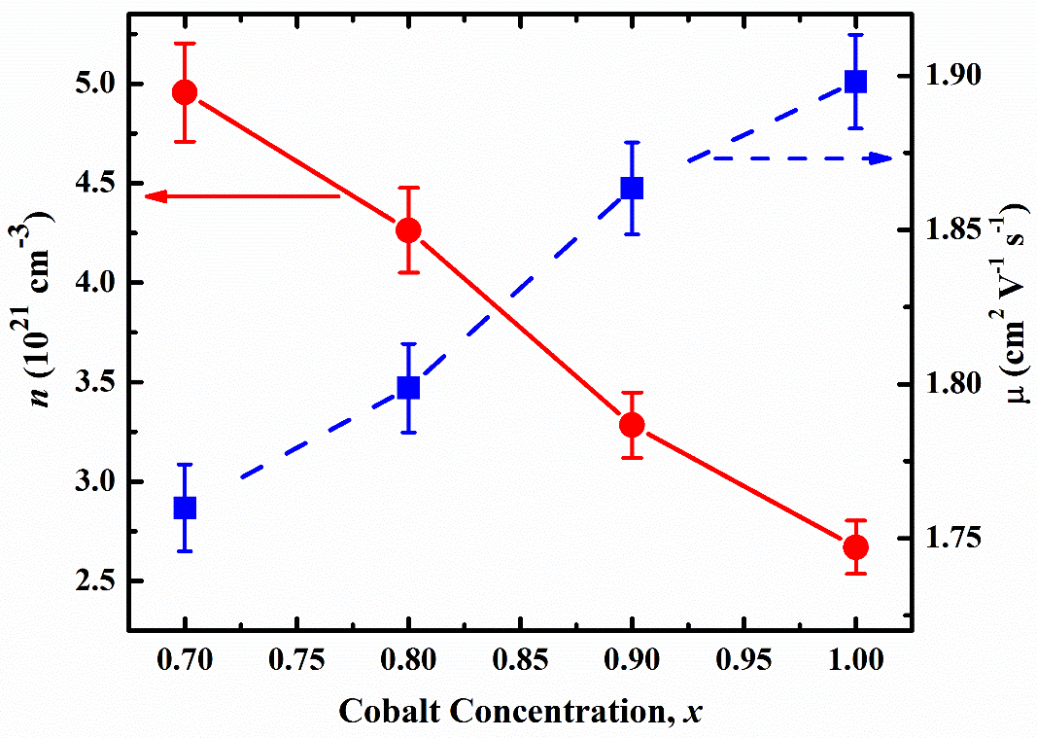

Fig. 5.2.3 Carrier concentration and hall mobility of $Mm_{0.9}Fe_{4-x}Co_xSb_{12}$ (x = 0.7, 0.8, 0.9, and 1). Carrier concentration decreases while mobility increases with increasing cobalt.

The temperature-dependent Seebeck coefficient is shown in Fig. 5.2.4b. The Seebeck coefficient of all samples is positive, implying that the holes are majority charge carriers. The Seebeck coefficient of the sample with higher cobalt concentration is higher because of the lower electrical conductivity. The Seebeck coefficient of most metals and degenerate semi-conductors is given by the Mott relation as [4],

$$S = \frac{\pi^2 \kappa_B^2 T}{3q}\left\{\frac{1}{n}\frac{dn}{dE} + \frac{1}{\mu}\frac{d\mu}{dE}\right\}_{E=E_f} \qquad (5.2.1)$$

With increased Co concentration: (a) the hole concentration decreases (Fig. 5.2.3), and (b) the Fermi level moves towards the edge of the valance band, increasing the number of available states per unit energy range near the Fermi level, which results in a higher Seebeck coefficient. The Seebeck coefficient of all samples increases with temperature, attains a maximum value at around 475 ^{o}C, and then decreases with temperature, a signature of bipolar conduction. However, for the sample with x = 0.7, the Seebeck coefficient keeps increasing from room temperature to about 525 ^{o}C. Using the measured Seebeck voltage, the value of band gap (E_g) in a semi-conductor can be roughly estimated using $E_g = 2eS_{max}T_{max}$, where e is the elementary charge, S_{max} is the peak Seebeck coefficient, and T_{max} is the temperature corresponding to the peak Seebeck coefficient [5]. The estimated band gap of the samples lies in the range of 0.29 to 0.32 eV, consistent with the values reported.

The temperature-dependent power factor is shown in Fig. 5.2.4c. The power factor of all samples increases with temperature up to about 425 ^{o}C and then decreases except for x = 0.7. With increasing cobalt concentration, the temperature corresponding to the highest power factor shifts towards a lower temperature regime, consistent with what we expect in a material with bipolar conduction. The highest power factor of ~30 μW cm^{-1} K^{-2} is obtained at about 425 ^{o}C in $Mm_{0.9}Fe_{3.1}Co_{0.9}Sb_{12}$.

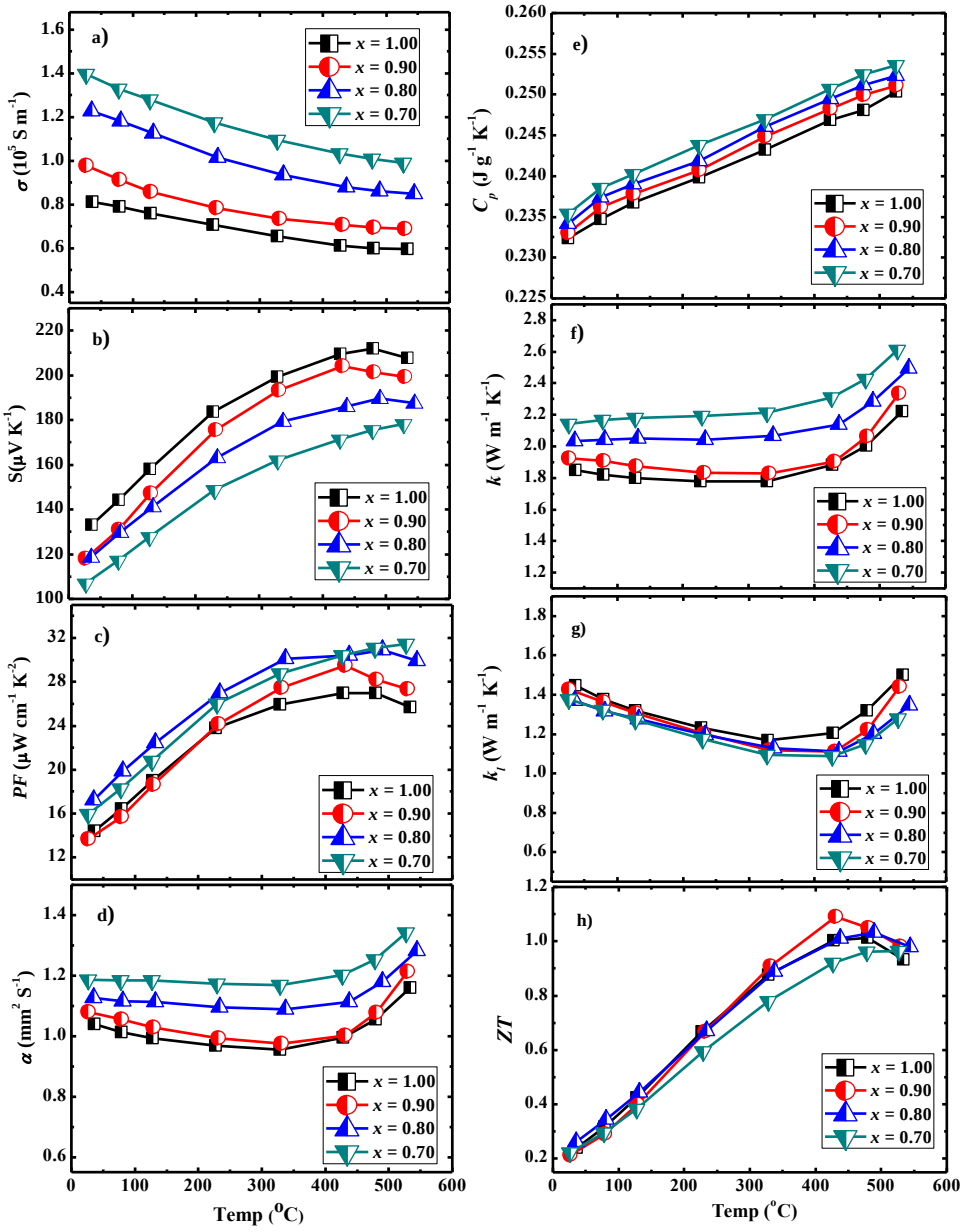

Fig. 5.2.4 Temperature-dependent thermoelectric properties of $Mm_{0.9}Fe_{4-x}Co_xSb_{12}$ for x = 0.7, 0.8, 0.9, and 1: a) electrical conductivity, b) Seebeck coefficient, c) power factor, d) thermal diffusivity, e) specific heat capacity, f) total thermal conductivity, g) lattice thermal conductivity, and h) dimensionless figure-of-merit, *ZT*.

The temperature-dependent thermal diffusivity (α) for all samples is shown in Fig. 5.2.4d. The thermal diffusivity of all samples decreases with temperature up to about 325 ^{o}C, attains the minimum value, and then increases with temperature. The rise in thermal diffusivity after 325 ^{o}C for the samples with x = 0.9 and 1 is more than the samples with x = 0.7 and 0.8. The thermal diffusivity varies from ~1.04 mm^2 S^{-1} at room temperature to ~1.16 mm^2 S^{-1} at about 535 ^{o}C in $Mm_{0.9}Fe_{3.1}Co_{0.9}Sb_{12}$, the sample that gave the best ZT value.

The temperature-dependent specific heat capacity (C_p) of $Mm_{0.9}Fe_{4-x}Co_xSb_{12}$ (x = 0.7, 0.8, 0.9, and 1.0) is shown in Fig. 5.2.4e. C_p of all samples increases with temperature and lies in between ~0.232-0.235 J g^{-1} K^{-1} at room temperature and ~0.250-0.254 J g^{-1} K^{-1} at about 535 ^{o}C.

The temperature-dependent total thermal conductivity κ for all samples is shown in Fig. 5.2.4f. For the sample with x = 0.7 and 0.8, κ remains almost constant up to about 325 ^{o}C and then increases with temperature. However, for the samples with x = 0.9 and 1.0, the total thermal conductivity decreases with temperature up to about 325 ^{o}C and then increases sharply after 425 ^{o}C. For the samples with higher cobalt concentration, a significant number of electrons move across the band gap together with holes at elevated temperature, a well-known bipolar conduction in *p*-type skutterudites. The thermal conductivity of such system can be written as [6],

$$\kappa_T = \kappa_e + \kappa_h + \kappa_l + \frac{\sigma_e \sigma_h}{\sigma_e + \sigma_h}(S_h - S_e)^2 T \qquad (5.2.2)$$

where κ_e, κ_h, κ_l, σ_e, σ_h, S_e, and S_h are the electron thermal conductivity, hole thermal conductivity, lattice thermal conductivity, electrical conductivity due to electrons and holes, and Seebeck coefficient for electrons and holes respectively. At high temperatures, both electrons and holes contribute to conduction, thus giving a parabolic behavior of thermal conductivity.

In general, the total thermal conductivity can be written as the sum of the thermal contribution from the carriers and from the lattice vibration. However, in *p*-type skutterudites with smaller the Fe/Co ratios, the contribution from the minority charge carrier (electrons in this case) as well as bipolar contribution becomes significant. The estimation of bipolar contribution to total thermal conductivity requires Seebeck voltage and electrical conductivity due to both electrons and holes at higher temperature. Since we do not exactly know the effective mass of carriers in the conduction band and the valance band at higher temperature, the estimation of carrier contribution and bipolar contribution to the total thermal conductivity becomes less reliable. The carrier contribution to the total thermal conductivity can be calculated using the Wiedemann-Franz relation given by $\kappa_e = \sigma LT$, where σ is the electrical conductivity, L is the Lorenz number, and T is the absolute temperature. In this calculation, we assumed that the acoustic phonon scattering is the dominant mechanism for carrier scattering and evaluated the temperature-dependent Lorenz number from the reduced Fermi energy deduced from the Seebeck coefficient at room temperature based on a single parabolic band model [7]. The lattice part of thermal conductivity can be derived from the total thermal conductivity by subtracting the carrier contribution. The temperature-dependent lattice thermal conductivity is plotted in Fig.

5.2.4g. The lattice part of thermal conductivity of all samples first decrease with temperature, indicating that the phonon transport is hindered by the dynamic process of Umklapp scattering. In case of the Umklapp phonon-scattering process, the lattice part of thermal conductivity can be expressed as,

$$\kappa_l = 3.5\left(\frac{\kappa_B}{h}\right)\frac{MV^{1/3}\theta_D^3}{\gamma^2 T} \qquad (5.2.3)$$

where M is the average mass per atom, V the average atomic volume, θ_D the Debye temperature, and γ the Grüneisen parameter. κ_l of all samples reaches a minimum value at around 425 ^oC, except for the sample with x =1, then increases with increasing temperature. This may be due to the additional heat carried by electron-hole pair generated from the intrinsic excitation at high temperature. One way to minimize κ_l is to increase the value of Grüneisen parameter, γ, which can be obtained by increasing the anharmonicity of fillers. The bipolar conduction can be minimized if we push the turning point of thermal conductivity at a higher temperature by increasing hole concentration. However, the increased carrier concentration increases the carrier part of thermal conductivity and simultaneously affects the Seebeck coefficient adversely, reducing the overall performance of the material. Band gap opening at higher temperature also prevents the excitation of the electron-hole pair and minimizes the bipolar conduction, which should be further studied to achieve such a goal.

The temperature-dependent dimensionless figure-of-merit, ZT, is calculated from the measured value of temperature-dependent electrical conductivity (σ), the Seebeck coefficient (S), and the thermal conductivity (κ) and is plotted in Fig. 5.2.4h. The ZT of all

samples increases with temperature. However, the peak *ZT* position for samples is observed at different temperatures. For the sample with a higher cobalt concentration *x*, the peak *ZT* is shifted towards lower temperature, an indication of bipolar effect at lower temperature. A peak *ZT* ~1.1 is achieved at 425 ^{o}C in $Mm_{0.9}Fe_{3.1}Co_{0.9}Sb_{12}$, which is comparable to some of the best results reported previously [8, 9]. The shift in peak *ZT* to a lower temperature makes the average *ZT* value higher, which could potentially increase the conversion efficiency.

5.3 Thermoelectric Performance of La/Ce Double-filled *p*-type Skutterudites

In solids, most of the heat carrying phonons have lower vibrational frequencies. Liu *et al*., have calculated the vibrational frequencies of various fillers in [111] direction of Fe-based *p*-type skutterudites RFe_4Sb_{12} and RFe_3CoSb_{12} [10]. The calculation reveals that the vibrational frequencies of filler does not change significantly even if Fe/Co ratio is changed. Since the calculated vibrational frequencies of La and Ce (79 cm^{-1} and 73 cm^{-1}, respectively) in RFe_4Sb_{12} is small, we have synthesized the La/Ce double-filled *p*-type skutterudites and their thermoelectric properties are measured.

Fig. 5.3.1 shows the XRD pattern of four samples ($La_{0.68}Ce_{0.22}Fe_{4-x}Co_xSb_{12}$, x = 0.4, 0.5, 0.6, and 0.8) studied. All of the peaks can be well indexed, indicating the formation of pure skutterudites phase within the detectability of the XRD machine. Fig. 5.3.2 shows the lattice parameter of samples as a function of Co concentration. The lattice parameter decreases with increasing Co concentration, and follows the Vegard law. The decrease in

lattice parameter with increasing amount of Co is due to the smaller ionic radii of Co than Fe.

Fig. 5.3.3 shows the SEM images at low (Fig. 5.3.3a) and high (Fig. 5.3.3b) magnification of the freshly broken surface of the hot pressed sample. From the SEM images, we have observed that the majority of grains are of a few hundred nanometers in size while a few are as big as micron. There is no grain texturing, leading to isotropic properties. With smaller grains, we have a number of boundaries to scatter phonons [3]. The grain size is further confirmed by TEM image (Fig. 5.3.3c). The SEM images shows that the crystallized grains are closely packed, indicating high volume mass density (7.72, 7.69, 7.74, 7.72 g cm^{-3} for x = 0.4, 0.5, 0.6, and 0.8, respectively please list the densities), consistent with the measured densities of all samples, which is more than 97% of theoretical density. The high resolution TEM image in Fig. 5.3.3d shows the clean grain boundary, which also facilitates the charge transport.

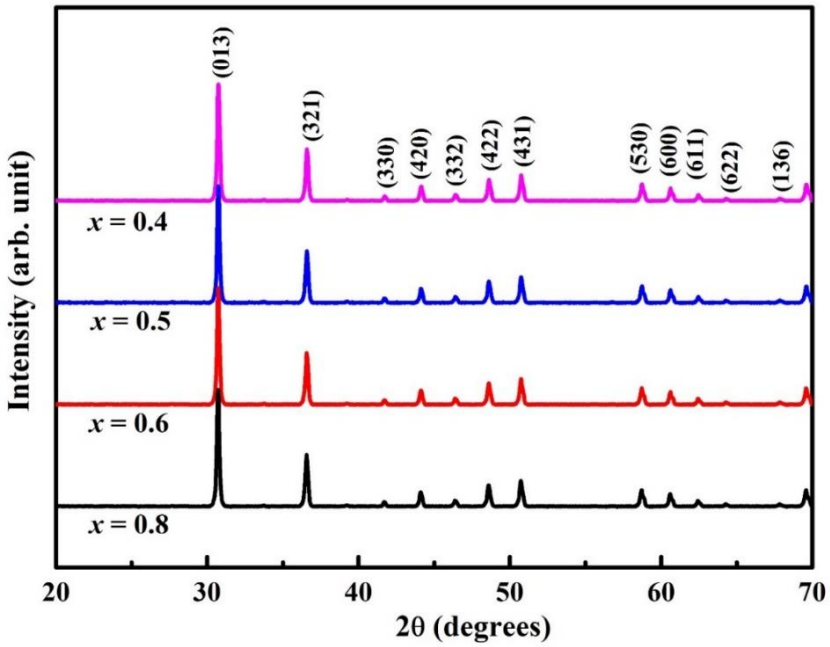

Fig. 5.3.1 XRD spectra of $La_{0.68}Ce_{0.22}Fe_{4-x}Co_xSb_{12}$ (x=0.4, 0.5, 0.6, and 0.8). All peaks can be indexed, indicating pure skutterudites phase.

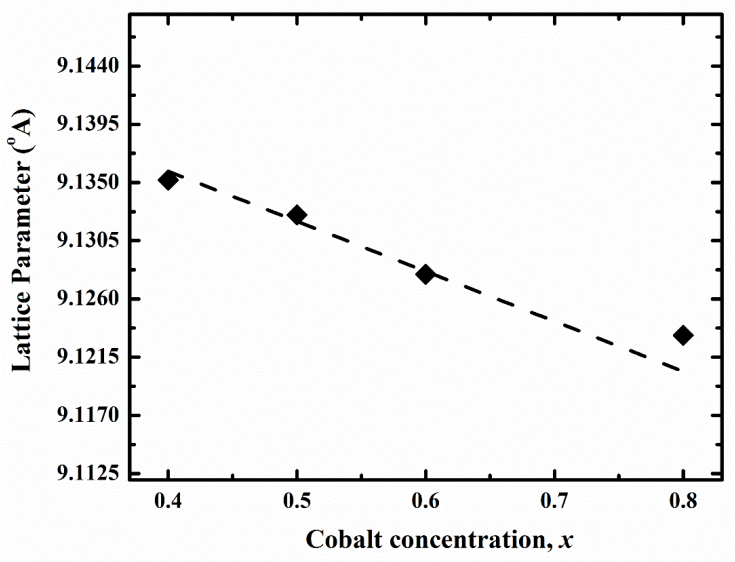

Fig. 5.3.2 Lattice parameter of $La_{0.68}Ce_{0.22}Fe_{4-x}Co_xSb_{12}$ (x=0.4, 0.5, 0.6, and 0.8) as a function of cobalt concentration. Lattice parameter decreases with increasing cobalt concentration.

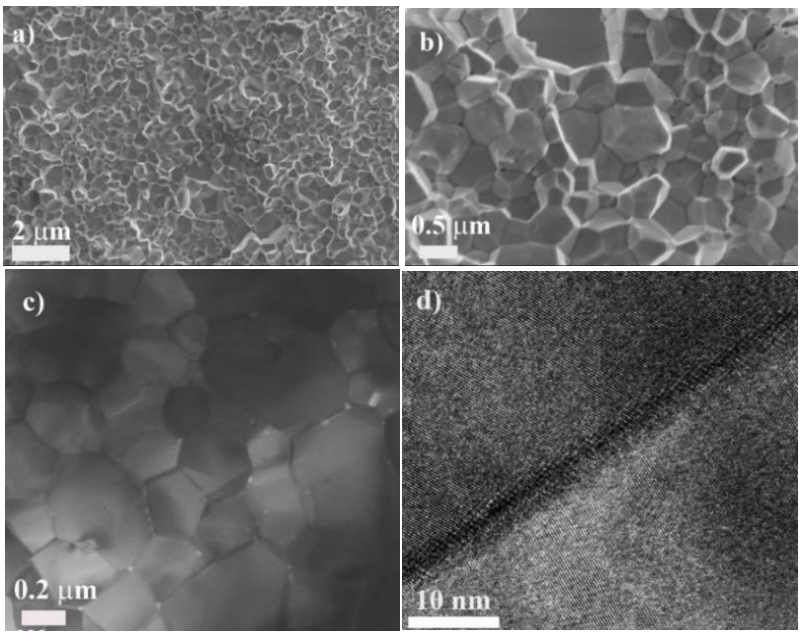

Fig. 5.3.3 SEM images at a) low and b) high magnification and TEM images at a) low and b) high magnification of $La_{0.68}Ce_{0.22}Fe_{3.5}Co_{0.5}Sb_{12}$ showing grain size, crystallinity, and grain boundary.

The room temperature carrier concentration and the mobility of the charge carriers as a function of cobalt concentration *x* is plotted in Fig. 5.3.4. The carrier concentration decreases with increasing cobalt concentration and ranges from 4.87×10^{21} cm^{-3} for $x = 0.4$ to 2.35×10^{21} cm^{-3} for $x = 0.8$. Higher cobalt content gives more electrons to the host system and effectively lowers the hole concentration, consistent with the experimental observation. The room temperature mobility of the charge carrier ranges from ~2.28 cm^2 V^{-1} S^{-1} for $x = 0.4$ to ~2.82 cm^2 V^{-1} S^{-1} for $x = 0.8$.

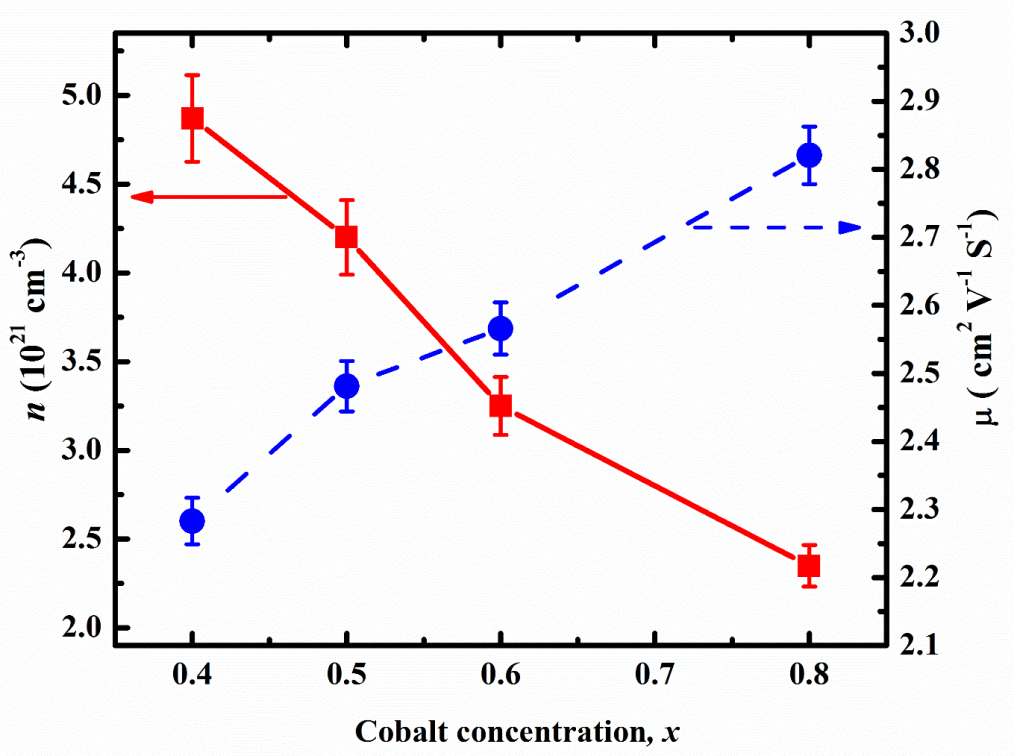

Fig. 5.3.4 Carrier concentration and mobility of $La_{0.68}Ce_{0.22}Fe_{4-x}Co_xSb_{12}$ as a function of cobalt concentration, *x*. Carrier concentration decreases while mobility increases with increasing cobalt concentration.

The temperature dependence of the electrical conductivity is shown in Fig. 5.3.5a. The electrical conductivity of all samples decreases with increasing temperature, implying that the samples are heavily doped semi-conductors. Since the concentration of La and Ce is kept fixed, the electrical conductivity of the samples mainly depends on the Fe/Co ratio. With higher cobalt content, the electrical conductivity of a sample decreases, which is due to reduced carrier concentration [Fig. 5.3.4]. However, for the fixed amount of fillers and Fe/Co ratio, the observed electrical conductivity is higher than the calculated electrical conductivity based on a simple electrons counting method. Generally La and Ce are in +3

state. The observed higher electrical conductivity compared with the calculated one indicates that there is not a complete transfer of electrons from the outer orbits of La and Ce to the host system. The estimation of charge state obtained by integrating the electronic density of filler(s) state up to Fermi level indicates that the charge state of La and Ce is less than +3 [11], which explains why observed electrical conductivity is higher when compared with the calculated one.

The temperature-dependent Seebeck coefficient is shown in Fig. 5.3.5b. The Seebeck coefficient of all samples is positive, indicating hole is the majority charge carrier. The Seebeck coefficient of degenerate semi-conductor or metal depends on carrier concentration (n) as $n^{-2/3}$ [4], sample with higher carrier density gives lower Seebeck coefficient, consistent with experimental observation. For the sample with x = 0.4, 0.5, and 0.6, the Seebeck coefficient increases from room temperature to about 525 ^{o}C. However, for the sample with x = 0.8, the Seebeck coefficient increases to about 500 ^{o}C and then decreases, an indication of the starting of bipolar effect with higher cobalt concentration. The Seebeck coefficient of such a mixed semi-conductor can be expressed as [12]

$$S = \frac{S_e \sigma_e + S_h \sigma_h}{\sigma_e + \sigma_h} \qquad (5.3.1)$$

where σ_e and σ_h are the conductivities from electrons and holes, respectively, S_e and S_h are the Seebeck coefficient from electrons and hole, respectively. At higher temperatures, both the electrons and holes move across the band gap, resulting in decreased Seebeck coefficient owing to the opposite effect of two types of carriers. From the temperature-dependent Seebeck coefficient measurement, the band gap (E_g) of various compositions

can be roughly estimated using the equation $E_g = 2eS_{max}T_{max}$, where *e* is the elementary charge, S_{max} is the peak Seebeck coefficient, and T_{max} is the temperature corresponding to the maximum Seebeck coefficient [5]. Based on this equation, the band gaps of the samples were estimated to be in the range of 0.27-0.31 eV, consistent with literature value [13].

The temperature-dependent power factor (*PF*) is shown in Fig. 5.3.5c. The power factor of all samples increases with temperature and attains a maximum value at around 450 ^{o}C and then decreases with temperature except for the sample with x = 0.4. The decrease in *PF* with temperature is due to the bipolar effect, consistent with the Seebeck effect observation. A maximum *PF* of ~35 μW cm^{-1} K^{-2} at around 450 ^{o}C is achieved in $La_{0.68}Ce_{0.22}Fe_{3.5}Co_{0.5}Sb_{12}$, which is comparable to some of the results reported previously [14, 15].

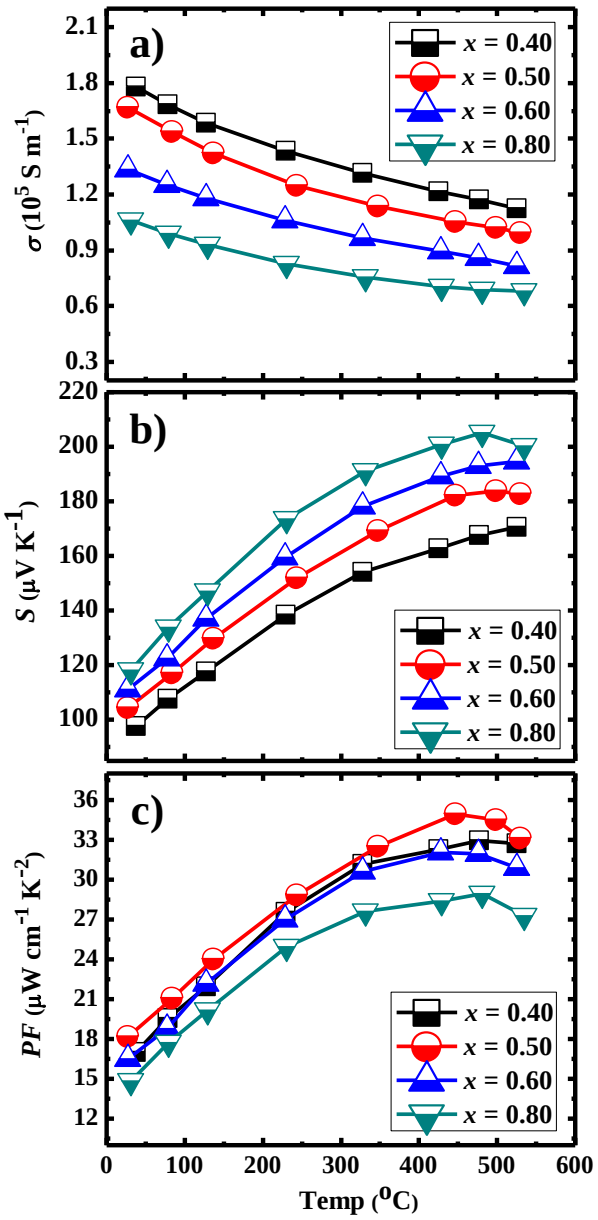

Fig. 5.3.5 Temperature-dependent a) electrical conductivity, b) Seebeck coefficient, and c) power factor of $La_{0.68}Ce_{0.22}Fe_{4-x}Co_xSb_{12}$ (x=0.4, 0.5, 0.6, and 0.80).

The temperature-dependent total thermal conductivity is shown in Fig. 5.3.6a. The thermal conductivity of all samples first decreases up to ~325 ^{o}C and then increases with temperature, a well-known bipolar effect. However, the rise in thermal conductivity is faster for the sample with x = 0.8, an indication of stronger bipolar effect. For the sample with x = 0.6, 0.5, and 0.4, the rise in thermal conductivity is not as sharp as with the sample x = 0.8, which may be due to less excited electrons compared with x = 0.8 sample. Assuming that the contribution of minority charge carriers at high temperature is small, the total thermal conductivity can be written as the sum of the thermal contribution from the carriers and from the lattice vibration. The carrier contribution to the total thermal conductivity can be calculated using the Wiedemann-Franz relation given by $\kappa_e = \sigma LT$, where σ is the electrical conductivity, L is the Lorenz number, and T is the absolute temperature. Within the degenerate approximation, the Lorenz number can be obtained using the equation [6],

$$L = \left(\frac{k_B}{e}\right)^2 \left[\frac{3F_0(\eta)F_2(\eta) - 4F_1^2(\eta)}{F_0^2(\eta)}\right] \qquad (5.3.2)$$

with the Fermi integral $F_j(\eta)$ defined as

$$F_j(\eta) = \int_0^\infty \frac{\xi^j d\xi}{1 + \exp(\xi - \eta)} \qquad (5.3.3)$$

where ξ is the reduced carrier energy and $\eta = E_F/k_BT$ is the reduced electrochemical potential. The reduced electrochemical energy can be calculated from the Seebeck coefficient S as well as the scattering parameter r, given as

$$S = \pm\frac{\kappa_B}{e}\frac{\left(r+\frac{5}{2}\right)F_{r+\frac{3}{2}}(\eta)}{\left(r+\frac{3}{2}\right)F_{r+\frac{1}{2}}(\eta)} - \eta \qquad (5.3.4)$$

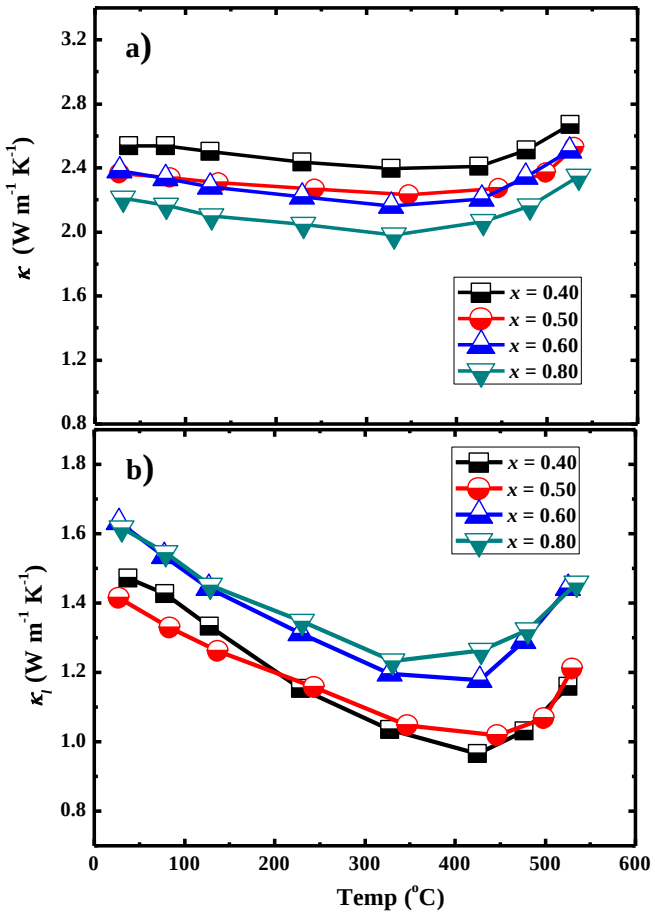

Fig. 5.3.6 Temperature-dependent a) total thermal conductivity and b) lattice thermal conductivity of $La_{0.68}Ce_{0.22}Fe_{4-x}Co_xSb_{12}$ (x=0.4, 0.5, 0.6, and 0.8).

Assuming that the acoustic phonon scattering is the dominant mechanism for carrier scattering, we have calculated the temperature-dependent Lorenz number from the reduced Fermi energy deduced from the Seebeck coefficient at room temperature based on a single parabolic band model [17]. The lattice part of thermal conductivity can be enumerated by subtracting the carrier contribution from the total thermal conductivity. The temperature-dependent lattice thermal conductivity is plotted in Fig. 5.3.6b.

In the Debye model, κ_l is expressed as [18, 19]:

$$\kappa_l = \frac{\kappa_B}{2\pi^2 \upsilon}\left(\frac{\kappa_B T}{\hbar}\right)^3 \int_0^{\theta_D/T} \frac{x^4 e^x}{\tau^{-1}(e^x - 1)^2}\, dx \qquad (5.3.5)$$

where $x = \frac{\hbar\,\omega}{\kappa_B T}$ is the dimensionless quantity, κ_B is the Boltzmann constant, ω is the phonon frequency, $\hbar$ is the reduced Planck constant, θ_D is the Debye temperature, υ is the velocity of sound, and τ is the phonon-scattering relaxation time. For double-filled skutterudites, the phonon-scattering relaxation time is given by,

$$\tau^{-1} = \frac{\upsilon}{l} + A\omega^4 + B\omega^2 \exp\left(-\frac{\theta_D}{3T}\right) + \frac{C_1 \omega^2}{(\omega_1^2 - \omega^2)^2} + \frac{C_2 \omega^2}{(\omega_2^2 - \omega^2)^2} \qquad (5.3.6)$$

where l is the grain size, A and B are the parameters which refer to the point defect scattering term and phonon-phonon Umklapp scattering term, C_1 and C_2 are the parameters related with the phonon resonant scattering term for different fillers, and ω_1 and ω_2 are the resonant frequencies of first and second filler, respectively. The terms in the right hand side of Eq. [5.3.6] represent grain boundary, point defect, phonon-phonon Umklapp, and phonon resonance scattering, respectively. The phonon-scattering probability is directly

related with the inverse of phonon-relaxation time. Compared with single-filled skutterudites, double-filled skutterudites brings an additional term in phonon relaxation time, which further reduces the lattice thermal conductivity κ_l. For double-filled skutterudites, the additional phonon scattering also comes from point defect scattering [20]. In the experiment, the total filling fraction of fillers is close to 100%, the point defects mainly comes from the mass fluctuation of the two fillers. Since the difference in atomic mass of La and Ce is very small, we cannot expect a significant reduction in lattice thermal conductivity via point defect scattering. Since La and Ce have similar vibrational frequencies [10], the scattering of phonons with different mean free paths is not significant. So, the reduction of lattice thermal conductivity in the system studied may be due to the phonon scattering off the grain boundaries. Among the four samples studied, the lattice thermal conductivity of the samples with x = 0.4 and 0.5 is almost the same in the entire temperature range and varies from ~1.4 W m^{-1} K^{-1} at room temperature to ~1.2 W m^{-1} K^{-1} at 535 ^{o}C.

From the measured value of temperature-dependent electrical conductivity, the Seebeck coefficient, and thermal conductivity, the temperature-dependent dimensionless figure-of-merit, *ZT*, calculated and is plotted in Fig. 5.3.7. The *ZT* values of all samples increase with temperature up to about 500 ^{o}C and then decrease. A peak *ZT* in excess of 1.1 at 500 ^{o}C is achieved in $La_{0.68}Ce_{0.22}Fe_{3.5}Co_{0.5}Sb_{12}$, comparable with the best reported *ZT*s [14, 15].

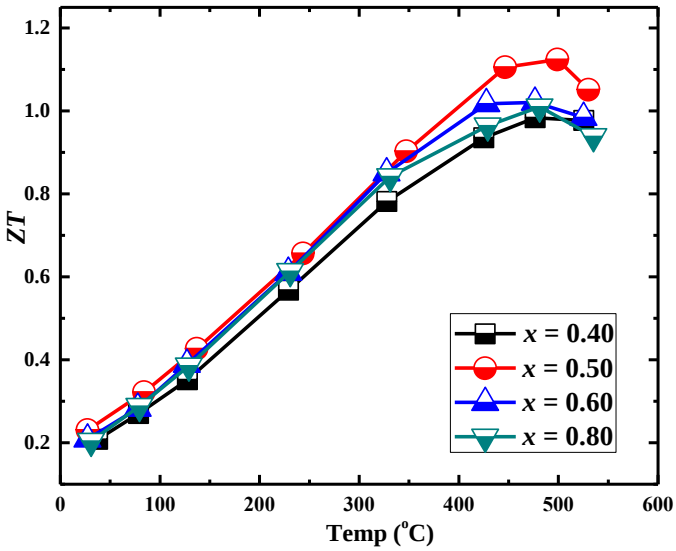

Fig. 5.3.7 Temperature-dependent dimensionless figure-of-merit, *ZT* of $La_{0.68}Ce_{0.22}Fe_{4-x}Co_xSb_{12}$ (x = 0.4, 0.5, 0.6, and 0.8).

Based on the temperature-dependent TE properties measurement, the generated output power and its conversion efficiency were predicted. The conventional formula for the maximum efficiency is given as,

$$\eta_{max} = \left(1 - \frac{T_c}{T_h}\right) \frac{\sqrt{1 + ZT_{av}} - 1}{\sqrt{1 + ZT_{av}} + {T_c}/{T_h}} \qquad (5.3.7)$$

where T_h, T_c, and T_{av} are the hot side, cold side and their average temperature, respectively. This estimates the maximum efficiency from the assumption of the temperature independence of TE properties as well as a lumped estimate of Joule heating on the hot and cold side, which gives rise to misleading of the temperature profile in a length direction through a TE leg. This analytical calculation leads to over/under-estimation of TE performance. For a precise prediction of output power and efficiency, a numerically

iterative method is necessary to take TE properties as a function of temperature into account. The 1-D heat flow of a differential element is governed by [21],

$$\frac{d}{dx}\left(\kappa(x)\frac{dT(x)}{dx}\right)+J^2\rho(x)-J\tau(x)\frac{dT(x)}{dx}=0 \qquad (5.3.8)$$

where J is the current density, and $\tau(x)$ is the Thomson coefficient defined as $T\frac{dS(x)}{dx}$ in which x is a position in a length direction.

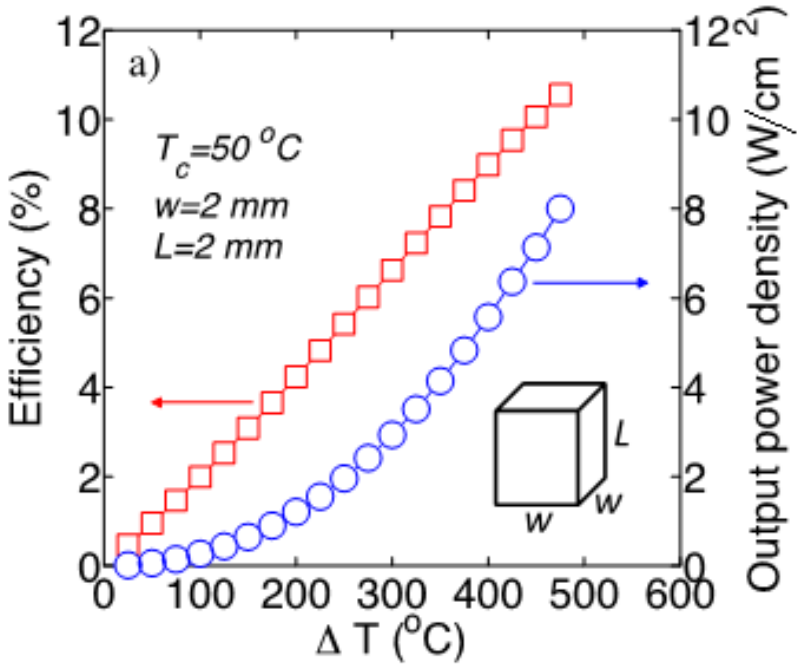

Fig. 5.3.8a Efficiency and output power density of $La_{0.68}Ce_{0.22}Fe_{3.5}Co_{0.5}Sb_{12}$ as a function of temperature difference between source and sink. The sink temperature is fixed at 50 °C.

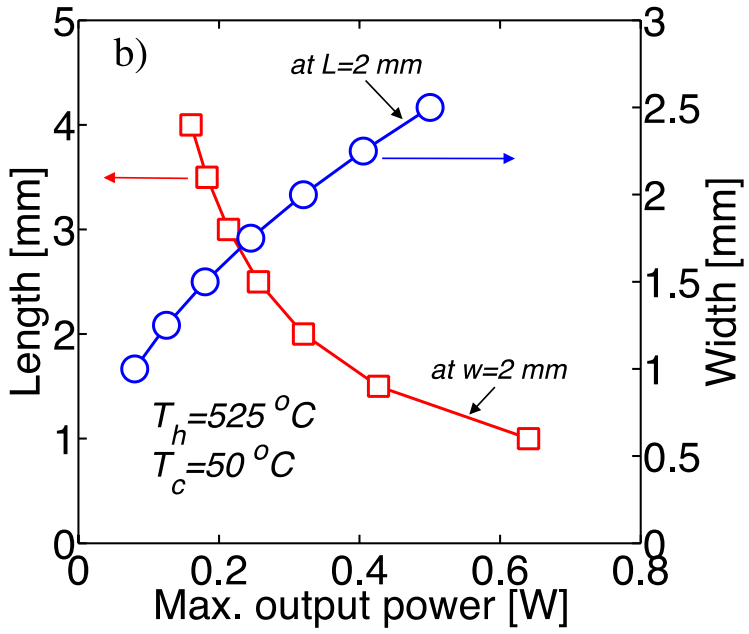

Fig. 5.3.8b Output power density as a function of length and width of bar sample.

By using a finite difference method, a temperature profile and its corresponding current density at a given temperature difference (ΔT) are obtained by iterative repetition until convergence criteria are met. Fig. 5.3.8a shows the output power and efficiency based on the numerical analysis at which T_c was kept as 50 ^{o}C, and T_h was increased up to 525 ^{o}C. The output power density of the size in 2x2x2 mm^3 increases parabolically with ΔT increasing and reaches 8 W cm^{-2} at ΔT=475 ^{o}C, and its corresponding conversion efficiency is 10.5 %(Fig. 5.3.8a). Since the output power is geometry dependent, the maximum output power according to various length and width of a leg is shown in Fig. 5.3.8b, where T_h=525 ^{o}C and T_c=50 ^{o}C. At a fixed width, the output power decreases at a longer leg since the electric resistance increases while a leg with larger cross-section area generates more electric power at a fixed length. It is noted that this trend is valid under a constant ΔT, i.e.

a required input heat from a heat source can be provided to keep ΔT a constant. Even though one requires more realistic analysis to design a practical TE generator, the performance prediction in an ideal constraint enables effective access to a selection of proper TE material beyond *ZT* value.

5.4 Thermoelectric Properties of $Ce_xNd_xFe_{3.7}Ni_{0.3}Sb_{12}$ (x = 0.35, 0.40, 0.45, and 0.50)

As discussed earlier, *p*-type skutterudites material shows strong bipolar effect at a higher temperature. So, a careful tuning of the Fe/Co ratio and filler(s) together with optimized amount of filler(s) is required to improve the TE performance of *p*-type skutterudites. Keeping in mind that in most of the solids, phonons with low vibrational frequencies contribute most to the heat conduction, scattering off those phonons is desired to minimize the thermal conductivity. The calculation shows that the vibrational frequencies of various fillers in (111) direction of Fe-based p-type skutterudites RFe_4Sb_{12} and RFe_3CoSb_{12} does not vary significantly for different Fe/Co ratio [10]. Based on the calculated vibrational frequencies [10] and considering the fact that most of the heat carrying phonons have lower vibrational frequencies, we have synthesized Ce/Nd-filled *p*-type skutterudites and their thermoelectric properties were examined.

Most of the work in *p*-type skutterudites involves the partial replacement of Fe by Co for charge compensation. Since Ni has one more electron compared to Co, a lower power factor and strong bipolar conduction in thermal conductivity is expected at higher temperature. However, we have demonstrated that by suitably tuning Fe/Ni ratio together

with fillers concentration, we can achieve both high power factor and low thermal conductivity, leading to an improved *ZT* value. In this experiment, we first fixed the rattler concentration and tuned Fe/Ni ratio to improve the TE properties. Based on this experiment, we chose the best Fe/Ni ratio that gave the highest *ZT* and tuned rattler concentration to further improve the TE performance.

Pure elements are weighted according to the stoichiometry of $Ce_xNd_xFe_{3.7}Ni_{0.3}Sb_{12}$ (x = 0.35, 0.40, 0.45, and 0.50) in a carbon-coated quartz tube under a low pressure and kept in furnace to melt them at about 1050 ^oC. The tubes were quenched in water and annealed the ingots at 650 ^oC for 5 days to ensure the pure skutterudites phase. The ingots were then cleaned and crushed into fine powder using mortar and pestle under argon protection, loaded into a graphite die and hot pressed at 650 ^oC under 80 MPa for 5 minutes.

Fig. 5.4.1 shows the XRD patterns of four compositions studied. The XRD patterns of the hot pressed samples show pure skutterudites phase without any impurity phase for x = 0.35, 0.40, and 0.45 indicating that the structure is flexible to accommodate different amount of rattlers. However, we observed impurity phase for the sample with x = 0.5.

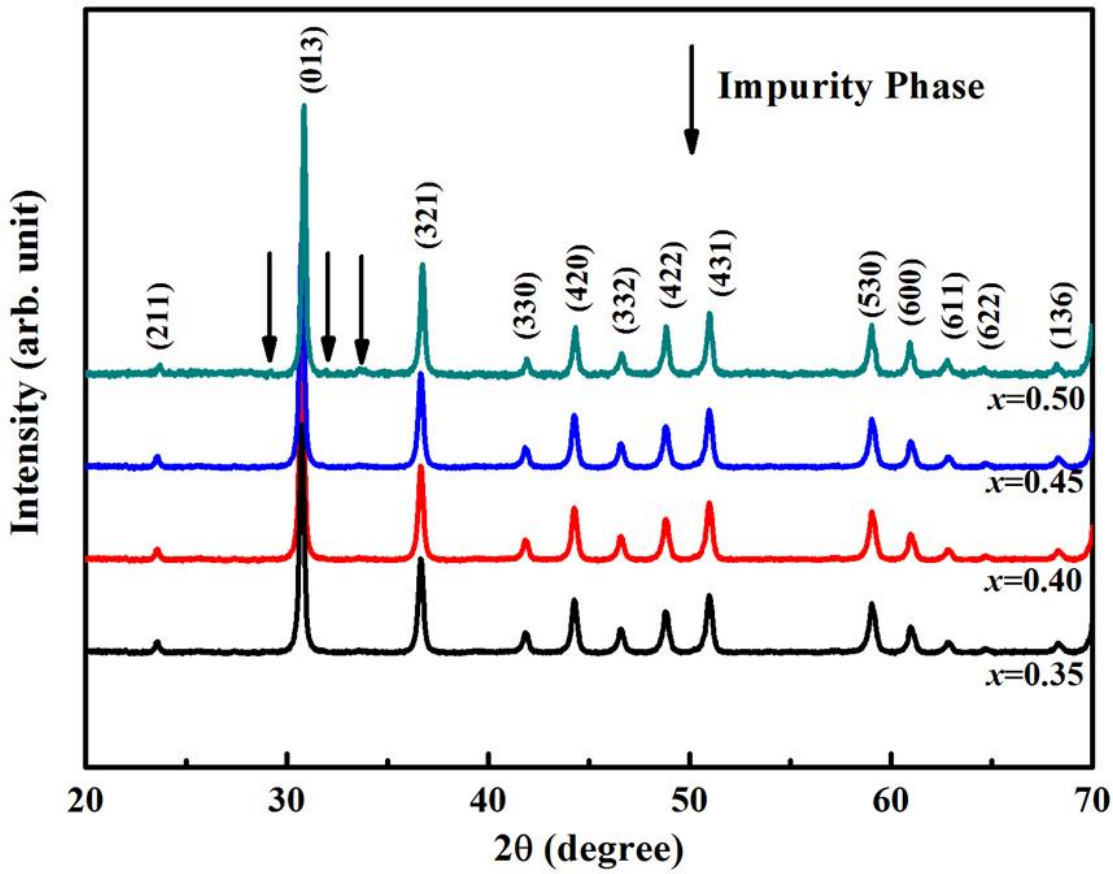

Fig. 5.4.1 XRD spectra of $Ce_xNd_xFe_{3.7}Ni_{0.3}Sb_{12}$ (x = 0.35, 0.40, 0.45, and 0.50). The sample composition with x = 0.50 shows the presence of impurity phase.

Fig. 5.4.2 shows the SEM image at low (Fig. 5.4.2a) and high (Fig. 5.4.2b) magnification of the freshly broken surface of the hot pressed samples. From the SEM images, we have observed that the majority of the grains are of micron size and only a few grains are of nano-scale size. With the bigger grains, we have few interfaces for phonon scattering. But, the non-uniform distribution of grain size can help scatter phonons with different mean free paths [22] even though it may not be as effective as what was shown in reference [22]. The

SEM image shows that the crystallized grains are closed packed, an indication of high volume mass density. The measured densities of 7.72, 7.70, 7.78, and 7.82 g cm^{-3} for x = 0.35, 0.40, 0.45, and 0.5, respectively of the sample are more than 97% of the theoretical density, which is consistent with close packing shown in the SEM images. The high resolution TEM image in Fig. 2c shows that the grain boundaries are clean and the orientations are of large angles, which also helps phonon scattering.

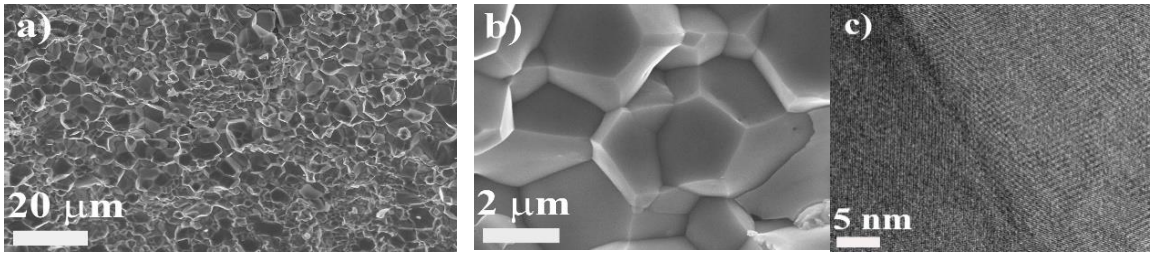

Fig. 5.4.2 SEM images a) low and b) high magnification and c) TEM image at high magnification of $Ce_{0.40}Nd_{0.40}Fe_{3.7}Ni_{0.3}Sb_{12}$ showing grain size and the a clean grain boundary.

Table 1 shows the compositions studied, their actual compositions, and various properties at room temperature.

Nominal composition	Actual composition	ρ	σ	S	κ	ZT
		(g cm^{-3})	(10^{5} S m^{-1})	(μV K^{-1})	(W m^{-1} K^{-1})	
$Ce_{0.35}Nd_{0.35}Fe_{3.7}Ni_{0.3}Sb_{12}$	$Ce_{0.33}Nd_{0.29}Fe_{3.77}Ni_{0.29}Sb_{11.84}$	7.72	1.97	97	2.28	0.25
$Ce_{0.40}Nd_{0.40}Fe_{3.7}Ni_{0.3}Sb_{12}$	$Ce_{0.38}Ce_{0.37}Fe_{3.78}Ni_{0.27}Sb_{11.68}$	7.70	1.76	103	2.10	0.27
$Ce_{0.45}Nd_{0.45}Fe_{3.7}Ni_{0.3}Sb_{12}$	$Ce_{0.40}Nd_{0.36}Fe_{3.72}Ni_{0.32}Sb_{11.88}$	7.78	1.53	100	2.25	0.21
$Ce_{0.50}Nd_{0.50}Fe_{3.7}Ni_{0.3}Sb_{12}$	$Ce_{0.43}Nd_{0.41}Fe_{3.74}Ni_{0.28}Sb_{11.72}$	7.82	1.37	104	2.34	0.19

Table 5.4.1 Room temperature physical properties of $Ce_xNd_xFe_{3.7}Ni_{0.3}Sb_{12}$ (x = 0.35, 0.40, 0.45, and 0.5) including their nominal and actual compositions, density, electrical conductivity, Seebeck coefficient, thermal conductivity, and dimensionless figure-of-merit, *ZT*.

Fig. 5.4.3a shows the temperature-dependent electrical conductivity of samples. The electrical conductivity of all samples decrease with temperature, showing that all samples are heavily doped semi-conductors. We also observed that the electrical conductivity of the samples with higher rattler concentration is lower. In the experiments we have kept the Fe to Ni ratio fixed, the electrical conductivity of the samples depends on the rattler concentration. Higher Ce and Nd contents give more electrons to skutterudites structure, effectively reducing the hole concentration which, in turn, reduces the electrical conductivity, which is consistent with the observed electrical conductivity.

The temperature-dependent Seebeck coefficient is shown in Fig. 5.4.3b. The Seebeck coefficient of all samples is positive, implying that the dominant charge carriers are holes. For a given temperature difference, high Seebeck voltage is required to convert a significant fraction of heat into useful electricity. We have achieved a high Seebeck voltage of ~173 μV K^{-1} at around 535 ºC in $Ce_{0.40}Nd_{0.40}Fe_{3.7}Ni_{0.3}Sb_{12}$, the composition with the highest ZT in this experiment. From the temperature-dependent Seebeck coefficient measurement, the band gap (E_g) of various compositions can be roughly estimated using the equation $E_g = 2eS_{max}T_{max}$, where e is the elementary charge, S_{max} is the peak Seebeck coefficient, and T_{max} is the maximum temperature corresponding to the maximum Seebeck coefficient [5]. Based on this equation, the band gaps of samples were estimated to be in the range of 0.25-0.29 eV, consistent with literature value [13].

The temperature-dependent power factor is shown in Fig. 5.4.3c. The power factor, *PF*, of all samples increases with temperature and attains a maximum value at around 530 ºC. A maximum power factor of ~35 μW cm^{-1} K^{-2} at around 535 ºC is achieved in $Ce_{0.4}Nd_{0.4}Fe_{3.7}Ni_{0.3}Sb_{12}$, and is comparable to some of the *p*-type compositions reported previously [14, 23].

The temperature-dependent thermal conductivity is shown in Fig. 5.4.3d. The thermal diffusivity of the samples as a function of temperature is shown in the inset of Fig. 3d. The total thermal conductivity for $Ce_xNd_xFe_{3.7}Ni_{0.3}Sb_{12}$ with x = 0.40, 0.45, and 0.50 is lower than that of $Ce_{0.35}Nd_{0.35}Fe_{3.7}Ni_{0.3}Sb_{12}$. For $Ce_{0.35}Nd_{0.35}Fe_{3.7}Ni_{0.3}Sb_{12}$, the total thermal conductivity increases with temperature. This may be due to increased carrier contribution to the total thermal conductivity and at the same time fewer rattlers will result in higher

lattice thermal conductivity. For all of the samples, we observed an upturn in thermal conductivity after 325 ^{o}C. The observed upturn in thermal conductivity at higher temperature is due to the excitation of both electrons and holes across the gap, a well-known bipolar effect. Assuming that the contribution of minority charge carriers at high temperature is small, the total thermal conductivity can be written as the sum of the thermal contribution from the carriers and from the lattice vibration. The carrier contribution to the total thermal conductivity can be calculated using Wiedemann-Franz relation given by $\kappa_e = \sigma LT$, where σ is the electrical conductivity, L is the Lorenz number, and T is the absolute temperature. The Lorenz number can be calculated as [24],

$$L = \left(\frac{\kappa_B}{e}\right)^2 \left[\frac{\left(r+\frac{7}{2}\right)F_{r+\frac{5}{2}}(\xi)}{\left(r+\frac{3}{2}\right)F_{r+\frac{1}{2}}(\xi)} - \left(\frac{\left(r+\frac{5}{2}\right)F_{r+\frac{3}{2}}(\xi)}{\left(r+\frac{3}{2}\right)F_{r+\frac{1}{2}}(\xi)}\right)^2\right] \tag{5.4.1}$$

where r is the scattering parameter, and $F_n(\xi)$ is the Fermi integral given by,

$$F_n(\xi) = \int_0^\infty \frac{y^n}{1+e^{y-\xi}}dx \tag{5.4.2}$$

where ξ is the reduced Fermi energy that can be deduced from the Seebeck coefficient S as well as the scattering parameter r, given as,

$$S = \pm\frac{\kappa_B}{e}\frac{\left(r+\frac{5}{2}\right)F_{r+\frac{3}{2}}(\xi)}{\left(r+\frac{3}{2}\right)F_{r+\frac{1}{2}}(\xi)} - \xi \tag{5.4.3}$$

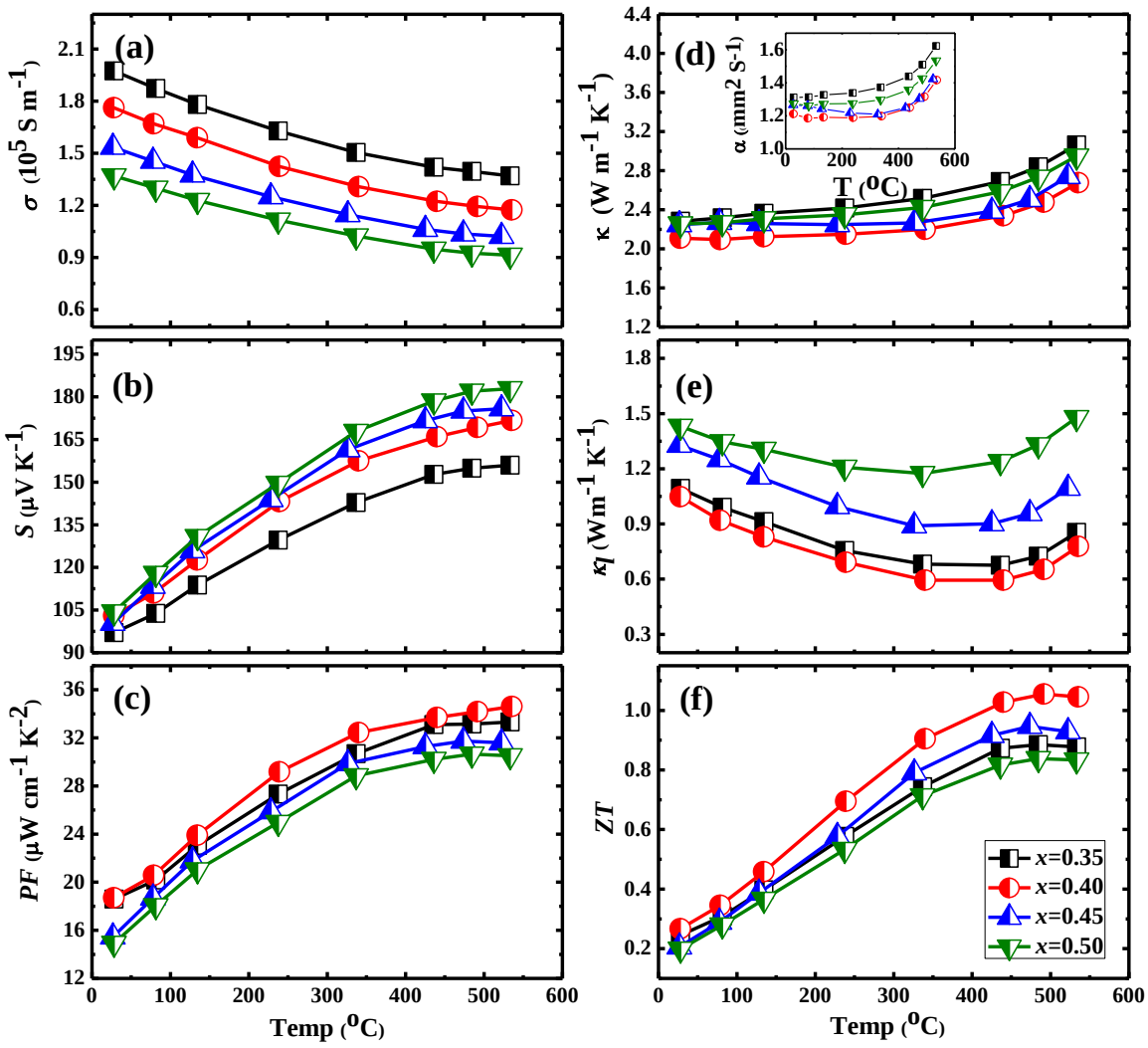

Fig. 5.4.3 Temperature-dependent thermoelectric properties of $Ce_xNd_xFe_{3.7}Ni_{0.3}Sb_{12}$ with *x*=0.35, 0.40, 0.45, and 0.50: a) electrical conductivity, b) Seebeck coefficient, c) power factor, d) thermal conductivity, e) lattice thermal conductivity, and f) *ZT*.

In this calculation, we assumed that the acoustic phonon scattering is the dominant mechanism for carrier scattering and evaluated the temperature-dependent Lorenz number

from the reduced Fermi energy deduced from the Seebeck coefficient at room temperature based on single parabolic band model [17]. The lattice part of thermal conductivity can be inferred by subtracting the carrier contribution from the total thermal conductivity. The temperature-dependent lattice thermal conductivity is shown in Fig. 5.4.3e. κ_l for most of the samples decreases with temperature and attains a minimum value at around 475 ^{o}C and then increases. For $Ce_{0.5}Nd_{0.5}Fe_{3.7}Ni_{0.3}Sb_{12}$, we observed an upturn in lattice thermal conductivity after 425 ^{o}C. The lattice thermal conductivity of the sample with x = 0.35 is higher than that of sample with x = 0.40, which can be attributed to the weaker rattling effect due to lower rattler concentration. For the sample with x = 0.45 and 0.50, the lattice thermal conductivity is higher than the sample with x = 0.35 and 0.40, possibly due to weaker rattling effect because of higher Ce and Nd concentration above the solubility limit [24, 25]. Among the four samples measured, the lattice thermal conductivity of $Ce_{0.4}Nd_{0.4}Fe_{3.7}Ni_{0.3}Sb_{12}$ is the lowest and varies from ~1.05 W m^{-1} K^{-1} at room temperature to ~0.8 W m^{-1} K^{-1} at 535 ^{o}C.

The temperature-dependent *ZT* is calculated from the measured value of temperature-dependent electrical conductivity (σ), the Seebeck coefficient (S), and the thermal conductivity (κ) and are plotted in Fig. 5.4.3f. The *ZT* value of all samples increases with temperature, attain a maximum value at around 475 ^{o}C, and then decreases. The peak *ZT* of ~1.1 at 475 ^{o}C in $Ce_{0.4}Nd_{0.4}Fe_{3.7}Ni_{0.3}Sb_{12}$ is comparable to the highest reported *ZT* of *p*-type skutterudites.

5.5 Summary

In summary, we have synthesized the La/Ce double-filled and misch metal ($La_{0.25}Ce_{0.5}Pr_{0.05}Nd_{0.15}Fe_{0.03}$) *p*-type skutterudites by melting-quenching-annealing-ball-milling-dc hot pressing the nano-powder at 650 ^{o}C at a pressure of 80 MPa for 5 minutes. The Ce/Nd double-filled sample are made by hot pressing the hand-ground powder made from annealed ingot under the same temperature, pressure, and holding time as mentioned above. The XRD spectra of La/Ce double-filled samples show pure skutterudites phase while we observed minority phase in misch metal-filled sample ($Mm_{0.9}Fe_{4-x}Co_xSb_{12}$, x=0.7, 0.8, 0.9, and 1.0) with x=0.7 and Ce/Nd double-filled skutterudites $Ce_xNd_xFe_{3.7}Ni_{0.3}Sb_{12}$ (x=0.35, 0.40, 0.45, and 0.50) with x=0.5. We achieved a high power factor ~35 μW cm^{-1} K^{-2} in $La_{0.68}Ce_{0.22}Fe_{3.5}Co_{0.5}Sb_{12}$ and $Ce_{0.4}Nd_{0.4}Fe_{3.7}Ni_{0.3}Sb_{12}$. However, the thermal conductivity of $La_{0.68}Ce_{0.22}Fe_{3.5}Co_{0.5}Sb_{12}$ varies in a narrow range (~2.4 W m^{-1} K^{-1} at room temperature to ~2.5 W m^{-1} K^{-1} at 535 ^{o}C) compared to the thermal conductivity (~2.1 W m^{-1} K^{-1} at room temperature to ~2.6 W m^{-1} K^{-1} at 535 ^{o}C) of $Ce_{0.4}Nd_{0.4}Fe_{3.7}Ni_{0.3}Sb_{12}$. Since the *ZT* of both samples are similar while the thermal conductivity is higher in La/Ce double-filled skutterudites, we can expect high output power density. However, the amount of fillers in Ce/Nd double-filled sample is less than that of La/Ce double-filled sample and Ni is cheaper than cobalt, using Ce/Nd double-filled sample could be price effective while considered the practical application. The power factor (~30 W m^{-1} K^{-2} at 425 ^{o}C) and thermal conductivity (~1.8 W m^{-1} K^{-1} at room temperature to ~2.3W m^{-1} K^{-1} at 535 ^{o}C) of misch metal-filled $Mm_{0.9}Fe_{3.1}Co_{0.9}Sb_{12}$ is lower than La/Ce and Ce/Nd double-filled *p*-type skutterudites. The peak ZT ~1.1 at 425 ^{o}C in $Mm_{0.9}Fe_{3.1}Co_{0.9}Sb_{12}$ is similar to the *ZT* of

other two samples. However, the shift of peak *ZT* towards lower temperature increases the average *ZT* of material, which could potentially increase the device efficiency.

5.6 References

1. Bourgoin *et al., J. Alloys and Compds*. **2005**, 399, 47.
2. Zhang *et al., J. Alloys and Compds.* **2009,** 481, 106.
3. Poudel *et al., Science* **2008**, 320**,** 634.
4. Cutler *et al*., *Phys. Rev.* **1964,** 133**,** A1143.
5. Goldsmith *et al., J. Electron Mat.***1999,** 28, 869.
6. Nolas *et al., Thermal Conductivity of Semi-conductors* **(2004)**, Norwell.
7. Li *et al., Nanotechnology* **2012,** 23, 065703.
8. Keppens *et al., Nature* **1998,** 395, 876.
9. Hermann *et al., Phys. Rev. Lett.* **2003,** 90, 135505.
10. Liu *et al., Intermetallics* **2011,** 19, 1747.
11. Shi *et al., Phys. Rev. B* **2007,** 75, 235208.
12. Nolas G. S., *Thermoelectrics: Basic Principles and New Material Developments*, Ed. Zunger A., New York, Springer, **(2001)**.
13. Goldsmith *et al., J. Electron Mat.***1999,** 28, 869.
14. Jie *et al., Phys. Chem. Chem. Phys.* **2013,** 15, 6809.
15. Dahal *et al., Phys. Chem. Chem. Phys.* **2014,** 16, 18170.
16. Rowe D. M. and Bhandari C. M., *Modern Thermoelectrics*, Reston Publishing, Reston, VA (**1983)**.
17. Liu *et al., Adv. Eng. Mater.* **2011,** 1**,** 577.
18. Callway J., *Phys. Rev* **1959,** 113, 1046.
19. Callway J., *Phys. Rev* **1960,** 120, 1149.

20. Bai *et al.*, *Appl. Phys. Lett.* **2010**, 96, 202102.

21. Shackelford, J. F., Alexander, W., Park, J. S., *Practical Handbook of Material Selection*, CRC Press, Boca Raton, **(1995)**.

22. Biswas *et al., Nature* **2012,** 489**,** 414.

23. Rogl *et al., Acta Materialia* **2013**, **61,** 6778.

24. Morelli *et al., Phys. Rev. B* **1997,** 56, 7376.

25. Kuznetsov *et al., J. Phys.: Condens. Matter* **2003,** 15, 5035.

Chapter 6

Mechanical Properties Testing

6.1 Introduction

The durability of thermoelectric generators mostly depend on the mechanical performance of thermoelectric materials. Since skutterudites materials can be used up to 500 ^{o}C, the material will be exposed to thermal stress that could potentially lower the generators' life time. This requires assessing the mechanical behavior of these materials. Among many mechanical properties, hardness (*H*) and Young's modulus of elasticity (*E*) are the easiest to measure. The former quantity is a measure of load-bearing capacity while the later parameter quantifies the stiffness of bond in a material. Instrumented indention testing (IIT), also known as depth-sensing indentation, continuous-recording indentation, or nano-indentation can be used to determine the mechanical strength of samples. One of the various advantages of this high-resolution instrumentation is continuously monitoring the load and displacement of the indenter while driving in or out from the sample surface [1, 2]. In this chapter, we will briefly discuss the technique to quantify the hardness and the Young's modulus of elasticity, and the experimental result on some of the best *p*-type and *n*-type skutterudites samples.

6.2 Measurement of Hardness and Young's Modulus of Elasticity

While considering the practical application of TE devices, several factors, including thermal stability, and mechanical strength, etc. of the sample, need to be considered besides

higher *ZT* value. The most frequently measured mechanical properties are the hardness and the elastic modulus of the material. Hardness of the material is a measure of how resistive is a material to various kinds of permanent shape changes when a compressive force is applied and is defined as load applied per unit area. The hardness of material measures the machinability and it's resistant to wear [3], while the Young's modulus of elasticity can be used to monitor the level of micro-crack damage that may accumulate during the use of TE materials [4]. The instrumented indentation testing (IIT) or nano-indentation enables simultaneous determination of both the hardness and the Young's modulus of elasticity. The schematic representation of basic components of IIT is shown in Fig. 6.2.1.

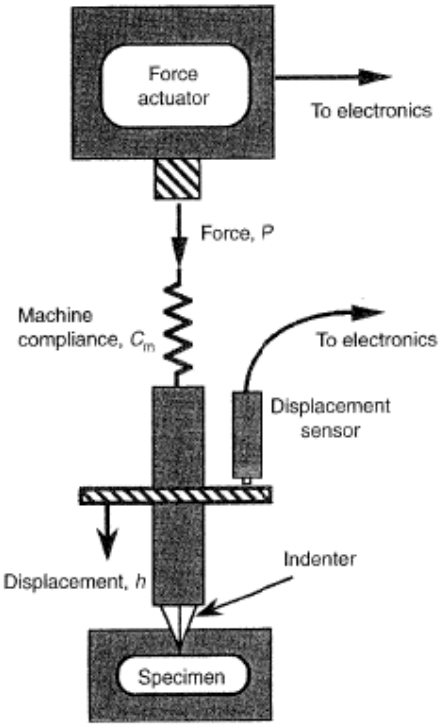

Fig. 6.2.1 Schematic representation of basic components of IIT (Fig taken from Ref.3)

The schematic representation of loading/unloading is shown in Fig. 6.2.2.When the nano-indenter is driven into the sample, the sample undergoes both elastic and plastic deformation. When the indenter is withdrawn, only the elastic part of the displacement gets recovered, allowing it to separate from plastic deformation [5]. The slope (dp/dh) of the upper portion of the unloading curve gives the contact stiffness, *S*.

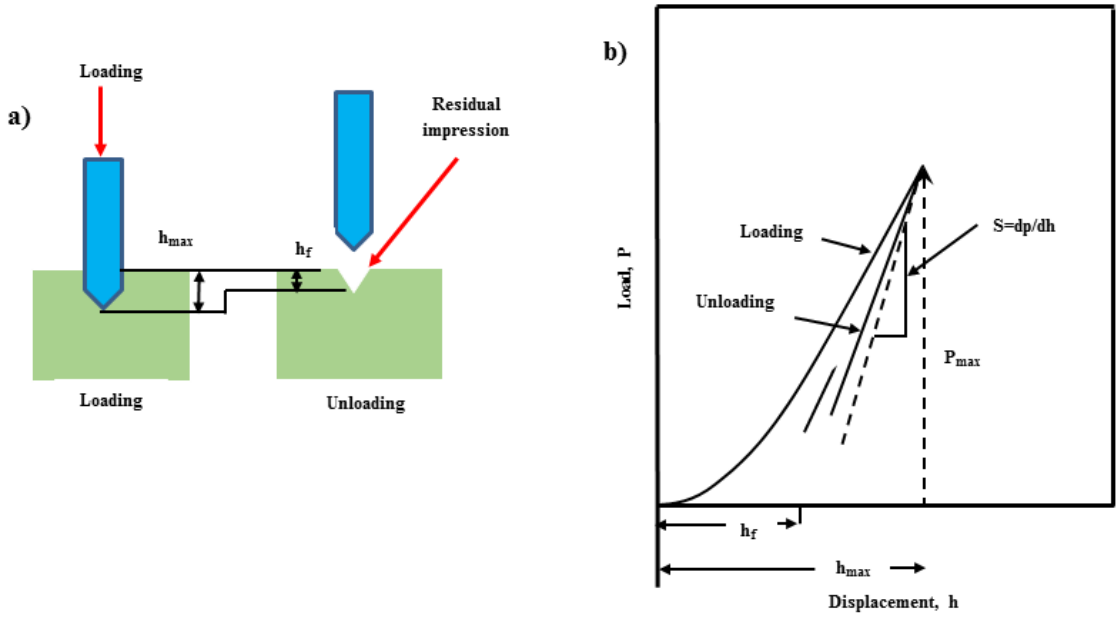

Fig. 6.2.2 Schematic representation of a) loading-unloading of nano-indenter in sample surface and b) load vs. displacement plot.

The hardness (*H*) and the Young's modulus of elasticity (*E*) can be calculated as,

$$H = \frac{P}{A} \qquad (6.2.1)$$

and

$$\frac{1}{E_r} = \frac{1-\upsilon^2}{E} + \frac{1-\upsilon_i^2}{E_i} \qquad (6.2.2)$$

where P is the load, A is the projected contact area at that load, E_r is the reduced elastic modulus, υ is the Poisson's ratio for the test material, and E_i and υ_i are the elastic modulus and Poisson's ratio of indenter, respectively. Diamond (E_i =1141 GPa and υ_i=0.07) is the most frequently used indenter material because its high hardness and elastic modulus minimizes the contribution of the indenter itself to the measured displacement [6]. The reduced elastic modulus (E_r) is given by,

$$E_r = \frac{\sqrt{\pi}}{2\beta}\frac{S}{\sqrt{A}} \qquad (6.2.3)$$

where β is a constant related to the geometric shape of the tip. The Berkovich triangular pyramidal indenter (β =1.034) is preferred over the four-sided Vickers or Knoop indenter because a three-sided pyramid is more easily ground to sharp point [6, 7, 8]. For Berkovich tip, the projected contact area A can be given in terms of indentation depth (h) as,

$$A = 24.56h^2 \qquad (6.2.4)$$

Indenters used in practical nano-indentation testing are not ideally sharp. Therefore, tip geometry calibration or area function calibration is needed. A series of indentation is made on a fused quartz silica at depths of interest. The corrected contact area A can be expressed as,

$$A = 24.56h^2 + C_1h^1 + C_2h^{1/2} + C_3h^{1/4} + \cdots \ldots \ldots + C_8h^{1/128} \qquad (6.2.5)$$

where C_1 through C_8 are constants. The first term in RHS of Eq. 6.2.5 describes the perfect Berkovich indenter, the other terms describes the deviation from Berkovich geometry due to blunting of the tip [8]. Since the measured values of hardness and elastic modulus depends on the indentation depth (h), the error in the measurement of indentation depth has subsequent effect on hardness and modulus value. If the plastic phenomenon is pile-up, then the contact area is larger than predicted by Eq. 6.2.5, both hardness and elastic modulus are overestimated. On the other hand, if the phenomenon is sink-in, the hardness and modulus of elasticity will be underestimated due to the fact that the contact area is smaller than the predicted value. The schematic representation of pile-up and sink-in is as shown in Fig. 6.2.3.

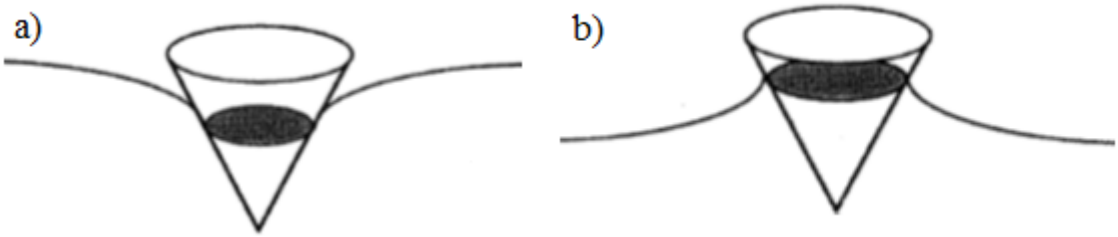

Fig 6.2.3 Schematic representation of a) sink-in and b) pile-up behavior. Fig. taken from Ref. 3.

To examine the extent of pile-up (or sink-in) and establish the true area of contact, the indentation should be imaged, which can be done using different techniques such as light microscopy, scanning electron microscopy (SEM), and atomic force microscopy (AFM) [9].

6.3 Experimental Procedure

The sample for nano-indentation test was made in the following way. The sample was kept it a mold containing the mixture of epoxy and harder (5:1) and let them solidify, which normally takes about 8-10 hours. The sample was then manually polished in progressively finer silicon carbide paper (with grit number 120 through 2500), followed by a diamond suspension polishing with an initial diamond particle size about 3 μm through 0.1 μm using rotating disk. To ensure that the sample surface is fine, the surface was examined using an optical microscope. To make the sample surface even finer, the sample was finally polished using colloidal silica in a vibromet (Buehler Vibromet I) for about 6 hours. The nano-indentation experiment was then carried out on the fine surface in a 10×10 array (100 indents), each one micron in depth using Continuous Stiffness Measurement (CSM) method using Nano-indenter XP (MTS Corporation). Then the average of 100 indents was taken to find out the hardness and the modulus of elasticity of samples. The nano-indenter and the vibromet used in the experiment are shown in Fig. 6.3.1 and Fig. 6.3.2, respectively.

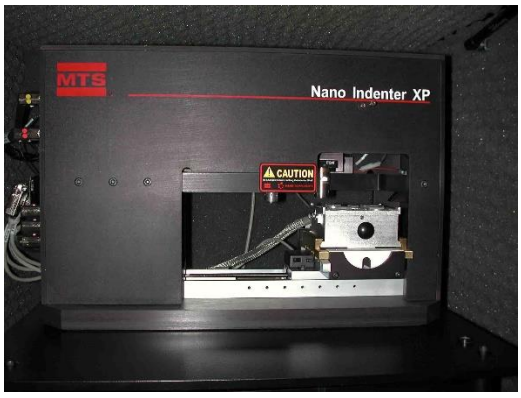

Fig. 6.3.1 Nano-indenter XP (MTS)

Fig. 6.3.2 Vibromet (Buehler).

6.4 Hardness and Young's Modulus of Elasticity of Misch Metal-filled and La/Ce Double-filled Skutterudites

The hardness and the Young's modulus of elasticity of Misch metal-filled $Mm_{0.9}Fe_{3.1}Co_{0.9}Sb_{12}$ ($Mm=La_{0.25}Ce_{0.5}Pr_{0.05}Nd_{0.15}Fe_{0.03}$) and La/Ce double-filled $La_{0.68}Ce_{0.22}Fe_{3.5}Co_{0.5}Sb_{12}$ *p*-type skutterudites were measured. One hundred indentations, each 1 μm deep, were taken on the fine surface of polished samples using Continuous Stiffness Measurement (CSM) method on Nano-indenter XP (MTS Corp.). The hardness and the elastic modulus was then calculated by taking their mean. The displacement-dependent hardness (Fig. 6.4.1a) and Young's modulus of elasticity (Fig. 6.4.2b) are represented by by 6 representative points. The average hardness and elastic modulus are

~7. 4 GPa and ~152 GPa, with no depth dependence beyond 250 nm was measured. Cracking was observed beyond 200 nm, which is a common phenomenon in brittle materials. Thus, to address the plastic flow of the material, another set of nano-indents was made. The maximum penetration depth was limited to 200 nm. By keeping the penetration depth to 200 nm, the cracking and chipping was eliminated. Fig. 6.4.2 shows the AFM scanning and depth profile of residual impression of 200 nm deep indent. The sample shows the pile-up behavior, meaning that the contact area used in Eq. (6.2.1) and Eq. (6.2.3) has been underestimated.

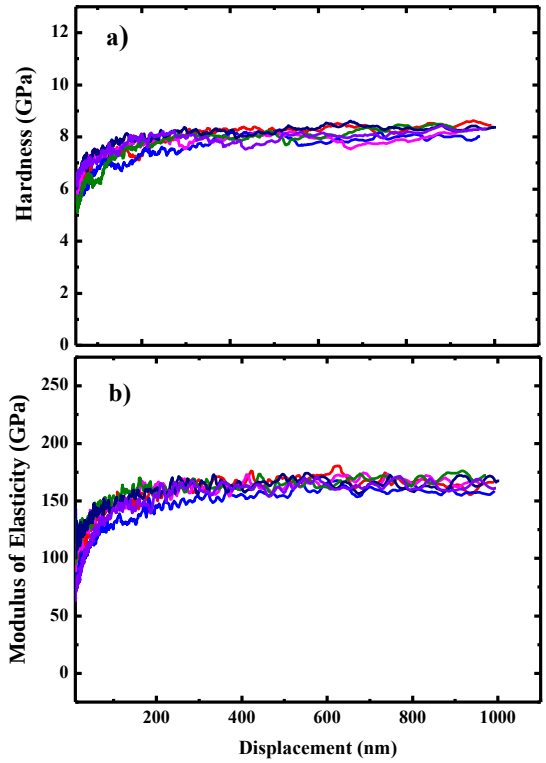

Fig. 6.4.1 Displacement-dependent a) hardness and b) Young's modulus of elasticity of $Mm_{0.9}Fe_{3.1}Co_{0.9}Sb_{12}$ sample.

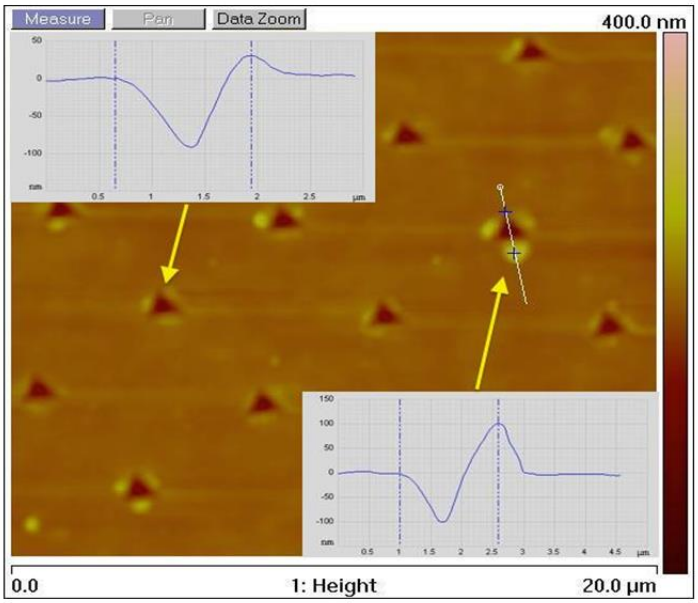

Fig. 6.4.2 AFM micrograph of residual impression on the surface of $Mm_{0.9}Fe_{3.1}Co_{0.9}Sb_{12}$.

Thus, to estimate the hardness and the Young's modulus of the material more accurately, an average mound height is added to the contact depth and the contact area is adjusted to account such behavior. The corrected values of the hardness and the modulus of elasticity then reduced to 4.2 GPa and 116 GPa, which are within the range of previously reported value (2.55-5.69 GPa) of skutterudites [10], and considerably higher than other thermoelectric materials like $Bi_xSb_{2-x}Te_3$ [11], $Ca_3Co_4O_9$ [12], and PbTe-Pbs [10].

The displacement-dependent a) hardness and b) Young's modulus of elasticity of $La_{0.68}Ce_{0.22}Fe_{3.5}Co_{0.5}Sb_{12}$ is as shown in Fig. 6.4.3. The observed trend in hardness/modulus vs displacement curve is similar to the behavior observed in $Mm_{0.9}Fe_{3.1}Co_{0.9}Sb_{12}$.

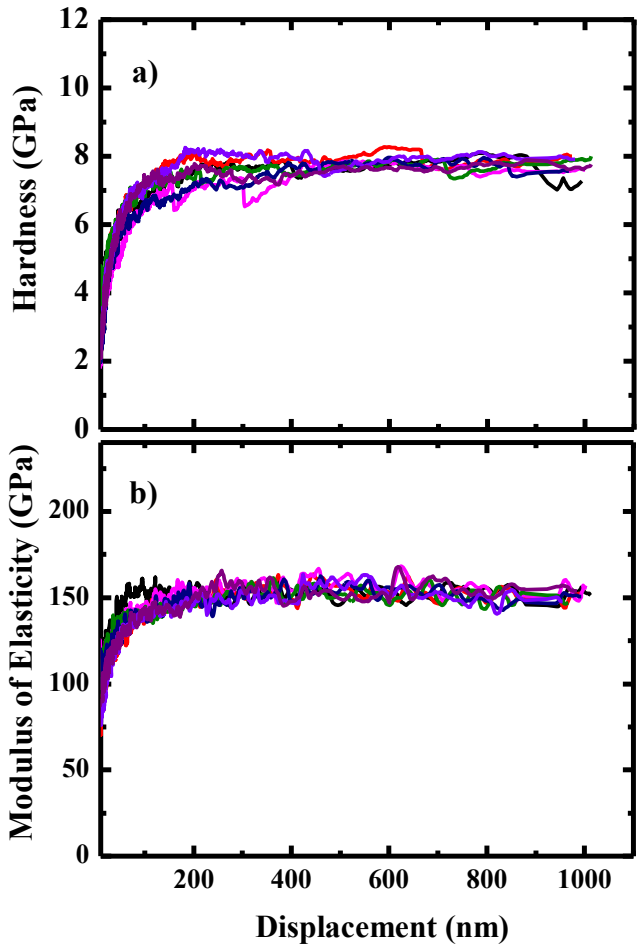

Fig. 6.4.3 Displacement-dependent a) hardness and b) modulus of elasticity of $La_{0.68}Ce_{0.22}Fe_{3.5}Co_{0.5}Sb_{12}$.

The average hardness and Young's modulus of elasticity are ~7.6 GPa and ~148 GPa, respectively, with no depth dependence beyond 200 nm. However, to account the mounding behavior, the indent sample surface was scanned using atomic force micrograph (Fig. 6.4.4). The AFM scan shows the pile-up behavior, indicating the hardness and hence the Young's modulus are overestimated. To truly account for these values, an average

mound height was added to the contact depth as discussed above and the area of contact was calculated accordingly. With the corrections made, the average hardness and the Young's modulus of the sample was reduced to 4.4 GPa and 118 GPa, respectively. The measured values of *H* and *E* of $La_{0.68}Ce_{0.22}Fe_{3.5}Co_{0.5}Sb_{12}$ are similar to that of $Mm_{0.9}Fe_{3.1}Co_{0.9}Sb_{12}$.

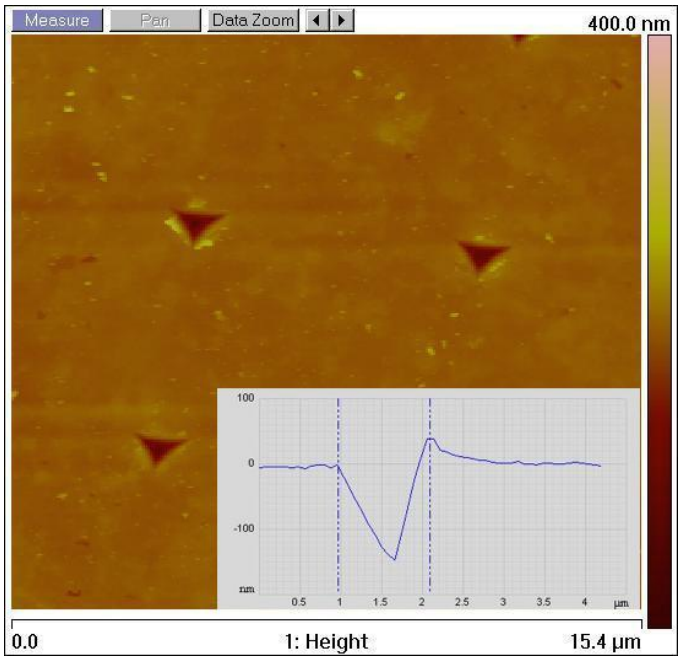

Fig. 6.4.4 AFM micrograph taken on indent surface of $La_{0.68}Ce_{0.22}Fe_{3.5}Co_{0.5}Sb_{12}$.

6.5 Hardness and Young's Modulus of *n*-type Skutterudites $Yb_{0.35}Co_4Sb_{12}$

Considering the long life time of a TE device, both *p* and *n*-type materials should have equal or nearly equal mechanical strength. So, a closer look was given to study the mechanical strength of Yb-filled *n*-type skutterudites material $Yb_{0.35}Co_4Sb_{12}$. The detail

sample synthesis process including their thermoelectric properties can be found in the literature [13]. The sample for nano-indentation was prepared following the method mentioned previously. Considering that the sample is brittle and larger indentation depth can lead to cracking or creeping in the material, 100 indents each of half micron in depth were taken on the sample surface. The hardness and the modulus of elasticity of the sample is then obtained by taking an average of all indents and are plotted in Fig.6.5.1a and 6.5.2b, respectively. An average hardness and the modulus of elasticity, ~8.3 GPa and ~154 GPa respectively, were measured in $Yb_{0.35}Co_4Sb_{12}$. Compared to the hardness of $Mm_{0.9}Fe_{3.1}Co_{0.9}Sb_{12}$ and $La_{0.68}Ce_{0.22}Fe_{3.5}Co_{0.5}Sb_{12}$ (~7.4 GPa and ~7.6 GPa, respectively), the observed higher hardness of $Yb_{0.35}Co_4Sb_{12}$ could be due to higher sintering temperature (750 ^oC) compared to the sintering temperature (650 ^oC) of *p*-type samples.

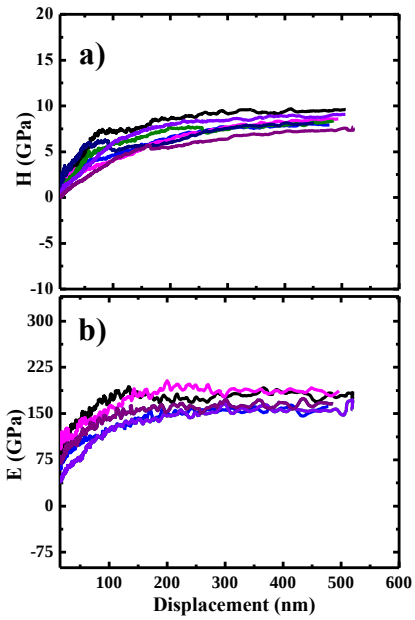

Fig. 6.5.1 Displacement-dependent a) hardness and b) Young's modulus of elasticity of $Yb_{0.35}Co_4Sb_{12}$.

However, to quantify the precise values of the hardness and the modulus of elasticity, sink-in or pile-up behavior of the material should be studied, which requires AFM micrograph of the indent surface. With the further correction, the hardness and modulus value changes.

6.6 Hot Pressing Pressure-dependent Hardness and Young's Modulus of Elasticity: Case Study of *p*-type Skutterudites

To study the effect of hot pressing pressure in mechanical properties of the sample, we made two *p*-type samples with nominal composition $Ce_{0.45}Nd_{0.45}Fe_{3.5}Co_{0.5}Sb_{12}$ at different hot pressing pressure. One of the samples was hot pressed at 650 ^{o}C under a pressure of 80 MPa for 5 minutes while the other was hot pressed at 110 MPa keeping all other conditions same. The density of sample (7.92 g cm^{-3}) hot pressed at 110 MPa was higher than the density (7.71 g cm^{-3}) of the sample hot pressed at 80 MPa. The samples were then polished to get a fine surface as described above. The nano-indenter was then driven into the sample surface with a penetration depth of about half micron. As discussed earlier, we took an average of 100 indents to estimate the hardness and the Young's modulus of elasticity. Fig. 6.61 and 6.6.2 give the displacement-dependent the hardness of the samples hot pressed at 80 MPa and 110 MPa, respectively.

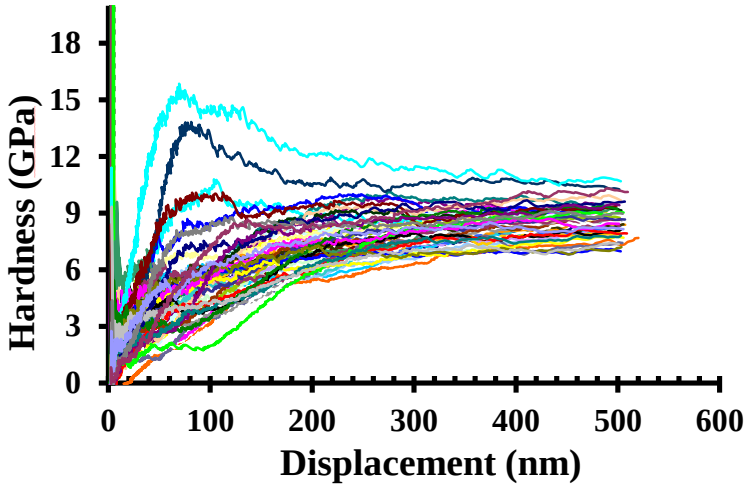

Fig. 6.6.1 Displacement-dependent hardness of $Ce_{0.45}Nd_{0.45}Fe_{3.5}Co_{0.5}Sb_{12}$ HP at 80 MPa.

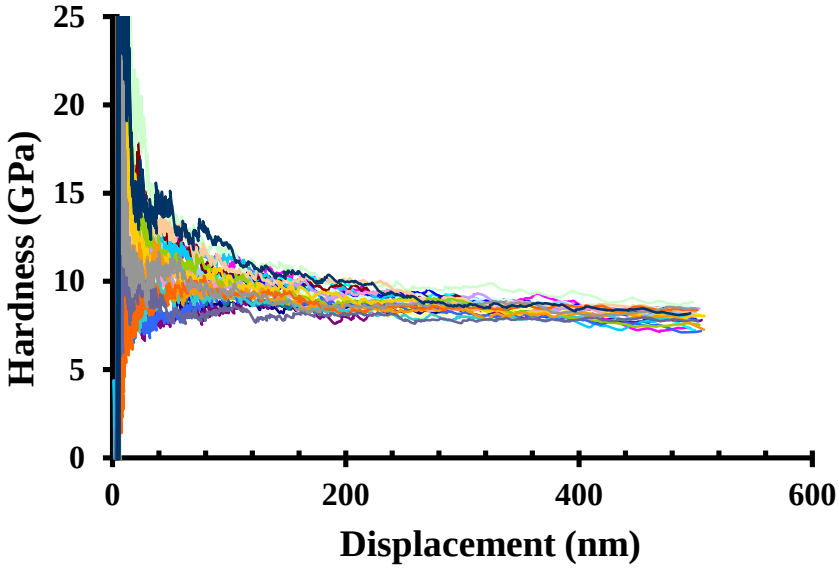

Fig. 6.6.2 Displacement-dependent hardness of $Ce_{0.45}Nd_{0.45}Fe_{3.5}Co_{0.5}Sb_{12}$ sample HP at 110 MPa.

The measured hardness (~7.72 GPa) of the sample hot pressed at 110 MPa is about 23% higher than the hardness (~6.27 GPa) of the sample hot pressed at 80 MPa. The better consolidation of the nano-powder at higher hot pressing pressure yields higher hardness, indicating that the sample has higher resistance to wear. Displacement-dependent modulus of elasticity of the sample hot pressed at 80 MPa and 110 MPa are shown in Fig. 6.6.3 and Fig. 6.6.4, respectively.

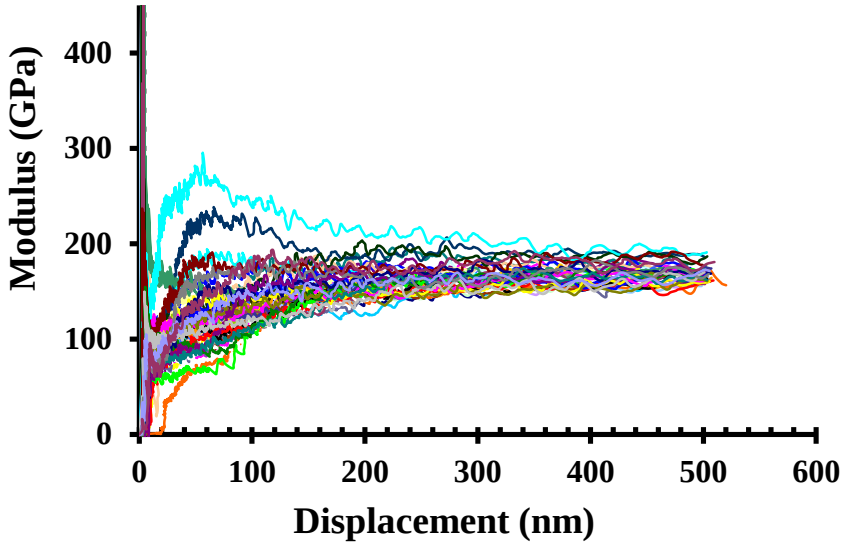

Fig. 6.6.3 Displacement-dependent Young's modulus of elasticity of $Ce_{0.45}Nd_{0.45}Fe_{3.5}Co_{0.5}Sb_{12}$ HP at 80 MPa.

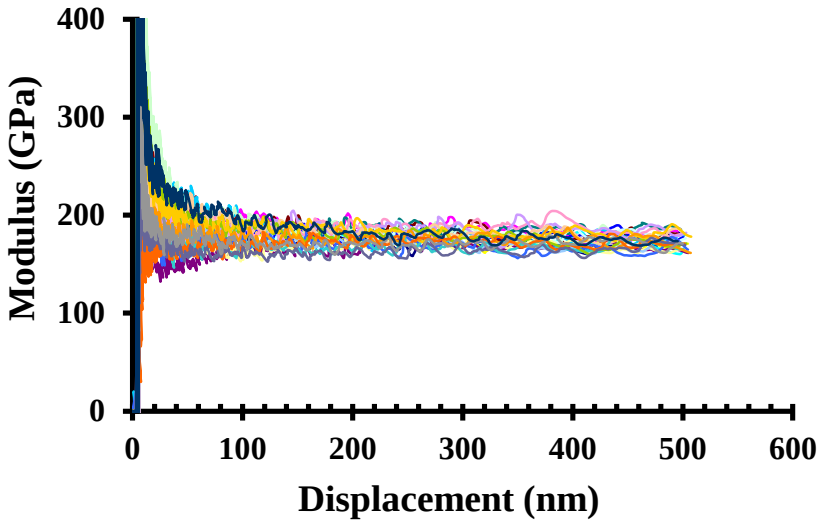

Fig. 6.6.4 Displacement-dependent Young's modulus of elasticity of $Ce_{0.45}Nd_{0.45}Fe_{3.5}Co_{0.5}Sb_{12}$ HP at 110 MPa.

The measured Young's modulus of elasticity (~175 GPa) of the sample hot pressed at 110 MPa is about 14% higher than the Young's modulus of elasticity (~154 GPa) of the sample hot pressed at 80 MPa. Nevertheless, AFM imaging is required to study the mounding behavior to estimate the more realistic value of hardness and modulus of elasticity. The higher hardness and the Young's modulus of elasticity of the sample hot pressed at higher pressure are preferred for practical application if we could preserve the thermoelectric properties of the sample. To examine if the thermoelectric properties of the sample hot pressed at higher pressure maintain the same high *ZT* as reported previously [14], we made different samples from two different ingots by melting-quenching-annealing-ball-milling, and hot pressing. The details of the thermoelectric properties are as shown below.

Two different samples were synthesized by general melting-quenching-annealing-ball-milling, and hot pressing the nano-powder. The data labeled by1st and 2nd ingot represent the measurement result of the sample made from two different ingots by hot pressing the nano-powder at a pressure of ~110 MPa. The data taken from Ref. 14 was hot pressed at 80 MPa. The densities (7.92 and 7.90 g cm^{-3}) of sample hot pressed at 110 MPa is higher than the density (7.71 g cm^{-3}) of the sample hot pressed at 80 MPa.

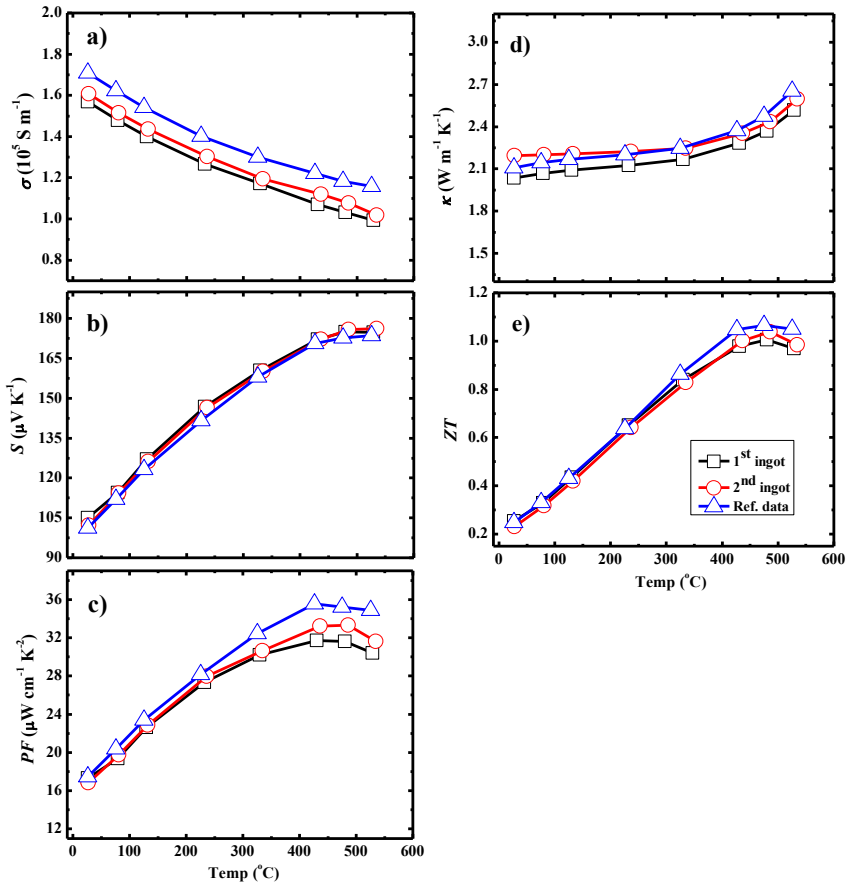

Fig. 6.6.5 Temperature-dependent thermoelectric properties of $Ce_{0.45}Nd_{0.45}Fe_{3.5}Co_{0.5}Sb_{12}$: a) electrical conductivity, b) Seebeck coefficient, c) power factor, d) thermal conductivity, and e) *ZT*. Reference data is taken from Ref. 14.

The temperature-dependent electrical conductivity of the samples is plotted in Fig 6.6.5a. In general, with higher density we expect higher mobility of charge carrier leading to an enhanced electrical conductivity. But, in this experiment we observed that the electrical conductivity of the samples hot pressed at 110 MPa is lower than that of the sample hot pressed at 80 MPa. With the higher hot pressing pressure, we expect smaller grains compared with grains of the sample hot pressed a lower pressure. Thus, with smaller grains, the carrier suffers significant scattering than while the grains are much bigger. Most of grains are about half a micron in size in the sample hot pressed at 80 MPa [14], while the majority of the grains are about 300 nm in the samples hot pressed at 110 MPa. The SEM images plotted in Fig. 6.6.6 confirms the smaller grains in the samples hot pressed at higher pressure.

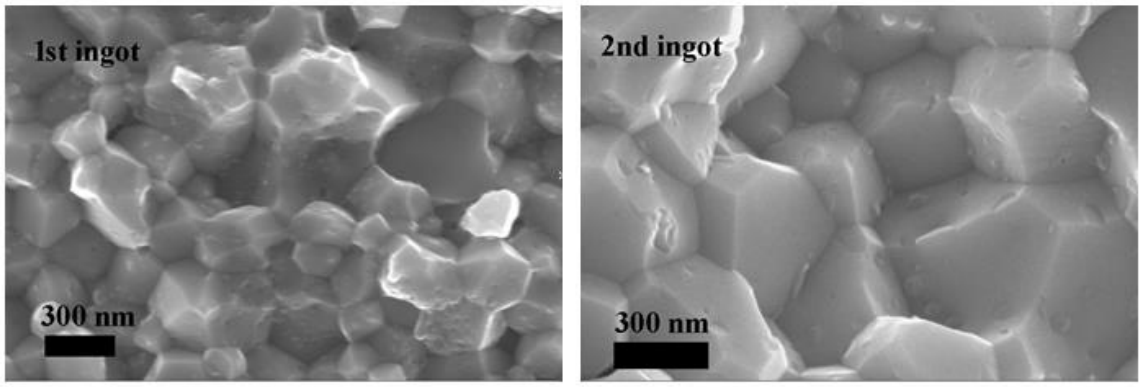

Fig. 6.6.6 High magnification SEM images of the samples HP at 110 MPa.

The temperature-dependent Seebeck coefficient plotted Fig 6.6.5b. The Seebeck coefficient of the samples increases with temperature and do not vary significantly with

each other. However, the *PF* (Fig. 6.5.5c) of the sample hot pressed at a lower pressure is higher than the *PF* of the samples hot pressed at higher pressure, which is mainly due to a higher electrical conductivity of the sample. The total thermal conductivity (Fig. 6.6.5d) of all samples is almost the same in the entire temperature range. From the measured electrical conductivity, Seebeck coefficient, and the thermal conductivity, temperature-dependent dimensionless figure-of-merit, *ZT* was calculated and is plotted in Fig.6.6.5e. The *ZT* value of the sample lies within the error range, indicating that the results are well reproducible even if the hot pressing pressure is high.

6.7 Summary

The hardness and the Young's modulus of elasticity of various *p*-type and a single-filled *n*-type skutterudites were measured using nano-indenter. The measured hardness and the Young's modulus of La/Ce double-filled $La_{0.68}Ce_{0.22}Fe_{3.5}Co_{0.5}Sb_{12}$ and misch metal-filled $Mm_{0.9}Fe_{3.1}Co_{0.9}Sb_{12}$ show similar values. AFM micrograph taken on the indent surface of both *p*-type samples show pile-up behavior. Accounting the pile-up height, the hardness and the Young's modulus of elasticity was re-evaluated. With the correction, the hardness and the Young's modulus of La/Ce double-filled *p*-type skutterudites were observed to be ~4.2 GPa and ~114 GPa, respectively and that of misch metal-filled sample were ~4.3 GPa and ~118 GPa, respectively. The hardness and the elastic modulus values of $Yb_{0.35}Co_4Sb_{12}$ were higher than its counter *p*-type sample. A higher hardness and the modulus of elasticity were found in *p*-type $Ce_{0.45}Nd_{0.45}Fe_{3.5}Co_{0.5}Sb_{12}$ samples hot pressed at 110 MPa, preserving the *ZT* value.

6.8 References

1. Bulychev *et al., Zavod. Lab* **1975,** 41, 1137.
2. Frohlich *et al., Phys. Status Solidi (a)* **1977**, 42, 79.
3. Hay *et al., ASM Handbook* **2000**, 8, 232.
4. *Case et al., Thermo Mechanical Fatigue and Fracture*, WIT Press, Southampton, UK **2002**, pp 137.
5. Oliver *et al., J. Mater. Res*. **1992**, 7, 1564.
6. Bhusan *et al., Handbook of Micro/nanotribology*, CRC Press, Boca Raton, FL **1999**.
7. Tabor *et al., The Hardness of Metal*, Oxford Univ. Press, London, **1951.**
8. Pharr *et al., Mater. Sci. Eng. A* **1998**, 253, 151.
9. Oliver *et al., J. Mater. Res.* **1992**, 7, 1564.
10. Zhang *et al., Materials Science and Engineering B* **2010**,170, 26.
11. Li *et al., Nanotechnology* **2012**, 23, 065703.
12. Kenfaui *et al., J. Alloys and Compds*. **2010**, 490, 427.
13. Dahal *et al., Acta Materialia* **2014,** 75, 316.
14. Jie *et al., Phys. Chem. Chem. Phys*. **2013**, 15, 6809.

.

Chapter 7

Exploring Contact Alloy for Si-Ge

7.1 Introduction

The thermoelectric figure-of-merit (*ZT)* of both *p*-type and *n*-type Si-Ge-based alloys have been improved significantly via nano-structuring approach [1, 2]. Developing the contact alloy with small contact resistance with TE material makes the application of Si-Ge-based material close to realization easily. In a real TE device, there are several layers between TE materials and the heat source and sink. Some of the layers to mention are the metal strip for electrical conduction between TE legs and ceramic plate for heat conduction from source/sink to TE legs. Most of the best thermoelectric materials are hard to solder into conducting strips directly, or easy to react with solder and degrade the performance of material via diffusion. So, an anti-diffusion barrier or contact layer between conducting strip and TE legs is required in addition to higher *ZT* value of material.

While considering the TE device, a proper contact between the thermoelectric leg and electrode is required. An ideal contact material requires high electrical and thermal conductivity. In addition, the contact alloy should have similar coefficient of thermal expansion (CTE) with TE material, strong bonding between them, and mechanically stable at working temperature. A small contact resistance between TE material and contact alloy at working temperature is desired to minimize the Joule's heat at the interface. Larger contact resistance at the interface of alloy and TE material leads to large Joule's heat ($H = I^2Rt$), which not only makes the bonding between alloy and material weaker but also

causes the diffusion of material from alloy side towards the thermoelectric material. This results a change in TE property of material in long run. A schematic representation of practical thermoelectric module is as shown in Fig 7.1.1.

In this chapter, we will discuss our approach to explore the contact alloy for both *n* and *p*-type Si-Ge material.

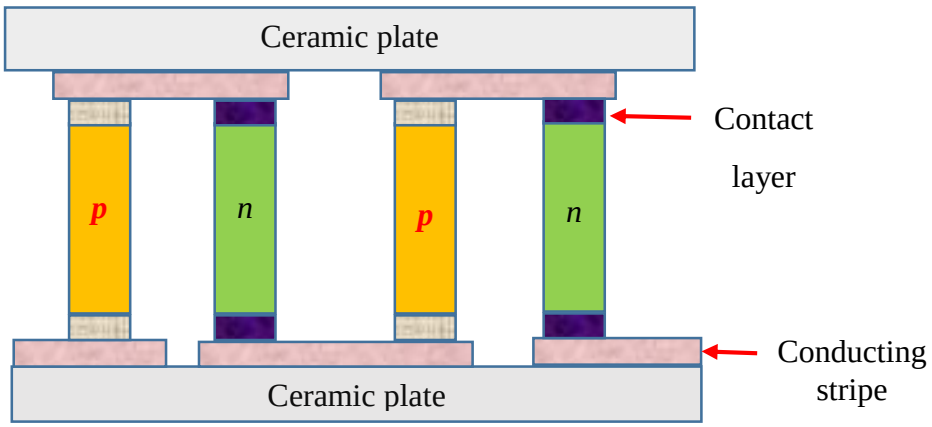

Fig. 7.1.1 Configuration of a practical thermoelectric module.

7.2 Sample Preparation and Measurement Technique

The *n*-type and *p*-type Si-Ge samples were synthesized as described in literature [1, 2]. Different contact alloys (which we will discuss later) were also ball milled for an hour. One step sintering process was used to make the sample disk. The schematic representation of loading the powder in a graphite die is as shown in Fig. 7.2.1

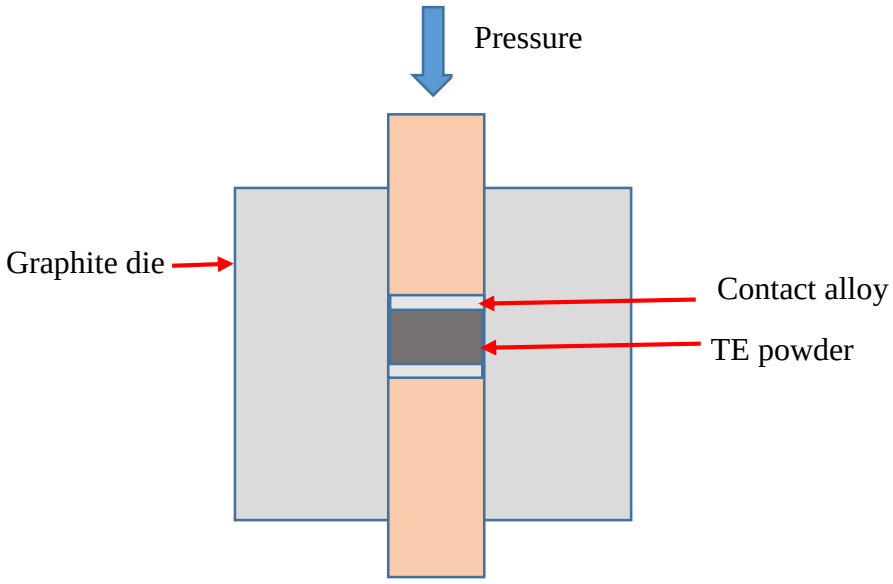

Fig. 7.2.1 Schematic drawing configuration of TE leg fabrication.

The TE powder was kept in between contact alloy in a graphite die and DC hot pressed simultaneously to get the sample disk. The hot press temperature and pressure used for *n*-type Si-Ge sample were 1050 ^{o}C and ~100 MPa, respectively while the *p*-type sample was sintered at 1150 ^{o}C at ~130 MPa, each for 2 minutes. The *n*-type and *p*-type Si-Ge powder used in this work are $Si_{80}Ge_{20}P_2$ and $Si_{80}Ge_{20}B_5$, respectively. Once the hot press was complete, the graphite die was immediately taken out and allowed to cool down slowly in air. A small TE leg with a cross-sectional area about 2×2 mm^2 required for contact resistance measurement was made by finely polishing the legs obtained by chopping the disk sample using a diamond blades. The sample for contact resistance measurement requires scanning the voltage from contact alloy to TE material horizontally. The schematic representation of the measurement method is shown in Fig. 7.2.2.

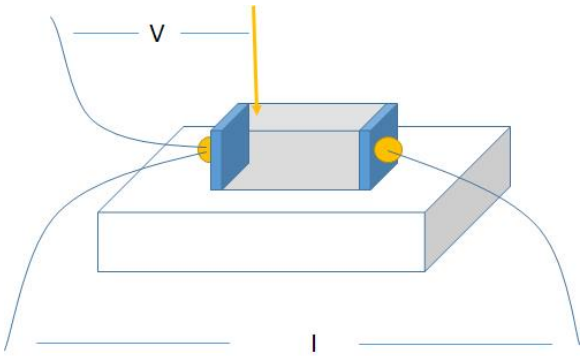

Fig. 7.2.2 Schematic representation of contact resistance measurement.

As shown in Fig. 7.2.2, three wires were soldered on the contact layers at the two ends of TE leg. The TE leg was fixed in the glass substrate. Current was fed from two wires attached on two ends of the contact alloy using Keithley 2400 Digital SourceMeter. Third wire and the spring-loaded pogo pin (size ~2 μm) measure the voltage drop. The pogo pin moves up and down and moves horizontally in a translation stage and scans the potential at different locations of the contact alloy and the TE material. A Keithley 2182 Nano VoltMeter was used to record the potential difference between pogo pin and the third wire. During the measurement, the voltmeter records the total potential coming from four different regions: potential drop in between the solder and the contact alloy, potential drop in the contact alloy, drop in the interface of contact alloy and thermoelectric leg, and potential drop across the thermoelectric material. So, the toal voltage can be written as,

$$V = V_S + V_A + V_C + V_{TE} = I(R_s + R_A + R_C + R_{TE}) \ldots\ldots\ldots\ldots (7.2.1)$$

$$R_A = \frac{\rho_A l_A}{A} \ldots\ldots\ldots\ldots\ldots\ldots\ldots\ldots\ldots (7.2.2)$$

$$R_C = \frac{\rho_C}{A} \ldots\ldots\ldots\ldots\ldots\ldots\ldots\ldots\ldots (7.2.3)$$

$$R_{TE} = \frac{\rho_{TE} l_{AE}}{A} \ldots\ldots\ldots\ldots\ldots\ldots\ldots\ldots\ldots (7.24)$$

where R_s is the resistance between the solder and electrode interface, R_A is the resistance of electrode alloy, R_c is the resistance between the interface of alloy electrode and thermoelectric material, called contact resistance, and R_{TE} comes from the thermoelectric material. Ideally, the electrical conductivity of contact electrode should be much larger than the electrical conductivity of TE material. This indicates that the potential drop across the TE material should be much larger compared to the potential drop in the contact alloy. The schematic representation of voltage drop as a function of scanning distance from one end of contact alloy is as shown in Fig. 7.2.3. The potential drop across the interface of contact alloy and TE material can be obtained by subtracting the extrapolated V_{TE} from V_A where the alloy layer ends.

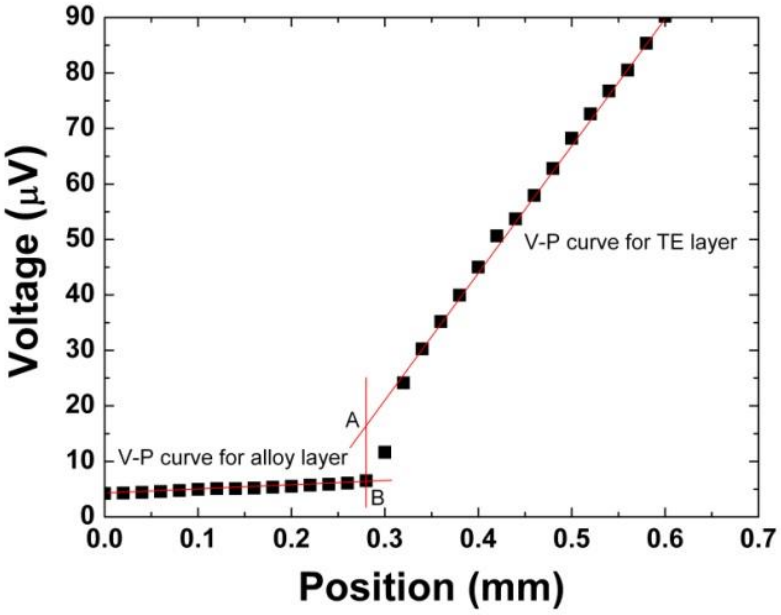

Fig. 7.2.3 Example of potential vs position plot in a contact resistance measurement.

7.3 Experiments

Since the thermal conductivity and the electrical conductivity of $CoSi_2$ is much higher than the thermal and electrical conductivities of Si-Ge, $CoSi_2$ powder was used as the starting contact alloy powder for Si-Ge samples. *n*-type Si-Ge powder was sandwiched between $CoSi_2$ powder as shown in Fig 7.2.1 and hot pressed at 1050 ^oC at a pressure of 100 MPa for 2 minutes and let it cool down in air. The sample was ejected from the die and polished to get a flat surface. We observed a lot of cracks on the sample surface, which is due to the mismatch between the thermal expansion coefficient between $CoSi_2$ and Si-Ge sample. We observed that $CoSi_2$ layer chipped off from the TE material, indicating a weaker bonding between the TE material and the contact alloy.

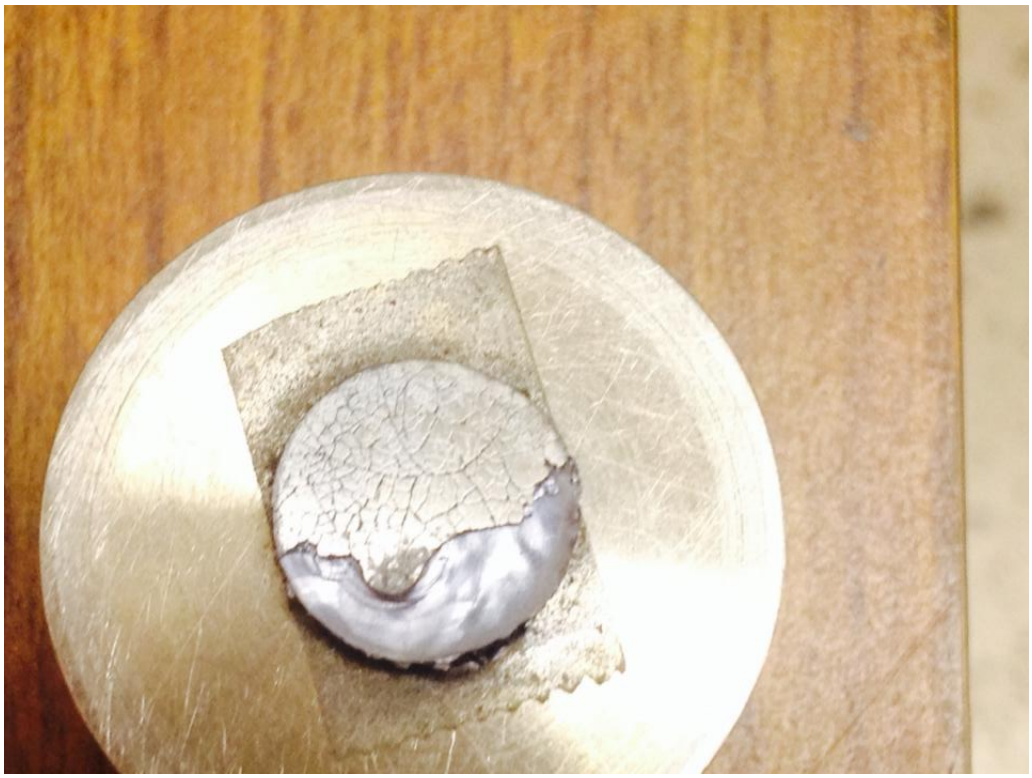

Fig. 7.3.1 *n*-type $Si_{80}Ge_{20}P_2$ sample hot pressed together with $CoSi_2$ as a contact layer.

To avoid the cracks after the hot press, a material with comparable CTE should be chosen, which requires experimental determination of the CTE of the TE material and the contact alloy. The thermal expansion coefficient of both *n*-type ($Si_{80}Ge_{20}P_2$) and *p*-type ($Si_{80}Ge_{20}B_5$) samples were measured using dilatometer. Fig.7.3.2 shows the thermal expansion coefficient of *p*-type $Si_{80}Ge_{20}B_5$ as a function of temperature. The blue dot curve represent the expansion of material in heating cycle while the red one represents the expansion coefficient during cooling. There is a difference in the expansion coefficients at higher temperatures. However, this discrepancy narrows down at lower temperatures and shows similar value from room temperature to about 600 ^oC. With this experiment, the

CTE of *p*-type $Si_{80}Ge_{20}B_5$ was found to be ~4.5×10^{-6} K^{-1} at room temperature. The increment in CTE of the sample at higher temperature is not significant.

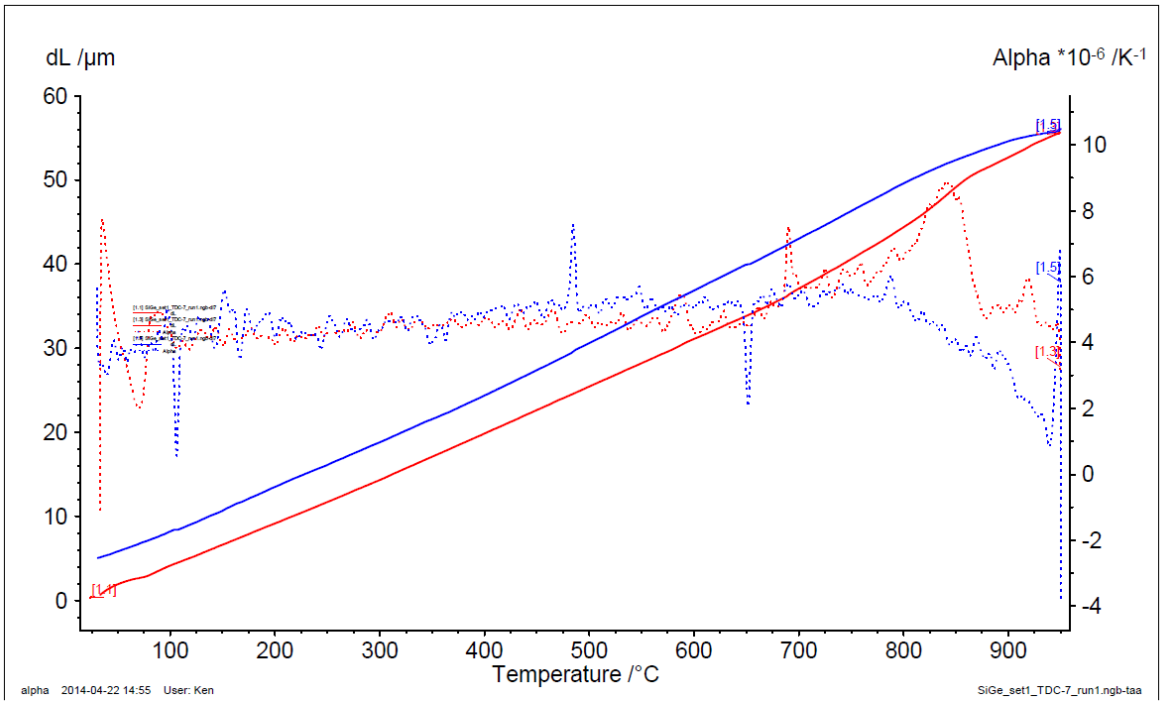

Fig.7.3.2 Temperature-dependent thermal expansion coefficient of *p*-type $Si_{80}Ge_{20}B_5$

The blue solid line represents the changes in length of the sample with temperature while ramping the temperature up, and the red solid line represent the same quantity while the sample is cooled. The measured value of the Young's modulus of elasticity (~175 GPa,) of the sample suggests that the sample is elastic in nature. So, the difference in length at room temperature after one cycle heat treatment for this sample is expected to be zero or near to zero. The observed difference in length after one complete cycle could be due to the sample geometry. A bar sample with perfectly parallel sides is required to precisely measure the

CTE. The difference in change in length with temperature may be due to imperfect sample dimension. The thermal expansion coefficient of *n*-type $Si_{80}Ge_{20}P_2$ is plotted in Fig.7.3.4. The thermal expansion coefficient of *n*-type material is almost similar to *p*-type material as expected. However, the difference in thermal expansion coefficient during heating and cooling cycle at higher temperature is significantly higher than *p*-type Si-Ge sample. Also, the difference in change in length after one cycle measurement in *n*-type material is larger compared to *p*-type material, indicating the significant departure of sample geometry from an ideal geometry.

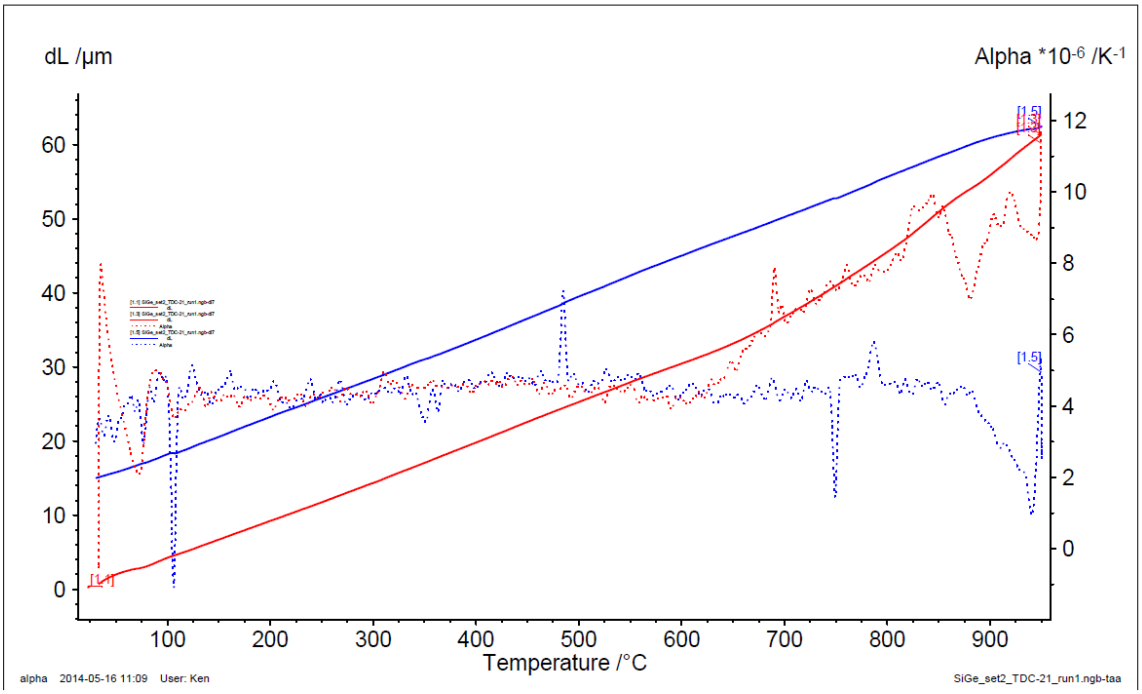

Fig. 7.3.3 Temperature-dependent thermal expansion coefficient of *n*-type $Si_{80}Ge_{20}P_2$.

After having the CTE expansion of TE material, contact alloy with similar CTE were explored. Molybdenum is one of the materials that satisfies some of the requirements [CTE~4.8 K^{-1}, κ~140 W m^{-1} K^{-1}, and σ~5.3×10^{-6} Ω-cm at room temperature (3)] of an ideal contact alloy. To achieve a low contact resistance between the contact alloy and the TE material, the Schottky barrier height at the interface of two material should be small, which can be achieved by matching the work function. The work function of Mo (~ 4.36-4.85 eV) is similar to the work function (~4.65 eV) of Si-Ge, which may lead to smaller Schottky height, lowering the contact resistance. So, both *p*-type and *n*-type Si-Ge samples were hot pressed using Mo as a contact layer. The observed shiny surface of $Si_{80}Ge_{20}P_2$ after polishing (Fig. 7.3.4a) indicates the consolidation of the powder into dense disk. However, when the sample was kept in a cutting machine, the contact layer pilled out from the TE material (Fig. 7.3.4b), showing a weak bonding between them. Similar behavior was observed in *p*-type Si-Ge.

Fig. 7.3.4 a) Hot pressed $Si_{80}Ge_{20}P_2$ using Mo as contact layer, b) picture showing the chipped off contact layer from $Si_{80}Ge_{20}P_2$, and c) picture showing the chipped off contact layer from $Si_{80}Ge_{20}B_5$.

In order to improve the boding between the TE material and the contact alloy, we ball milled Mo with small amount of phosphorous (about 1% by atomic weight) and used as the contact alloy powder for *n*-type $Si_{80}Ge_{20}P_2$ sample. The observed shiny surface of the sample (Fig. 7.3.5a) shows the consolidation of the TE material and the contact alloy into a dense sample. However, the side view of the samples (Fig. 7.3.5b) indicates that the bonding between the samples is not strong enough. Other contact alloy powders used for *n*-type Si-Ge sample were Mo+1.5%P, Mo+2%P, and Mo+1%Ni. But, the attempt to consolidate the TE powder with these different alloy powders did not result a single good sample. For *p*-type Si-Ge, we used ball milled Mo+ (1%, 1.5%, and 2%)B alloy powder as contact layer and consolidate to a disk. The contact layer was not strongly bonded with the TE material in this case as well.

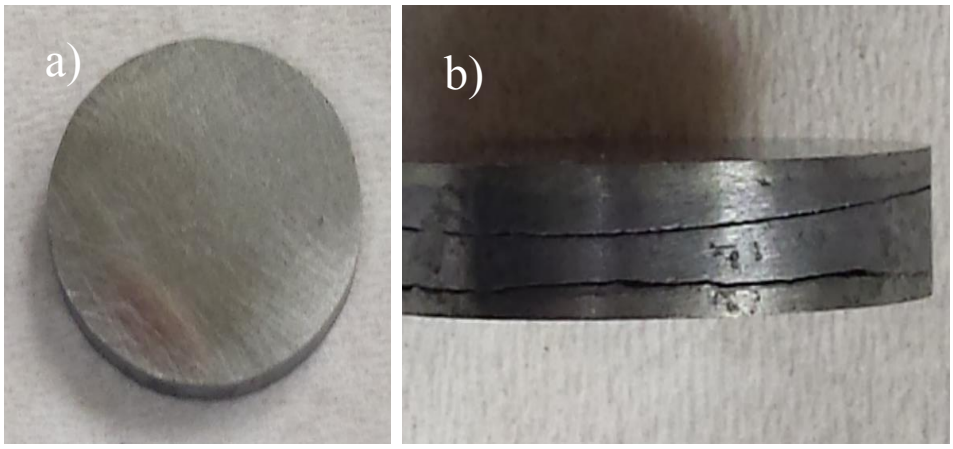

Fig. 7.3.5 a) Top view of $Si_{80}Ge_{20}P_2$ sample hot pressed using Mo-P as contact alloy, and b) side view showing the crack between contact alloy and TE material.

To improve the bonding strength, we chose $MoSi_2$ as a contact layer. The reported high thermal conductivity (Fig. 7.3.6a) and comparable thermal expansion [4] of the sample (Fig. 7.3.6b) satisfies some of the requirements of an ideal contact layer. However, the difference in CTE of $MoSi_2$ is significantly different than that of Si-Ge samples at higher temperature.

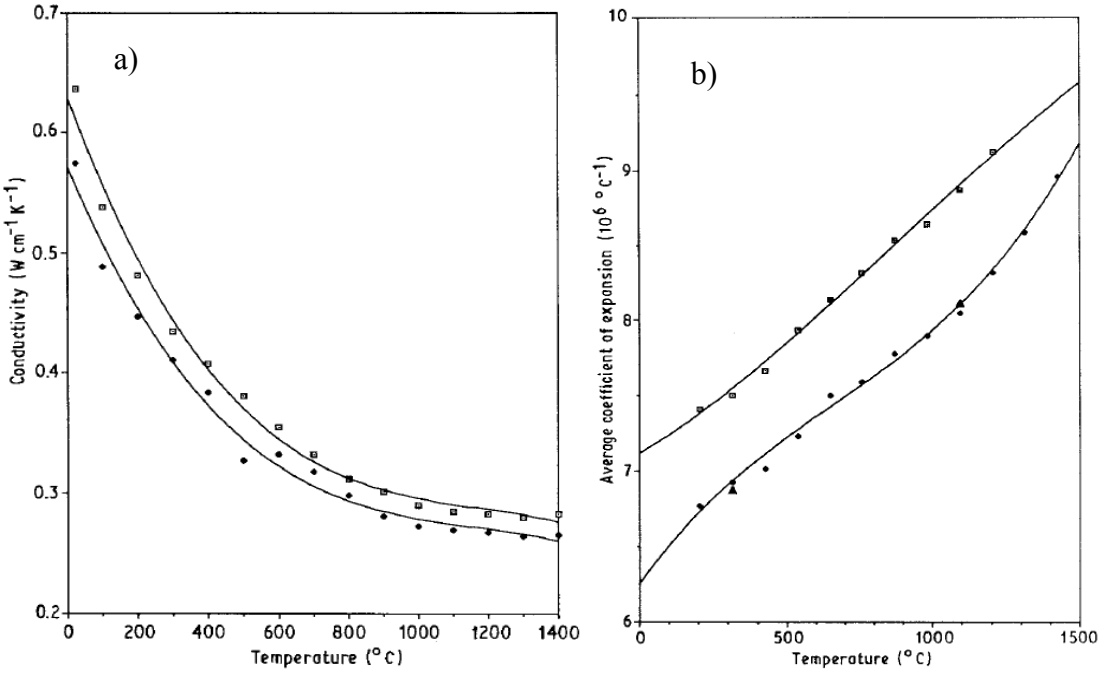

Fig. 7.3.6 Temperature-dependent a) thermal conductivity and b) thermal expansion coefficient of $MoSi_2$. Plot is taken from Ref. [4].

Using $MoSi_2$ as contact layer, *n*-type Si-Ge sample was sintered. Two sides of polished sample is shown in Fig. 7.3.7. The observed difference in the texture of sample surface indicates non-uniformity in the hot press temperature on different sides of sample. Since we used a DC hot press system, the temperature gradient in the sample might result such a texture. An approach to improve the uniformity in sample surface using an AC hot press

system was attempted. But, we ended up with similar sample surface. A closer examination of the phase diagram of Mo-Si indicates that higher sintering temperature is required to densify the $MoSi_2$ powder [5]. Using a higher temperature to densify the alloy power impacts the TE property of Si-Ge adversely. So, higher sintering temperature cannot be used to densify the alloy.

Fig. 7.3.7 Two sides of *n*-type $Si_{80}Ge_{20}P_2$ sample hot pressed using $MoSi_2$ as contact layer.

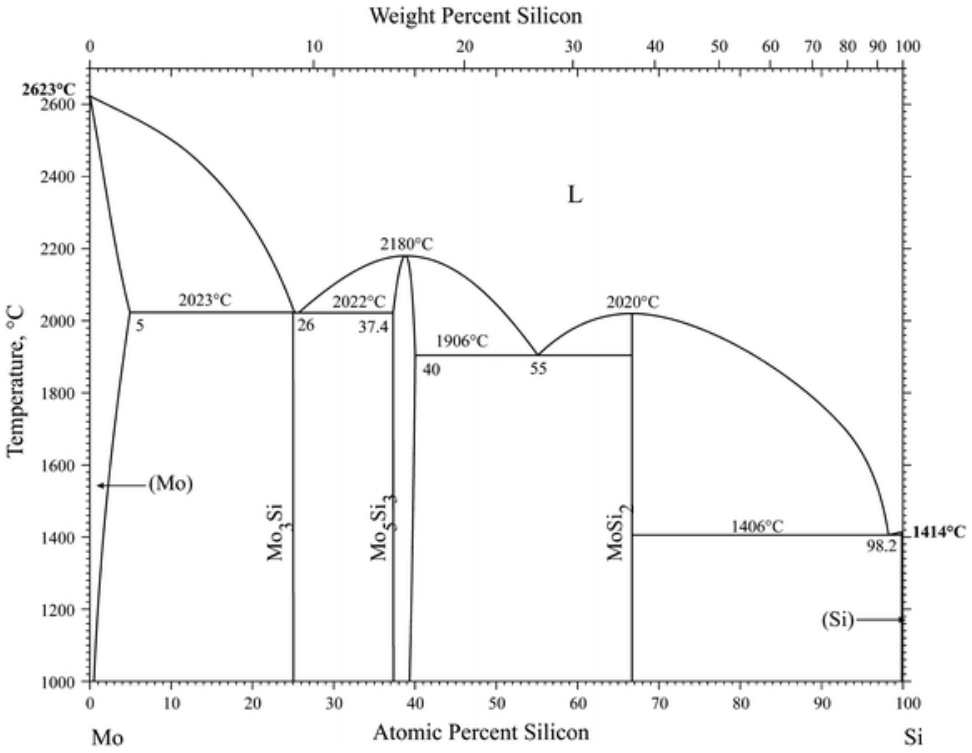

Fig. 7.3.8 Phase diagram of Mo-Si binary alloy. Phase diagram is taken from Ref. [5]

We had examined yet another alloy. Small amount of Ni was arc melted together with Mo and Si to make $MoSi_2Ni_{0.05}$, ball milled for an hour and used the powder as a contact alloy. The addition of small amount of Ni may alter the phase change temperature and could greatly reduce the temperature required to densify the sample. However, we observed two different issues [Fig. 7.3.9] with this contact alloy: a) several cracks were observed on the sample surface and b) contact alloy chipped off from the disk, indicating weaker bonding. Since Ni has large thermal expansion coefficient (~13.4 K^{-1} at room temperature), small amount of Ni can lead to larger CTE mismatch between the contact alloy and the TE material, resulting cracks on the sample surface.

Fig. 7.3.9 *n*-type $Si_{80}Ge_{20}P_2$ sample hot pressed using $MoSi_2Ni_{0.05}$ as contact alloy.

7.4 Summary

Several contact alloy powders were sintered with both *p*-type and *n*-type Si-Ge samples following a one-step sintering method. We observed two main issues: a) the bonding between the TE material and alloy powder was so weak that the alloy disk chipped off from the material, and b) CTE mismatch between the TE material and contact alloy resulted number of cracks on sample surface. Further investigation is required to find out a suitable contact alloy that can exhibit a strong bonding and CTE match with the TE material.

7.5 References

1. Joshi *et al., Nanoletters* **2008**, 8, 4670.
2. Wang *et al., Appl. Phys. Lett.* **2008**, 93, 193121.
3. http://en.wikipedia.org/wiki/Molybdenum
4. Bose *et al., J. Mater. Sci* **1992**, 27, 2749.
5. Okamoto *et al., J. Phase Equilibria and Diffusion* **2011**, 32, 176.

Chapter 8

Summary

In conclusion, we have synthesized Yb-filled *n*-type skutterudites ($Yb_xCo_4Sb_{12}$: x = 0.2, 0.35, 0.45, 0.5, and 0.6) by melting-quenching-ball-milling, and hot pressing the nano-powder using a DC hot press system. XRD spectra of the material shows that the solubility of Yb in the host system can be enhanced to as much as 0.5 by choosing different synthesis process, which is much higher than so called solubility of 0.2. The thermoelectric properties of $Yb_{0.35}Co_4Sb_{12}$ made by hot pressing the nano-powder obtained from ball milled ingot is compared with the previously reported sample with same nominal composition made by hot pressing the powder obtained from directly ball-milling the constituent elements. We observed higher electrical conductivity in the sample made from melting method, which may be due to the presence of fewer defects due to pre-alloying the elements. With higher electrical conductivity and similar Seebeck coefficient, a high power factor (~53 $\mu W\ cm^{-1}\ K^{-2}$ at 550 ^oC) is achieved in $Yb_{0.35}Co_4Sb_{12}$. Compared with the uniformly distributed grain size in the previously reported sample $Yb_{0.35}Co_4Sb_{12}$, we observed a wide grain-size distribution (~200 nm – 1 μm) in the present sample. The wide grain size distribution scatters off the phonon of different mean free paths, resulting lower lattice thermal conductivity. With higher power factor and similar thermal conductivity, we achieve a peak ZT~1.4 at around 550 ^oC in $Yb_{0.35}Co_4Sb_{12}$, which is higher than previously reported peak ZT of ~1.2 for same nominal composition.

The effect of sample synthesis conditions on thermoelectric performance of Yb-filled skutterudites were investigated. A longer ball-milling time significantly reduced the lattice thermal conductivity without affecting electrical conductivity too much. However, a relatively longer ball-milling time reduced the electrical conductivity significantly, which may be due to the presence of defects due to high energy ball-milling process. A higher hot press temperature improved the electrical conductivity, which could be due to less scattering of the carriers from the bigger grains.

Experiments were carried out by bringing a distortion on Sb-planner ring of skutterudites by replacing small amount of Sb by Sn and Te. A small perturbation made on Sb-planner ring can can bring a substantial phonon scattering via mass fluctuation, and improve the electrical conductivity due to the change in concentration and the mobility of the carrier. We observed that small amount of Sn can reduce the lattice thermal conductivity in $CoSb_{2.8}Sn_{0.005}Te_{0.195}$. With a moderate high power factor (~42 $\mu W\ cm^{-1}\ K^{-2}$ at 550 ^oC) and a lower thermal conductivity (~2.6 $W\ m^{-1}\ K^{-1}$ at 550 ^oC), we achieve a peak *ZT* in excess of 1.1 at 550 ^oC in $CoSb_{2.8}Sn_{0.005}Te_{0.195}$. The improved *ZT* in $CoSb_{2.8}Sn_{0.005}Te_{0.195}$ may be due to the improved electrical conductivity due to higher Te solubility in $CoSb_3$ by alloying it with Sn, and reduced thermal conductivity due to scattering off phonon from smaller grains and via mass fluctuation scattering. This *ZT* value fairly competes with the *ZT* of most of the single-filled skutterudites.

Considering the practical application, the efficiency of a thermoelectric device can be enhanced if both *n* and *p*-type materials have similar high *ZT* values. Keeping in mind that the thermoelectric performance of *p*-type skutterudites is inferior compared to its *n*-type

counterpart, we extended our research to improve the thermoelectric properties of *p*-type skutterudites. Since Ni has one more electron than Co, using Ni as a charge compensator in *p*-type skutterudites is expected to have lower electrical conductivity and higher thermal conductivity due to bipolar conduction at elevated temperatures. However, we have demonstrated that by suitably tuning the Fe/Ni ratio together with appropriate fillers concentration, it is possible to achieve a high power factor (~35 μW cm^{-1} K^{-2} at 535 ^{o}C) and a lower thermal conductivity (~2.6 W m^{-1} K^{-1} at 535 ^{o}C), leading to a peak *ZT*~1.1 at 475 ^{o}C in $Ce_{0.4}Nd_{0.4}Fe_{3.7}Ni_{0.3}Sb_{12}$.

Since most of the heat-carrying phonons in solids have lower vibrational frequencies, we synthesized La/Ce double-filled *p*-type skutterudites, the fillers with lower vibrational frequencies (79 cm^{-1} and 73 cm^{-1} for La and Ce, respectively) along [111] direction in Fe-based skutterudites RFe_4Sb_{12}. The small variation in thermal conductivity (~2.4 W m^{-1} K^{-1} at room temperature and ~2.5 W m^{-1} K^{-1} at 535 ^{o}C), and a high power factor (~35 μW cm^{-1} K^{-2} at 535 ^{o}C) was achieved in $La_{0.68}Ce_{0.22}Fe_{3.5}Co_{0.5}Sb_{12}$, leading to a peak *ZT* above 1.1 at 500 ^{o}C. An output power density ~8 W cm^{-2} in 2×2×12 mm^3 bar sample of $La_{0.68}Ce_{0.22}Fe_{3.5}Co_{0.5}Sb_{12}$ is estimated for ΔT = 475 ^{o}C between the heat source and sink. Keeping in mind that the fillers with different atomic masses and ionic radii can scatter off phonons in a wide range, rare earth-based misch metal (Mm= $La_{0.25}Ce_{0.5}Pr_{0.05}Nd_{0.15}Fe_{0.03}$) filled *p*-type skutterudites $Mm_{0.9}Fe_{4-x}Co_xSb_{12}$ (x = 0.7, 0.8. 0.9, and 1) samples were synthesized. A high power factor (~30 μW cm^{-1} K^{-2} at 425 ^{o}C) and a low thermal conductivity (~1.9 W m^{-1} K^{-1} at 425 ^{o}C) achieved in $Mm_{0.9}Fe_{3.1}Co_{0.9}Sb_{12}$ leads to a peak *ZT*~1.1 at 425 ^{o}C. The shift of peak *ZT* at a lower temperature enhances the

average *ZT* of material system, which could potentially increases the conversion efficiency of the TE device.

The hardness and the Young's modulus of elasticity of some of the best *p* and *n*-type samples were examined using nano-indentation experiment. With depth-dependence characterization, the observed hardness and Young's modulus of elasticity of $La_{0.68}Ce_{0.22}Fe_{3.5}Co_{0.5}Sb_{12}$ and $Mm_{0.9}Fe_{3.1}Co_{0.9}Sb_{12}$ show similar values (~7.6 GPa and 152 GPa, respectively). However, AFM micrograph indicates that the presence of plastic deformation showing pile-up behavior. The hardness and Young's modulus of elasticity (~4.2 GPa and 118 GPa, respectively) of the material yield lower value once the contact area was corrected considering the mound height. The mechanical strength of *n*-type $Yb_{0.35}Co_4Sb_{12}$ sample (hardness ~8.3 GPa and Young's modulus of elasticity ~165 GPa) is better compared to its *p*-type counterpart $Ce_{0.45}Nd_{0.45}Fe_{3.5}Co_{0.5}Sb_{12}$ (hardness ~6.3 GPa and Young's modulus of elasticity ~154 GPa). The hardness and the modulus of elasticity of $Ce_{0.45}Nd_{0.45}Fe_{3.5}Co_{0.5}Sb_{12}$ hot pressed at higher pressure show better mechanical strength. Nonetheless, to quantify more precise value of those parameter, the correction in contact area is required. The measured hardness and Young's modulus of elasticity of skutterudites samples are lower than half-Heusler samples, while much better than Bi_2Te_3 and PbTe-based samples, which signifies skutterudites as one of the prominent material for practical applications.

Several experiments were carried out to explore the contact alloy for Si-Ge-based thermoelectric materials. A weaker bonding between the TE material and the contact alloy was observed in various alloys tested. The mismatch in thermal expansion coefficients

between the contact alloy and the Si-Ge sample was another issue. Further study is required to explore the appropriate contact alloy for this material.

Appendix

Publications and Conference Participations

A1 Publications

1. Dahal *et al.*, *Acta Materialia* **2014**, 75, 316.
2. Dahal *et al., Phys. Chem. Chem. Phys.* **2014**, 16, 18170.
3. Dahal *et al., JOM* **2014**, **66**, 2282.
4. Dahal *et al., J. of Alloys and Compounds* **2015**, 623, 104.
5. Dahal *et al., "Thermoelectric and mechanical properties of La/Ce double-filled p-type $La_{0.68}Ce_{0.22}Fe_{3.5}Co_{0.5}Sb_{12}$ skutterudites",* **Submitted to *Nano-Energy*.**
6. Dahal *et al., "Thermoelectric and Mechanical Properties on Misch Metal Filled p-type Skutterudites $Mm_{0.9}Fe_{4-x}Co_xSb_{12}$",* Submitted **to *J. of Applied Physics.***
7. Joshi, G., **Dahal, T**. *et al., Nano Energy* **2013,** 2, 84.
8. Pokharel, M., **Dahal, T.** *et al.,* J. *Alloys and Compounds* **2014**, 609, 228.
9. Pokharel, M., **Dahal, T**. *et al., Energy Conversion and Management* **2014**, 87, 584.
10. Koirala, M., Zhao, H., Pokharel, M., Chen, S., **Dahal, T**. *et al., Appl. Phys. Lett.* **2013**, 102, 213111.
11. Jie, Q., **Dahal T.** *et al.,* "*Work Function Matching as the Guiding Principle to Achieve Low Contact Resistance for Thermoelectric legs: A Case study for p-type Filled Skutterudite",* **Under Review**.
12. Jie, Q., **Dahal T.** *et al.,* "*n-type triple filled skutterudite material and legs with low contact resistance"*, In **Preparation**.

A2 Conferences Participations

1. **T. Dahal (speaker),** Q. Jie, and Z. F. Ren, *American Physical Society March Meeting 2014, Denver, CO, USA,* "Effect of triple fillers on thermoelectric performance of *p*-type skutterudites".
2. **T. Dahal** (**poster presenter**), G. Joshi, Q. Jie, C. F. Guo, Y. C. Lan, and Z. F. Ren, *International Conference on Thermoelectrics, Nashville, TN, USA*, "Effect of triple fillers on thermoelectric performance of *p*-type skutterudites".
3. **T. Dahal** (**speaker**), G. Joshi, Q. Jie, C. F. Guo, Y. C. Lan, and Z. F. Ren, *47th Semiannual T_CSUH Student Symposium, University of Houston, TX, USA*, "Effect of triple fillers on thermoelectric performance of *p*-type skutterudites".
4. **T. Dahal (poster presenter)**, Q. Jie, W. S. Liu, K. Dahal, Y. C. Lan, and Z. F. Ren, *Graduate Research and Scholarship Project Day, University of Houston, TX, USA*, "Thermoelectric properties of La/Ce double-filled *p*-type skutterudites".